Creep, tensile and corrosion behaviour of Ca and/or Sb added AZ91 Mg alloys

Anil Kumar Singh Bankoti

Department of Metallurgical and Materials Engineering
National Institute of Technology, Rourkela

Creep, tensile and corrosion behaviour of Ca and/or Sb added AZ91 Mg alloys

Dissertation submitted in partial fulfilment

of the requirement of the degree of

Doctor of Philosophy

in

Metallurgical and Materials Engineering

by

Anil Kumar Singh Bankoti

(Roll Number: 512MM102)

based on research carried out

under the supervision of

Prof. Ashok Kumar Mondal

and

Prof. Bankim Chandra Ray

Department of Metallurgical and Materials Engineering

National Institute of Technology, Rourkela

July 2017

Department of Metallurgical and Materials Engineering
National Institute of Technology, Rourkela

Date:……

Certificate of Examination

Roll Number: *512MM102*
Name: *Anil Kumar Singh Bankoti*
Title of Dissertation: *Creep, tensile and corrosion behaviour of Ca and/or Sb added AZ91 Mg alloys*

We the below signed, after checking the dissertation mentioned above and the official record book (s) of the student, hereby state our approval of the dissertation submitted in partial fulfilment of the requirements of the degree of *Doctor of Philosophy* in *Metallurgical and Materials Engineering* at *National Institute of Technology, Rourkela*. We are satisfied with the volume, quality, correctness, and originality of the work.

Bankim Chandra Ray Co-Supervisor	Ashok Kumar Mondal Principal Supervisor
Debasis Chaira Member, DSC	Sandhyarani Biswas Member, DSC
Arunachalam Thirugnanam Member, DSC	Somnath Bhattacharyya External Examiner
Bipin Bihari Verma Chairperson, DSC	Smarajit Sarkar Head of the Department

Department of Metallurgical and Materials Engineering
National Institute of Technology, Rourkela

Prof. Ashok Kumar Mondal
Assistant Professor

Prof. Bankim Chandra Ray
Professor

Date: …….

Supervisors' Certificate

This is to certify that the work presented in the dissertation entitled *Creep, tensile and corrosion behaviour of Ca and/or Sb added AZ91 Mg alloys* submitted by *Anil Kumar Singh Bankoti*, Roll Number 512MM102, is a record of original research carried out by him under our supervision and guidance in partial fulfilment of the requirements of the degree of *Doctor of Philosophy* in *Metallurgical and Materials Engineering*. Neither this dissertation nor any part of it has been submitted earlier for any degree or diploma to any institute or university in India or abroad.

Bankim Chandra Ray Professor Co-Supervisor	Ashok Kumar Mondal Assistant Professor Principal Supervisor

Dedicated to my family

Anil Kumar Singh Bankoti

Declaration of Originality

I, *Anil Kumar Singh Bankoti*, Roll Number *512MM102* hereby declare that this dissertation entitled *Creep, tensile and corrosion behaviour of Ca and/or Sb added AZ91 Mg alloys* presents my original work carried out as a doctoral student of NIT Rourkela and, to the best of my knowledge, contains no material previously published or written by another person, nor any material presented by me for the award of any degree or diploma of NIT Rourkela or any other institution. Any contribution made to this research by others, with whom I have worked at NIT Rourkela or elsewhere, is explicitly acknowledged in the dissertation. Works of other authors cited in this dissertation have been duly acknowledged under the sections "Reference" or "Bibliography". I have also submitted my original research records to the scrutiny committee for evaluation of my dissertation.

I am fully aware that in case of any non-compliance detected in future, the Senate of NIT Rourkela may withdraw the degree awarded to me on the basis of the present dissertation.

Date: ……..

NIT Rourkela Anil Kumar Singh Bankoti

Acknowledgment

First of all, I praise God, the Almighty for providing me this opportunity and granting me the capability to proceed successfully.

I am highly grateful to my supervisor, Prof. Ashok Kumar Mondal for believing in me and encouraging me to study Ph.D. and pursue my dreams. I am also highly grateful to my co-supervisor Prof. Bankim Chandra Ray for his support and encouragement. My sincere thanks to Head of the Department, Metallurgical and Materials Engineering, for providing necessary facilities for this work. My sincere gratitude to members of my doctoral scrutiny committee: Prof. Bipin Bihari Verma, Prof. Debasis Chaira, Prof. Sandhyarani Biswas and Prof. Arunachalam Thirugnanam for their help and support throughout this work. I am also thankful to all the laboratory members of Department of Metallurgical and Materials Engineering, NIT Rourkela. Sincere thanks to Biju Pattanaik Central Library (BPCL) for providing all the necessary literature for the work.

I would like to thank Prof. S. Kumar, Department of Materials Engineering, Indian Institute of Science Bangalore for extending their laboratory facilities and all the necessary support. Special thanks to Prof. S. Seshan, Department of Mechanical Engineering, Indian Institute of Science Bangalore for his help to get all the desired castings. I am also very grateful to Dr. Hajo Dieringa for conducting compressive creep tests.

Thanks to NRC-M programme for providing me all the necessary assistance and facilities during my visits to Department of Materials Engineering, Indian Institute of Science, Bangalore. Ms. Bharthi N, NRC-M Project Administration Co-ordinator, has always been so supportive and helpful. I am also thankful to Department of Science and Technology (DST) for providing financial support to this work.

Thanks for all the help and company, I received from Chandra S. Perugu, Pushpendra, Krishna and all other lab mates in Department of Materials Engineering, Indian Institute of Science Bangalore. Also, I would like to say thank you to current and past members of Prof. Mondal’s group in NIT Rourkela for their direct and indirect contribution to my dissertation.

Sourav, Jichil, Ranjit, Binit, Hrishikesh, Arjun, Pranav, Kishor, Lailesh, Brijesh, and Himanshu are some of the names who made my stay in Rourkela so memorable.

I would like to express my deepest gratitude to my parents for their constant support, love, affection and encouragement throughout in my life. I am thankful to my beloved son. His cheerful smile is able to disappear the biggest tensions in a fraction of a second. I would like to thank my wife for her unconditional love, supportive nature and calm disposition. Just because of her selfless support, I am able to pursue this endeavour. I wish to acknowledge my brother, sister and other family members for their invaluable support.

This thesis, although it bears only my name, is really the result of the work of many. To acknowledge them all individually would be impossible. Please forgive me if I did not acknowledge someone who made some contribution or assisted me during the course of my journey. All errors and limitations remaining in this thesis are mine alone. The long journey of Ph.D. not only helped me to gain knowledge but also taught how to deal with conflicts and difficulties in life.

Date: ……..

NIT Rourkela

Anil Kumar Singh Bankoti

Roll Number: 512MM102

Abstract

In the present thesis, the effects of combined additions of Ca and Sb on microstructure, tensile, creep and corrosion behaviour of AZ91 alloy fabricated by squeeze-casting have been investigated. For comparison, the same has also been studied on the squeeze-cast AZ91 alloy with and without individual additions of Ca and Sb. The composition of all the fabricated alloys are AZ91+0.59Sb (AZY911), AZ91+0.89Ca (AZX911), AZ91+0.91Ca+0.31Sb (AZXY9110), AZ91+0.89Ca+0.62Sb (AZXY9111) and AZ91+1.80Ca+0.33Sb (AZXY9120) (wt.%).

A detailed microstructural characterization of all the fabricated alloys has been done. Tensile tests of all the specimens at ambient, 423 K and 473 K temperatures have been carried out. The impression creep tests are conducted in the stress range of 300 to 480 MPa and temperature range of 423 to 523 K for a dwell time of 7200 s. A detailed microstructural analysis of the creep tested specimens has been carried out to further interpret creep behaviour of the alloys. Compressive creep tests are carried out on all the modified alloys at a temperature 473 K and stress of 70 MPa. The corrosion tests have been performed in 0.5NaCl (wt.%) solution at neutral pH with specimen exposed area of 0.5 cm^2 at ambient temperature.

The results indicate that both individual and combined additions refine the grain size and β-$Mg_{17}Al_{12}$ phase, which is more pronounced with combined additions. Besides, α-Mg and β-$Mg_{17}Al_{12}$ phases, a new reticular Al_2Ca and rod-shaped Mg_3Sb_2 phases are formed following individual additions of Ca and Sb in the AZ91 alloy. With combined additions, an additional Ca_2Sb phase is formed suppressing Mg_3Sb_2 phase. Additions of both Ca and Sb increase yield strength (YS) at both ambient and elevated temperatures up to 473 K. However, both ductility and ultimate tensile strength (UTS) decrease first up to 423 K and then increase at 473 K. The increase in YS is attributed to the refinement of grain size, whereas, ductility and UTS are deteriorated by the presence of brittle Al_2Ca, Mg_3Sb_2, and Ca_2Sb phases. The best tensile properties are obtained in the AZXY9110 alloy owing to the presence of a lesser amount of brittle Al_2Ca, and Ca_2Sb phases resulted from the optimum

content of 1.0Ca and 0.3Sb (wt.%). The fracture surface of the tensile specimen tested at ambient temperature reveals cleavage failure that changes to quasi-cleavage at 473 K. All the modified alloys exhibit superior creep resistance than the base AZ91 alloy. The combined additions of Ca and Sb are more effective in improving creep resistance than the individual additions. Individual Ca added AZX911 results superior creep resistance than the Sb added AZY911 is owing to the higher thermal stability of the Al_2Ca phase in the former alloy compared to that of the Mg_3Sb_2 phase in the later one. The AZXY9120 alloy pertaining 2.0Ca and 0.3Sb (wt.%) exhibit the best creep resistance due to reduced amount of β-$Mg_{17}Al_{12}$ phase and presence of higher amount of dense network of thermally stable Al_2Ca phase at grain boundaries. Post creep microstructural observation confirms the ability of the Al_2Ca phase to withstand applied high stresses at elevated temperature without undergoing significant changes in its structure. The values of stress exponents and activation energies are in the range of 4.3 to 6.5 and 111.9±1.1 to 114.9±3.0 kJ/mol, which concludes dislocation climb controlled by pipe diffusion is the dominant creep mechanism for all the alloys in the temperature and stress level employed. The observed trend in creep rates with respect to the individual and combined additions of Ca and Sb in the AZ91 alloy was further confirmed by carrying out conventional compressive creep tests on all the alloys. It has been observed that the trend in creep rates, i.e., impression velocities in impression creep, and strain rates in compression creep obtained with respect to the individual and combined additions of Ca and Sb to the AZ91 alloy is the same. Corrosion resistance of all the modified alloys is better owing to the refined and reduced volume fraction of β-$Mg_{17}Al_{12}$ phase as well as grain refinement. Individual additions are better than mixed additions. The AZX911 alloy comprising individual Ca addition with a continuous network of Al_2Ca phase reveals the lowest corrosion rate. Among the alloys comprising combined additions, the AZXY9120 alloy exhibits the best corrosion resistance due to higher and lower volume fraction of Al_2Ca and Ca_2Sb phases, respectively.

To conclude, the individual and combined additions of Ca and Sb to the AZ91 alloy resulted in improved ambient and elevated temperature tensile properties as well as impression and compression creep behaviour without deteriorating corrosion resistance. Among the modified alloys, the AZXY9120 alloy exhibited the best properties considering its targeted powertrain application at elevated temperature. In addition, the tensile and creep properties

of the squeeze-cast alloys in the present investigation were superior as compared to that of the alloys developed by gravity-cast.

Keywords: Magnesium alloy; AZ91; Squeeze-casting; Microstructure; Tensile properties; Impression creep; Corrosion

Contents

List of Figures

List of Tables

Chapter 1

Introduction

1.1 Introduction

In the past few years, the application of magnesium (Mg) alloys in the automotive industry have increased significantly owing to their high specific strength resulting in considerable increased fuel efficiency and reduced emissions. The major growth areas for Mg alloys in automobile use are the powertrain applications where mechanical properties including creep resistance in the temperature range of 423-573 K is a major requirement [1,2].

Conventional Mg alloys, i.e., AZ91D, AM50A and AM60B offer an excellent combination of ambient temperature strength and ductility, good corrosion resistance and good die-castability. However, they do not exhibit the required elevated temperature performance. Among these, AZ91 is still a workhorse alloy for automobile industries and its use is limited to interior parts that are mostly die-cast [3]. Unfortunately, this alloy has drawbacks of a drastic reduction in tensile properties and creep resistance above 393 K [3,4], which made it inadequate for major powertrain applications. The AZ and AM alloys, the most common Mg die-cast alloys, exhibit poor creep resistance at elevated temperature because of softening of the β-$Mg_{17}Al_{12}$ phase present along grain boundaries.

In order to overcome this shortcoming, less Al containing alloy series AS (Mg-Al-Si) and AE (Mg-Al-RE) having improved high temperature properties were developed. The AS series exhibit only marginal improvement in creep resistance, whereas, AE series are expensive [5]. In addition, these alloys lack in castability compared to the AZ91 alloy. Accordingly, their application is restricted to complex cast components. Over the years, many experimental Mg alloys (such as Mg-Al-Ca, Mg-Al-Sr, Mg-Al-Ca-Sr and so on) having superior creep resistance were developed. These are not yet commercialized on account of their poor die-castability.

During the past two decades, several attempts were made to modify the microstructure of AZ91 alloy through alloying additions in order to improve its high temperature properties [6]. The additions of the alloying elements mainly form a thermally stable intermetallic with Mg and Al at grain boundaries, and they provide an effective barrier for dislocation and grain boundary movement even at a higher temperature. A review of the alloying additions to AZ91 alloy concludes that the individual additions of Ca and Sb are more effective in enhancing creep resistance owing to the presence of higher melting point Al_2Ca (M. P. 1352 K) and Mg_3Sb_2 (M. P. 1501 K) phases formed following the additions of Ca and Sb, respectively. It was observed that some combined additions were more effective in enhancing ambient and elevated temperatures mechanical properties including creep behaviour [7–11]. Therefore, combined additions of Ca and Sb to AZ91 alloy will bring plausible improvement in the above-mentioned properties as well, which is investigated in the present thesis.

Individual additions of Ca and Sb are detrimental to ambient temperature mechanical properties caused by the unfavourable morphologies of the second phases formed following their additions [12–16]. Moreover, Ca adversely affect the castability of AZ91 alloy due to its high viscosity [17], which restricts the fabrication of Ca and Sb added AZ91 alloy-based components by die-cast. Therefore, it is essential to develop alternative casting processes for these alloys to ensure better castability, ambient and elevated temperatures mechanical properties including creep behaviour by modifying their microstructures.

Squeeze-casting is regarded as a combination of casting and forging processes in which molten metal is solidified under applied pressure. Application of pressure on molten metal during solidification might change the melting point, solidification rate, microstructural refinement, reduction of gas and shrinkage porosities. Thus, components fabricated by squeeze-casting generally exhibit superior mechanical properties and casting soundness in comparison with the conventional casting processes. Therefore, squeeze-casting can be regarded as a potential alternative casting process for producing defect free, near-net shape AZ91-Ca-Sb alloy-based components bearing superior mechanical properties.

1.2 Objectives of the present thesis

The objective of the present work is to understand and evaluate the effects of combined additions of Ca and Sb on microstructure, ambient as well as elevated temperature tensile properties, creep, and corrosion behaviour of squeeze-cast AZ91 alloy developed for possible automobile powertrain applications. For comparison, the same has also been studied on the squeeze-cast AZ91 alloy with and without individual additions of Ca and Sb. The salient objectives of the thesis are as follows:

1. Synthesis of Ca and/or Sb added AZ91 alloy by squeeze-cast.
2. Characterization of microstructures of all the fabricated alloys.
3. Evaluation of ambient and elevated temperature tensile properties of the alloys.
4. Detailed investigation of creep behaviour of the alloys.
5. Study of electrochemical corrosion behavior of the alloys.
6. Correlation of microstructures with creep, tensile and corrosion behaviour of all the alloys.

1.3 Structure of the thesis

The present thesis consists of eight chapters, and the contents of each chapter are as follows.

Chapter 1 briefly introduces the importance of the problem and states the objective of the present thesis.

Chapter 2 deals with the review of literature relevant to the present work and provides the motivation behind the present work.

Chapter 3 provides the details of materials and experimental procedure employed.

Chapter 4 describes the microstructural characterisation of all the fabricated alloys.

Chapter 5 discusses the ambient as well as elevated temperature tensile properties of all the alloys.

Chapter 6 describes the in-depth impression creep behaviour with emphasis on the dominant mechanism controlling creep deformation of all the alloys. This chapter also concerns with creep behaviour of all the fabricated alloys using compressive creep.

Chapter 7 provides a detailed investigation of electrochemical corrosion behaviour of all the alloys.

Chapter 8 summarizes the major conclusions arising out of the present work.

Appendix I provides a glimpse of the chronological development of alloying additions to the AZ91 alloy.

The references cited in the entire thesis are enlisted under ‘References’ provided after Appendix I.

Chapter 2

Literature review

In this chapter, a detailed background of the literature relevant to the present thesis is presented. A brief introduction to magnesium and its alloy is incorporated at the beginning. Followed by a brief theory on tensile properties with the current state of research on the tensile behaviour of the base AZ91 as well as modified AZ91 alloys is presented. At the third section of this chapter, a concise theory on creep along with the current state of research on the creep behaviour of the base AZ91 and its modified AZ91 alloys is presented. A brief theory on corrosion of metallic materials with the summary of research on the corrosion behaviour of the base AZ91 as well as modified AZ91 alloys is presented following creep behaviour. Finally, at the end of this chapter motivation behind this work is concluded based on the literature review presented.

2.1 Magnesium and magnesium alloys

2.1.1 Properties of pure magnesium

Magnesium (Mg) is having a density of 1.74 g/cm^3 that is about two-third of the density of aluminium (2.71 g/cm^3) and one-fourth of the density of iron (7.87 gm/cm^3). It is abundant in earth crust and also available in ocean water. The atomic number of Mg is 12, and it belongs to group II in the periodic table. It has hexagonal close-packed (HCP) crystal structure with lattice parameters, a = 0.321 nm and c = 0.521 nm. The c/a ratio of Mg is 1.624 which is the nearest to that of the ideal c/a ratio 1.633 for HCP crystal. According to von-Mises' criterion, minimum five independent slip systems must be operative for obtaining deformation in a polycrystalline material. Unfortunately, Mg has only two independent slip systems at room temperature. Therefore, activation of non-basal slip systems and/or twinning are necessary for obtaining significant deformation in it [18]. The strength of pure Mg is not sufficient for commercial applications. Therefore, Mg is always alloyed with other alloying elements like aluminium, zinc, calcium, silicon, rare earth, antimony, strontium, manganese and so on.

2.1.2 Designation of magnesium alloys

There is no well-established designation system for Mg alloys. However, American Society for Testing and Materials (ASTM) established some conventions. According to this, each Mg alloy is represented by two alphabets that specify the main alloying elements followed by numbers that represent the content of these elements in weight percentage. If the percentages of the two alloying elements are equal, the letters are arranged alphabetically. The designation of Mg alloy is generally followed by an alphabet that specifies the purity level of the alloy. Moreover, temper designation followed are in accordance with the ASTM B296 standard. A dash is used to separate the alloy from its temper designation. Table 2.1 shows the abbreviations used for the various alloying elements added to Mg as per ASTM B275 standard. For example, the designation AZ91D-T6 implies that the alloy contains 9.0Al and 1.0Zn (wt.%). The purity level of the alloy is represented by D, and it is in T6 condition, i.e., artificially aged.

Table 2.1: Abbreviation used for various alloying elements added to Mg alloys [19,20]

Alphabet	Alloying Element	Alphabet	Alloying Element
A	Aluminium	N	Nickel
B	Bismuth	P	Lead
C	Copper	Q	Silver
D	Cadmium	R	Chromium
E	Rare earths	S	Silicon
F	Iron	T	Titanium
H	Thorium	W	Yttrium
K	Zirconium	Y	Antimony
L	Lithium	Z	Zinc
M	Manganese		

2.1.3 Classification of magnesium alloys

According to processing method employed, Mg alloys are divided into two groups, i.e., cast alloys and wrought alloys. Cast Mg alloys are further subdivided into two groups:

(a) Zirconium containing alloys, and

(b) Zirconium free alloys

2.1.3.1 Zirconium containing alloys

Zirconium (Zr) is an effective grain refiner for Mg alloys. It has the maximum solubility of 0.6 (wt.%) in molten Mg. The strength of Mg-Zr binary alloy is not adequate for commercial applications. Therefore, alloying addition is the basic necessity to improve its strength. The addition of Al in Mg-Zr binary alloy reduces the solid solubility of Zr in Mg by forming an Al-Zr-based intermetallic, hampering the efficiency of Zr addition. There are several investigations that reported a beneficial effect of Zr along with other alloying additions in Mg. Ternary Mg-RE-Zn alloys have good castability and mechanical properties, and further improvements were observed with Zr addition. For example, the EZ33 (Mg-3.0RE-2.5Zn-0.6Zr) (wt.%) alloy exhibited very good strength and creep resistance up to 523 K [21]. Similarly, commercially available WE54 (Mg-5.0Y-4.0RE-0.5Zr) (wt.%) alloy provided high strength at ambient temperature, and excellent creep properties at elevated temperature (up to 573 K) [22]. Improved ambient and elevated temperature properties were also observed in QE22 (Mg-2.5Ag-2RE-0.7Zr) (wt.%) and HK31 (Mg-3Th-0.7Zr) (wt.%) alloys [4,23]. Most of the Zr containing alloys found applications in aerospace industry where they are extensively used to manufacture rotor heads of helicopters, landing wheels and gearbox housings of aircrafts.

2.1.3.2 Zirconium free alloys

Aluminium (Al) is the main constituent of Zr free Mg alloys. They are based on Mg-Al system and exhibit good castability and a wide range of mechanical properties. These alloys are frequently employed in die-cast applications.

The most commonly used Mg alloys AZ91, AM50, and AM60, are based on Mg-Al binary phase system. The maximum solubility of Al in Mg is 12.7 (wt.%) at a eutectic temperature (710 K). The solubility of Al progressively decreases to 2.9 (wt.%) at 473 K and below 2.0 (wt.%) at room temperature [20,24,25]. At a temperature of 710 K, β-$Mg_{17}Al_{12}$ phase formation takes place with an Al concentration of about 32.3 (wt.%). The β-$Mg_{17}Al_{12}$ phase favourably precipitates at grain boundaries during cooling. Eutectic morphology is greatly influenced by the amount of Al and rate of cooling [26]. Alloys containing more than 2.0Al (wt.%) exhibits diverse β-$Mg_{17}Al_{12}$ phase morphologies. Two morphologies, i.e., partially divorced and fully divorced eutectic are frequently revealed by the β-$Mg_{17}Al_{12}$ phase. Connected alternate layers of eutectic α-Mg and β-$Mg_{17}Al_{12}$ phases are portrayed as partially

divorced, whereas, complete separation of these two phases termed as fully divorced eutectic. Although Mg-Al alloys are heat treatable yet the effectiveness of solutionizing and aging are meagre owing to the inconsistent formation of the β-$Mg_{17}Al_{12}$ precipitate [26,27]. Brittleness of the intermetallic β-$Mg_{17}Al_{12}$ phase reduces ductility of the alloy, however, improves its strength. The presence of higher amount of Al in the alloy leads to the higher β-$Mg_{17}Al_{12}$ phase formation, consequently greater UTS, and YS.

Mg-Al binary alloys have a good blend of castability and mechanical properties. However, almost all Mg-Al-based commercialised alloys are ternary and quaternary alloy systems. A small amount of Zn, Mn, REs, Si, Ca and so on are added to enhance specific properties to make the alloys more suitable for end applications. These alloying elements also alter the solidification behaviour of the alloys. The AZ series (Mg-Al-Zn), AM series (Mg-Al-Mn) and AE series (Mg-Al-RE) are some of the commercialised Zr free Mg alloys used in automobile, aerospace and electronics industries [28].

2.1.4 AZ91 alloy

The AZ91 (Mg-9.0Al-1.0Zn-0.3Mn) (wt.%) is the most popular Mg alloy. The presence of Al in the AZ91 alloy increases its strength by solid solution strengthening and also enhances its fluidity during casting. The addition of Zn to AZ91 alloy too improves its strength by solid solution strengthening owing to the excellent solubility of Zn in Mg. However, Mg-Al alloys with high Zn content is susceptible to hot cracking. The addition of small amount of Mn to Mg-Al-Zn alloy enhances its corrosion resistance. Mn reacts with Fe present in the alloy as impurities and forms AlMnFe ($Al_8(Mn, Fe)_5$) intermetallic that settles at the bottom of the melt [29].

Luo [30] studied solidification kinetics of the AZ91 alloy. He observed a partially divorced eutectic α-Mg + β-$Mg_{17}Al_{12}$ along with lamellar β-$Mg_{17}Al_{12}$ phase, precipitating at a very slow cooling rate (0.03-0.4 °C/s) typically found in sand casting. The eutectic formation is a secondary process under non-equilibrium conditions, chasing primary solidification. As the amount of remaining liquid is meagre in this case, degeneration of the lamellar eutectic structure takes place, and it is expected that the lamellar eutectoid $Mg_{17}Al_{12}$ is formed through discontinuous precipitation from the supersaturated α-Mg matrix. Such precipitates

disappear from the microstructure when solidification rate is high. The obtained equilibrium liquidus and solidus temperatures of β-$Mg_{17}Al_{12}$ phase for sand casting process are 873 K and 708 K, respectively. A fully divorced eutectic was observed when the solidification rates are significantly high. This situation normally arises in gravity-casting and high pressure die-casting (HPDC) processes [31]. The properties of cast AZ91 alloy are superior at room temperature, and a marginal variation is observed till 393 K. Beyond this temperature, there is a steep decrease in mechanical properties especially in creep behaviour. Softening of β-$Mg_{17}Al_{12}$ phase above 423 K was considered as the prime accused behind the instability of the alloy at elevated temperature [4,32]. The high-temperature mechanical performance of an alloy also depends on the quality of casting, grain size, presence of shrinkage, gas porosity and so on.

The development of high purity AZ91 alloy with improved corrosion resistance (i.e., AZ91D and AZ91E) is the remarkable advancement in the field of commercial Mg alloys. The AZ91 is the most popular Mg alloy since it exhibits a superior combination of castability and mechanical properties. Nowadays, a major share of Mg alloys is consumed by automobile industries. Among the commercialized Mg alloys, approximately 80% casting components are prepared from AZ91 alloy for applications up to 393 K. The use of AZ91 alloy by different automobile manufacturers are summarized in Table 2.2.

2.2 Squeeze-casting

2.2.1 Description of squeeze-casting

Squeeze-casting is regarded as a combination of casting and forging processes. The steps involved in squeeze-casting are illustrated in Fig. 2.1. In this process, molten metal is poured into a mould with least turbulence and solidification takes place under applied pressure (typically above 100 MPa). The pressure is applied until complete solidification takes place. In this process, heat transfer coefficient is extremely high because the liquid metal is pressed against the die wall.

Table 2.2: Use of AZ91 alloy in automobiles by different companies [20].

S. No.	Company	Part	Modal	Alloy
1.	Ford	Clutch housing, oil pan, steering column	Ranger	AZ91HP AZ91B
		Four-wheel-drive transfer case housing	Aerostar 1994	AZ91D
		Manual transmission case housing	Bronco	AZ91D
2.	General Motors	Valve cover, air cleaner, clutch Housing (manual)	Corvette	AZ91HP
		Induction cover	North Star V8 1992	AZ91D
		Clutch pedal, brake pedal, steering Column brackets	Oldsmobile W30, Pontiac, Buick	AZ91D
3.	Porsche AG	Wheels (7.44 kg each)	944 Turbo	AZ91D
4.	Honda	Cylinder head cover	City Turbo	AZ91D
5.	Fueling Engineering	Cylinder block, Oil Sump	5HQ	AZ91D
6.	Alfa-Romeo	Miscellaneous components (45 kg)	GTV	AZ91B

2.2.2 Advantages of squeeze-casting

Application of pressure on molten metal during solidification might change the melting point, solidification rate, microstructural refinement, reduction of gas and shrinkage porosities [33]. Thus, components fabricated by squeeze-casting generally exhibit superior mechanical properties and casting soundness in comparison with the conventional casting processes. Therefore, squeeze-casting can be regarded as a potential alternative casting process for producing defect free, near net shape alloy components bearing superior mechanical properties [34,35].

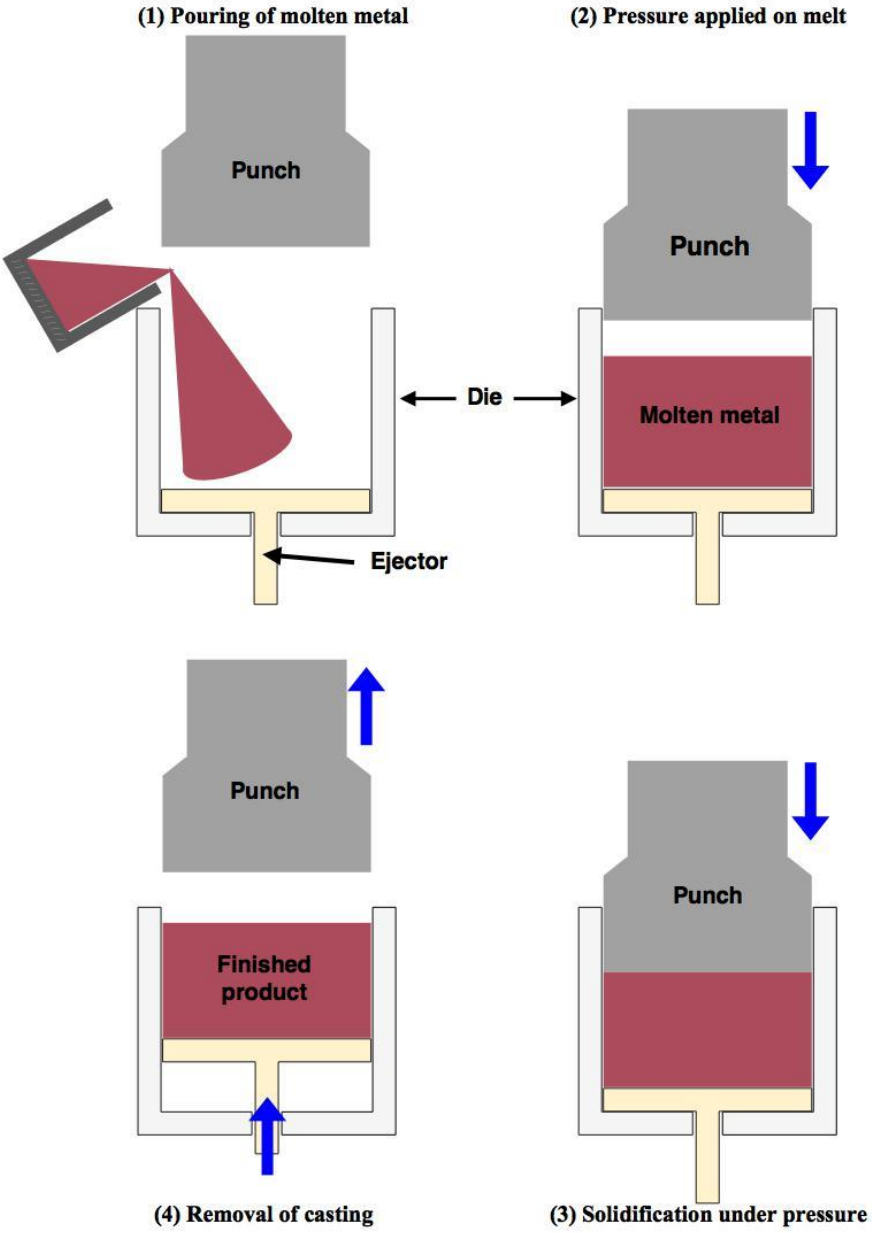

Fig. 2.1. Schematic of squeeze-casting process.

2.2.3 Research on squeeze-casting of Mg alloys

To date, the research on squeeze-cast Mg alloys is limited although potential exist to produce high-performance Mg alloys. The potential of squeeze-casting for fabrication of Mg alloys was reviewed by Luo [36] and inferred superior tensile behaviour in squeeze-cast AZ91 compared to gravity-cast and HPDC. Kleiner et al. [37] correlated microstructure and mechanical properties of the AZ91 alloy produced by squeeze-casting, rheo-casting as well as thixo-casting, and reported the best mechanical properties in squeeze-casting. Zhang et al. [17] studied microstructure and mechanical properties of Ca added AZ91D alloys and concluded better mechanical properties in squeeze-casting compared to conventional casting. Shastri [38] correlated microstructure with tensile and creep properties of AZ91 alloy produce by squeeze-casting, gravity-casting and HPDC, and reported the best properties in the squeeze-cast alloy. A similar observation, i.e., the best creep resistance of a squeeze-cast Mg-Al-Ca alloy compared to gravity-casting and HPDC was reported by Zhu et al. [39] as well. Chen et al. [40] inferred better tensile properties of squeeze-cast solid extrusion compared to thixo-forged AZ91D-RE alloy. Goh et al. [41] investigated the effect of pressure as well as melt and mould temperature on mechanical properties of the squeeze-cast AZ91-2Ca alloy and concluded microstructural refinement controlled by mould and melt temperature resulted in better mechanical properties of the alloy. Han et al. [42] studied the effect of pressure on the microstructure of squeeze-cast AZ91D alloy, and showed refined grains and increased eutectic fraction with an increase in applied pressure. Lee et al. [43] investigated the influence of Nd, Sr, and Y on micro-mechanism of fracture of squeeze-cast AZ91 alloys. A detailed microstructural analysis following squeeze-casting of the AZ91D alloy was carried out by Yang et al. [44]. Han et al. [45] studied microstructure and correlated hardness with YS of squeeze-cast AZ91 alloy. Kurnaz et al. [46] investigated the influence of Ti and Cr addition on the microstructure and mechanical properties of the squeeze-cast Mg-6Al alloy.

2.3 Tensile properties

The tensile test is largely implemented in order to select materials for various engineering applications, quality inspections and develop new materials. The data acquired from the test are generally plotted as stress vs. strain. A typical stress-strain curve is shown in Fig. 2.2. In the elastic region, stress in the material is directly proportional to the strain, and the material reverts back to its original position once the load is removed.

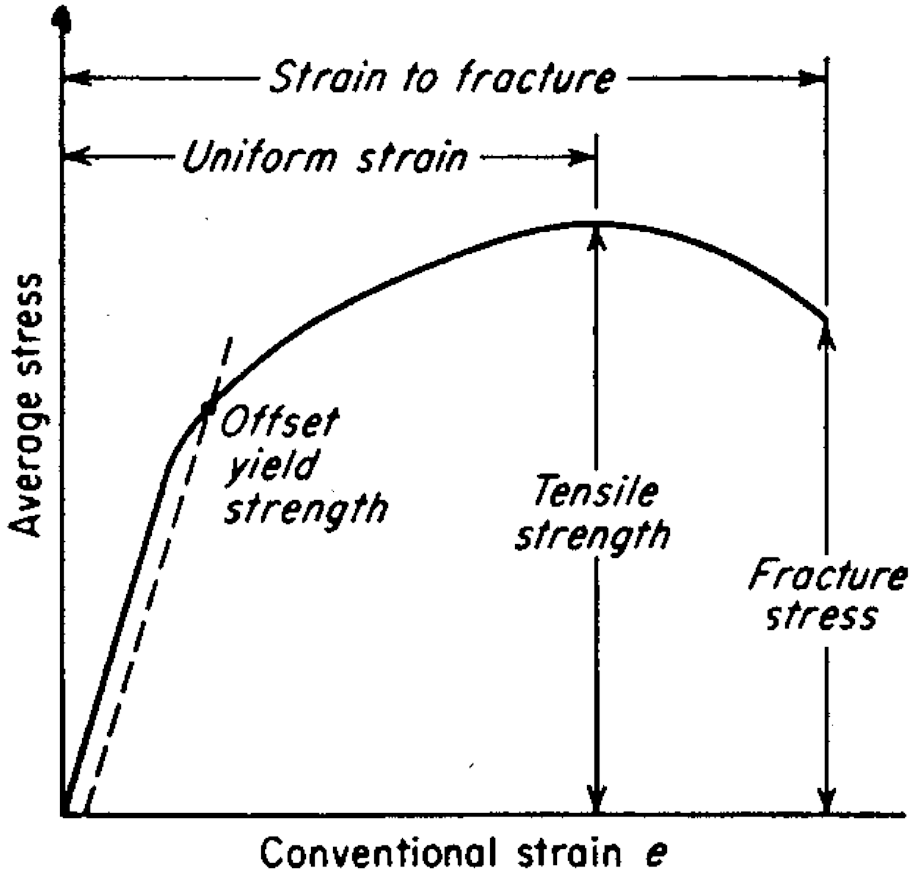

Fig. 2.2. Typical stress strain curve [18].

The material undergoes permanent plastic deformation as the stress exceeds its YS. If the load is removed in the plastic region, the material will always have certain amount of plastic deformation. For materials having an undefined yield point, the yield point is defined by 0.2% proof stress. The stress increases with increasing plastic strain to produce plastic deformation, and the material becomes strain hardened. To keep the overall volume constant, the cross-sectional area of the gauge length decreases uniformly with an increase in length. The initial strain hardening is more and not compensated fully by the decrease in cross-sectional area consequently; stress rises with increasing strain. Finally, a point is reached where stress generated from strain hardening is lower than the increase in stress due to a decrease in specimen cross-sectional area. This situation results necking. Plastic deformation is concentrated at the relatively weaker point of the material. A rapid decrease in the cross-sectional area taking place and the actual load required for deformation decreases continuously until a fracture occurs.

2.3.1 Tensile behaviour of AZ91 alloy

The microstructure of AZ91 alloy consists of α-Mg and β-$Mg_{17}Al_{12}$ phases. The β-$Mg_{17}Al_{12}$ is the main strengthening intermetallic phase during the deformation of the AZ91 alloy. The HCP crystal structure of α-Mg is mismatched with BCC crystal structure of β-$Mg_{17}Al_{12}$ phase, which increases the fragility of the α-Mg/β-$Mg_{17}Al_{12}$ interface. The β-$Mg_{17}Al_{12}$ is metastable, soft and relatively low strength phase of AZ91 alloy and gets completely dissolve during heat treatment [26]. The α-Mg/β-$Mg_{17}Al_{12}$ interface and the β-$Mg_{17}Al_{12}$ phase are prone areas for microcrack initiation [47]. All these factors contribute to poor tensile properties of the AZ91 alloy. Also, the morphology and volume fraction of the β-$Mg_{17}Al_{12}$ phase have a profound effect on the mechanical properties of the AZ91 alloy. Other factors, which affects the strength and ductility of AZ91 alloy, are the presence of alloying elements in solid solution, the formation of second-phase during solidification, heat-treatment, grain refinement, porosity, and solidification rate [48]. As reported by Shastri [38], squeeze-cast AZ91 alloy exhibited superior mechanical properties than gravity-cast and HPDC due to higher solidification rate and extremely low level of porosities. Several techniques were employed to improve the mechanical behaviour of the AZ91 alloy in the recent past. A brief summary of the various attempts to improve the performance of the AZ91 alloy is presented here.

Fabrication of AZ91 alloy by some new casting techniques and their effect on mechanical behaviour are illustrated in some literature. Application of pressure during solidification of the melt assisted in grain refinement. The tensile properties of HPDC AZ91 alloy at different locations of the casting were studied by Prakash et al. [49]. The better YS, UTS, fracture strain and ductility for the edge region than the middle region of the casting were attributed to the fine grain size, the negligible size of pores and lower clustering nature of microporosity and β-$Mg_{17}Al_{12}$ phase. The tensile behaviour of directionally and non-directionally solidified AZ91 alloy was studied by Mabuchi et al. [50]. Directionally solidified AZ91 alloy consisting of elongated grains resulted in higher strength at room temperature and 473 K than the non-directionally solidified AZ91 alloy owing to the suppressed grain boundary sliding. Zhang et al. [51] fabricated the ultrafine-grained (0.3–1.3 μm) AZ91 alloy by powder extrusion and reported a significant improvement in YS (360–478 MPa) and moderate improvement in ductility (6–8%). The high strength could be attributed to a combined effect of grain refinement and precipitation hardening. The microstructure and mechanical properties of the AZ91 alloy prepared by spray forming with subsequent extrusion were investigated by Li et al. [52]. Homogeneous, equiaxed and fine grain structure along with reduced divorced eutectic β-$Mg_{17}Al_{12}$ phase at the grain boundary resulted in an enhanced combination of toughness and strength. The room temperature UTS, YS and elongation of the alloy are 435 MPa, 360 MPa, and 9.2%, respectively. Park et al. [53] investigated the microstructure, and mechanical properties of the strip cast AZ91 alloy. The microstructure of the alloy was fine and equiaxed dendritic structure with the variation of secondary dendrite arm spacing throughout the thickness. They reported the best combination of tensile properties in T4 condition resulted from the presence of Al−Mn particles. Like pressure, application of ultrasonic vibration during solidification also has a significant effect on the mechanical behaviour of the AZ91 alloy. Gao et al. [54] as well as Aghayani and Niroumand [55] subjected the AZ91 melt to different power levels of ultrasonic vibration during solidification and studied its microstructures and mechanical properties. The cavitation and streaming phenomena of ultrasonic treatment provided smaller, more rounded and better-distributed grains resulted in significant improvement in tensile strength with the increase in applied ultrasonic power. Also, the acoustic streaming generated by ultrasonic vibrations reduced the Al segregation at grain boundaries resulted in low volume fraction of β-$Mg_{17}Al_{12}$ phase [56]. Variation in microstructure and tensile properties by the secondary processing of AZ91 alloy was the subject of various studies. A significant improvement in YS, UTS, and ductility of the AZ91 alloy was observed after the

alloy was subjected to equal channel angular processing (ECAP) owing to the fine grain microstructure. Mabuchi et al. [57] observed that the alloy with non-equilibrium grain boundary structures exhibited lower superplastic elongation than the alloy with equilibrium grain boundaries [58]. Chen et al. [59] investigated the influence of ECAP on microstructure and mechanical properties of a hot-rolled AZ91 alloy and reiterated that the mechanical behaviour of the ECAP-processed alloy was strongly influenced by the morphology of the β-$Mg_{17}Al_{12}$ phase. Ding et al. [60] studied the microstructure, texture and tensile properties of extruded AZ91 alloy. Extrusion promotes the occurrence of dynamic recrystallization, precipitation of β-$Mg_{17}Al_{12}$ phase and the formation of basal texture. They observed a decrease in tensile strength and increase in ductility with the increase of either the extrusion temperature or extrusion ratio. The increase in elongation attributed to the deformation twinning. Cavaliere et al. [61] and Zhang et al. [62] used the friction stir processing (FSP) to refine the microstructure of the AZ91 alloy prepared by HPDC and gravity-casting. They reported that friction stir processed AZ91 alloy showed good strength and ductility at ambient temperature due to the very fine structure. The microstructure, mechanical properties, and tensile fracture behaviour of electropulsing treated and subsequently aged AZ91 alloy were investigated by Jiang et al. [63]. Spheroidizing and dissolution of β-$Mg_{17}Al_{12}$ phase due to electropulsing treatment (EPT) and ageing remarkably increased the elongation to failure without altering the tensile strength of the alloy. The effect of microporosity on the tensile deformation of the as-cast AZ91 alloy was investigated by Lee and Shin [64]. They observed a strong inverse parabolic dependence of UTS and elongation on microporosity variation, whereas, the YS depends linearly on the load carrying capacity. Lee [65] studied the correlation of microporosity with grain size in HPDC and gravity-casting AZ91 alloy. They reported the effect of microporosity on the UTS and elongation increased with the increase in grain size.

2.3.2 Tensile behaviour of modified AZ91 alloys

The AZ91 alloy is usually alloyed with several surface-active elements like Bi, Ca, RE, Sb, Sr and so on to improve its mechanical properties. Guangyin et al. [7] investigated the tensile properties of Bi added AZ91 alloy. They reported a new Mg_3Bi_2 phase at the grain boundaries along with the β-$Mg_{17}Al_{12}$ phase. The melting point of Mg_3Bi_2 phase is 1096 K. The formation of thermally stable Mg_3Bi_2 phase and reduction of β-$Mg_{17}Al_{12}$ phase at the grain boundaries significantly improved elevated temperature tensile properties preventing

grain boundary sliding. The addition of Ca in AZ91 alloy refined the grains, reduced the volume fraction of β-$Mg_{17}Al_{12}$ phase and eliminate the discontinuous precipitations of β-$Mg_{17}Al_{12}$ phase [66,67]. Up to a certain limit, an increase in UTS and ductility was observed. Alloy containing high Ca content become more susceptible to hot tearing [14]. Improvement in YS was attributed to reduced grain size. Diminishing the oxidation tendency of the AZ91 alloy by Ca addition was an added advantage [68,69]. Zhang et al. [17] reported further improvement in mechanical properties of the squeeze-cast AZ91-Ca alloy processed under high applied pressure. The α-Mg grains turned into the rosette-like structure when pouring temperature of the melt was almost equal to the liquidus temperature. Therefore, alloys processed by squeeze-casting can provide better mechanical properties. In addition, some amount of Ca was trapped in β-$Mg_{17}Al_{12}$ phase, which helped to improve its thermal stability [70]. It was also observed that the combined additions of Ca and Si was more effective in increasing the tensile strength at ambient and elevated temperature [66]. Effect of RE addition in AZ91 alloy was the subject of several studies in recent past. Successive improvement in YS and UTS up to 2.0RE (wt.%) addition to AZ91 alloy at a temperature of 413 K was observed by Khomamizadeh et al. [71]. Replacement of β-$Mg_{17}Al_{12}$ phase by thermally stable RE containing intermetallics provided the necessary grain-boundary strengthening and restricted the flow of grain boundaries at elevated temperature. The improved performance of RE containing AZ91 alloy was due to its ability to retain fine microstructure and ultimate shear strength even after long term annealing at 693 K. The addition of RE beyond 2.0 (wt.%) increased the brittleness and reduced the strength because of the growth of sharp edged $Al_{11}RE_3$ brittle phase, yet the modified alloy had better strength than the base AZ91 alloy [72]. Wang et al. [73] studied the effect of Sb addition to the AZ91 alloy. They reported an increase in tensile strength and elongation up to a certain level of Sb addition in the temperature range of 298-423 K owing to refined grains, refined and granulated β-$Mg_{17}Al_{12}$ phase as well as coarse needle-shaped Mg_3Sb_2 phase. Srinivasan et al. [9] studied the effect of Si with 0.2Sb (wt.%) additions on the microstructure and mechanical properties of permanent mould AZ91 alloy. They observed an even distribution of hexagonal shaped Mg_2Si particles when Sb was added to AZ91-Si alloys. Significant improvement in strength and ductility at ambient and elevated temperature was reported. Turen [74] studied the effect of Sn addition on microstructure and mechanical properties of the AZ91 alloy. He reported β-$Mg_{17}Al_{12}$ phase refinement with improved tensile and elongation with 0.5Sn (wt.%) addition to the AZ91 alloy. The presence of clustered Mg_2Sn phase was the reason behind poor mechanical properties when Sn addition exceeded the

limit of 0.5Sn (wt.%). Zhao et al. [75] studied the effect of Sr and B additions on the microstructure and mechanical properties of the AZ91 alloy. They observed the best tensile strength owing to the presence of Al_4Sr phase at grain boundaries following the additions of 0.5Sr and 0.09B (wt.%) to the AZ91 alloy. A small amount of Sr addition helped to refine the grain size. Improvement in fluidity and reduction in solidification range was observed in the AZ91-Sr-B alloy. The role of Y, Sr and Nd additions on the microstructure and fracture mechanism of squeeze-cast AZ91-X alloys was studied by Lee et al. [43]. Additionally, the combined additions of Ca and Sb to AZ91 alloy produced by conventional casting resulted in poor mechanical properties at ambient temperature [76].

2.4 Creep

2.4.1 Definition

Creep is a time-dependent plastic deformation of a material under constant stress and temperature. It occurs at a homologous temperature (i.e., T/T_m) ≥ 0.5. The homologous temperature varies with melting point of materials and accordingly, different materials undergo creep at different temperature. For example, Pb creeps at ambient temperature whereas, Fe creeps at above 873 K. Some Ni-based superalloys can withstand temperatures as high as 1500 K, and ceramics can resist creep deformation up to 2000 K. In general, the phenomenon of creep is important at high temperature. Three stages are observed in a typical creep plot i.e. primary, secondary and tertiary stages as shown in Fig. 2.3. In the primary (or transient) creep stage, strain rate decreases with time owing to strain hardening effect. In the secondary creep stage, there is a dynamic balance between strain hardening and recovery processes resulting in a steady state region with an almost constant creep rate. Minimum creep rate is obtained from this stage. In the tertiary region, creep rate increases with time. The increase in creep rate is associated with the reduction in the cross-sectional area due to necking or internal void formation. The increase in temperature and stress reduce the duration of different creep stages [18,77]. It is evident from Fig. 2.4 that the creep rate increases with the increase in stress at a constant temperature. A similar behaviour is observed at a constant stress for different temperature as shown in Fig. 2.5.

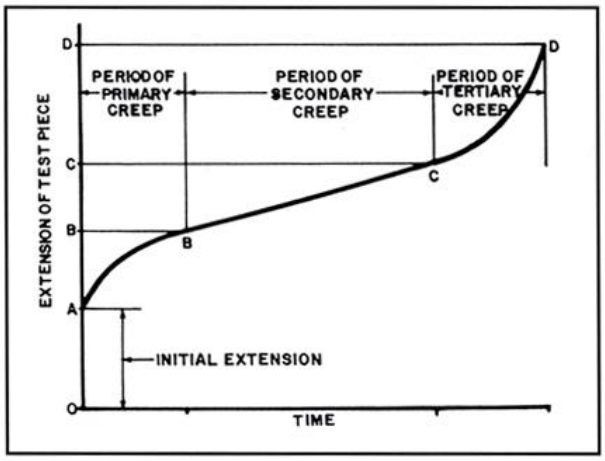

Fig. 2.3. Schematic representation of a typical creep plot [18].

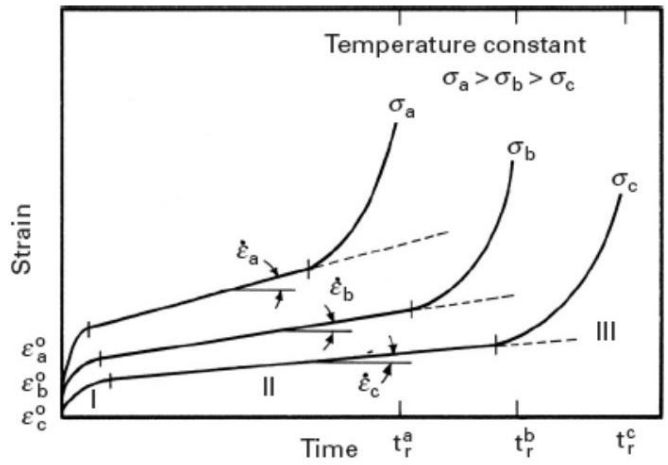

Fig. 2.4. Effect of stress on creep curves at constant temperature [78].

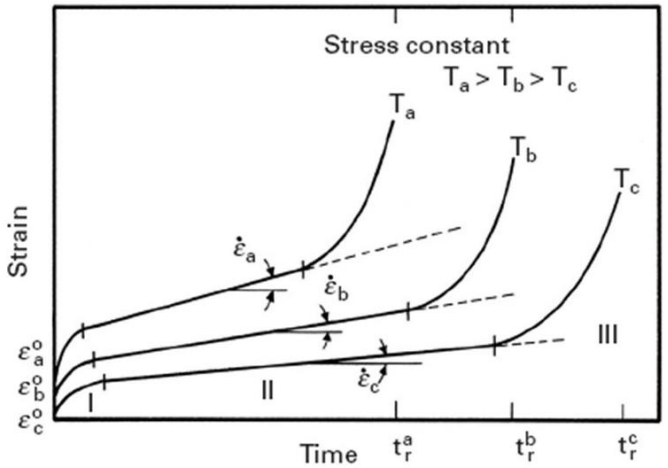

Fig. 2.5. Effect of temperature on creep curves at constant stress [78].

2.4.2 Classification of creep mechanisms

2.4.2.1 Dislocation creep

The creep deformation that takes place by the movement of dislocations is termed as dislocation creep. This mechanism of creep tends to dominate at high stresses and relatively low temperature. There are usually two varieties of dislocation creep. First, dislocations can move by gliding in a slip plane, and the process requires little thermal activation. Dislocation glide is seen to dominate in the stress range $10^{-4} < \sigma/G < 10^{-2}$. Second, dislocations can move by climb process, and it requires diffusion. Thus, the process is time-dependent and favoured only at high temperature [79].

2.4.2.2 Diffusion creep

The occurrence of creep deformation through the diffusion of atoms is termed as diffusion creep. The operating conditions of diffusion creep are low stress and high temperature. The driving force behind the process is the free energy gradient created by the applied stress. After applying a tensile load, regions parallel to the loading direction or polar region, feel tensile stress and regions perpendicular to the loading direction or equatorial region feel compressive stress. Atoms at the polar region possess lower free energy than equatorial region. Therefore, diffusion of atoms is taking place towards such regions, and this motion will lead to elongation of the grain along the loading direction. The movement of vacancies is always in the opposite direction of the atom. In this process, the grain boundaries act as source and sink of vacancies. The fine-grained material has shorter diffusion distances, which tend to make the material more susceptible to creep [80–82]. Diffusion creep is of two different types: Nabarro-Herring creep, and Coble creep. In Nabarro-Herring creep, strain rate is governed by the stress assisted the flow of vacancies through the lattice diffusion of atoms as illustrated Fig. 2.6(a). It generally occurs at a higher temperature, which is lower than 0.8 T_m and can be explained by the following constitutive equation.

$$\dot{\varepsilon} = \left(\frac{14\sigma b^3 D_l}{kTd^2}\right) \tag{2.1}$$

where σ is the applied stress, b is the burgers vector, D_l is the lattice self-diffusion coefficient, k is Boltzmann's constant, T is absolute temperature, and d is the grain diameter. In Coble creep [83], the strain rate is controlled by the diffusion of atoms through grain

boundaries as illustrated in Fig. 2.6(b). It predominantly happens at a temperature around 0.4 T_m and is explained by the following constitutive equation.

$$\dot{\varepsilon} = \left(\frac{a\sigma D_{gb} b^4}{kTd^3}\right) \qquad 2.2$$

where a is material constant, and D_{gb} is the grain boundary diffusion coefficient. Finer the grain size, higher is the creep rate. Grain size effect is more significant in Coble creep than Nabarro-Herring creep.

2.4.2.3 Grain boundary sliding

The occurrence of creep deformation by the movement of grain boundaries in their own plane (sliding) or normal to it (migration) under applied shear stress is termed as grain boundary sliding or migration. This deformation process generally occurs at low stress and high homologous temperature. It is basically an important strain-producing process in superplastic deformation. It does not have a significant role during primary or secondary creep, however; it contributes to the initiation and propagation of intercrystalline cracks during tertiary stage of creep. The grain-boundary sliding rate is controlled by the accommodating processes where the sliding surface deviates from a perfect plane. Lifshitz [84] explained that the vacancy diffusion under applied stress is the principal reason for grain boundary displacement. This type of sliding exclusively occurs in Nabarro-Herring and Coble creep.

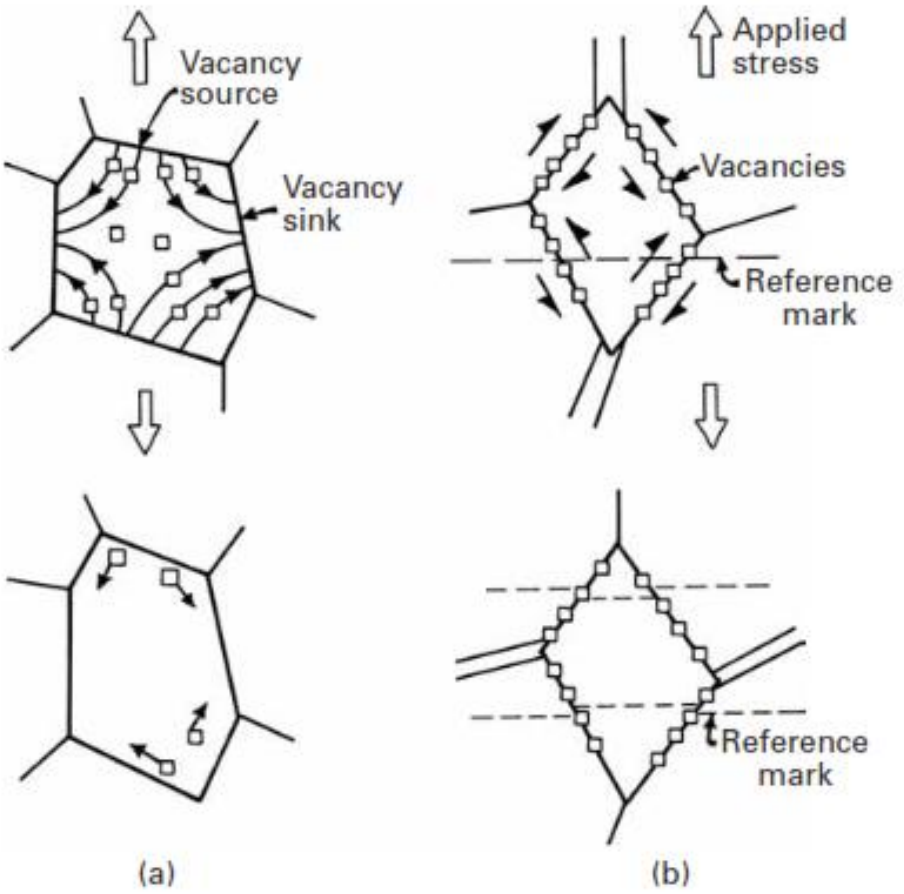

Fig. 2.6. Representation of (a) Nabarro-Herring creep and (b) coble creep [78].

2.4.3 Assessment of creep mechanism

The creep deformation of the material is directly associated with underlying microstructure. At constant stress, the steady state strain rate is given by [85]

$$\dot{\varepsilon}_s \propto \exp\left(\frac{-Q}{RT}\right) \quad 2.3$$

where $\dot{\varepsilon}_s$ is the steady state strain rate, Q is the activation energy for creep, R is the universal gas constant (8.314 J/mol.K), and T is the absolute temperature. At constant temperature, the steady state strain rate is given by [86]

$$\dot{\varepsilon}_s \propto \sigma^n \quad 2.4$$

where n is the stress exponent. The combined form of equation 2.3 and 2.4 is given in equation 2.5.

$$\dot{\varepsilon}_s = A_0\sigma^n \exp\left(\frac{-Q}{RT}\right) \quad 2.5$$

where A_0 is a constant. This is an Arrhenius type equation and known as power law creep equation. The value of activation energy Q is correlated with the underlying diffusion process. It is reported that the activation energy for creep for pure metal is nearly equal to the activation energy required for self-diffusion [87,88]. Based on the values of n and Q determined from equation 2.5 over a temperature and stress range, the dominant creep mechanism is concluded. The most general description of the creep constitutive equation is provided by Mukherjee et al. [89], and it is well known as the Mukherjee-Bird-Dorn equation.

$$\dot{\varepsilon} = A\left(\frac{b}{d}\right)^p \left(\frac{GbD_0}{kT}\right)\left(\frac{\sigma}{G}\right)^n \exp\left(\frac{-Q}{RT}\right) \quad 2.6$$

where D_0 is a pre-exponential factor (frequency factor), and p is the grain size exponent. It is evident from equation 2.1, 2.2 and 2.6 that the predicted stress exponent value for all types of diffusion creep is unity and p is 2 for Nabarro-Herring creep, and 3 for Coble creep. The values of n vary from 3 to 7 for dislocation creep.

2.4.4 Creep behaviour of AZ91 alloy

There were several papers published on creep behaviour of AZ91 alloy [4,90–93]. However, the creep deformation mechanism of the alloy is still under debate. The presence of β-$Mg_{17}Al_{12}$ phase is associated with lower creep resistance. It was suggested that creep resistance of the alloy was reduced by softening of the β-$Mg_{17}Al_{12}$ phase at elevated temperature, which allowed easy grain boundary sliding. Dargusch et al. [94] noted that the poor creep resistance of the alloy could be attributed to the discontinuous precipitation of β-$Mg_{17}Al_{12}$ phase in areas that had previously been regions of highly supersaturated α-Mg. Regev et al. [95] studied the creep behaviour of die-cast AZ91 alloy and reported lower creep rate and higher elongation to fracture than that of pure Mg. The proposed dominated creep mechanism was dislocation creep as they found stress exponent (n) varied from 5.4 to 6.9 in the temperature range from 423 to 453 K. Similarly, Blum et al. [96] also concluded dislocation creep as the dominated creep mechanism when they conducted test in the compressive creep mode in the temperature range of 343-423 K on die-cast AZ91 alloy. They did not observe the contribution of grain boundary sliding in creep deformation. Miller [97] reported creep deformation of the AZ91 alloy at room temperature at 60 MPa. According to him, the mechanism working behind the room temperature creep was the diffusion controlled dislocation climb.

Grain boundary sliding in die-cast AZ9l alloy was observed by Dargusch et al. [98], and it was preferentially dominated at low-stress level. They used 20 to 60 MPa stress and 298 to 448 K temperature range to conduct the creep experiments and the calculated stress exponent, and apparent activation energy values were 1.5 and 44 kJ/mol, respectively. The measured activation energy for a discontinuous β-$Mg_{17}Al_{12}$ precipitate in the Mg-9A1 alloy is 30 KJ/mol which is close to experimentally obtained value, i.e., 44 kJ/mol. Discontinuous precipitation was normally obtained at grain boundaries, which is not good for creep. Regev et al. [99] reported better creep performance of the gravity-cast AZ91 alloy than the die-cast AZ91 alloy. The minimum creep rate was much higher of the alloy produced by HPDC. The dynamic precipitation process of the alloys during creep imposed a marked difference in hardening mechanisms.

2.4.5 Creep behaviour of modified AZ91 alloy

The effect of different rare-earths (REs) additions on creep behaviour of the AZ91 alloy was extensively studied by several researchers. Zhang et al. [100] reported the creep behaviour of the AZ91-Y alloy at 423 K temperature and 50 MPa stress. They observed very small amount of Al_2Y phase with refined eutectic β-$Mg_{17}Al_{12}$ phase. Moreover, the morphology of β-$Mg_{17}Al_{12}$ phase changed from partially divorced to fully divorced. All these factors helped to improve creep resistance of the modified alloy significantly. The microstructure of Ce rich mischmetal added AZ91 alloy had a needle shape thermally stable $Al_{11}RE_3$ particles which reduced the susceptibility of grain boundary sliding at high temperature and the dominated deformation mechanism was dislocation climb controlled [101].

Apart from rare earth elements, Ca addition also showed the potential to improve the creep resistance of the AZ91 alloy. Amberger et al. [102] reported the formation of thermally stable Al_2Ca phase with skeleton type morphology, which is responsible for enhanced creep resistance of the alloy. When Ca was added 2.0 (wt.%) or above to AZ91 alloy, complete suppression of low melting β-$Mg_{17}Al_{12}$ phase was reported. Ca containing AZ91 alloy also showed higher stress exponent value than that of the base AZ91. Shepeleva et al. [103] investigated creep behaviour of Ca, and Ce added AZ91 alloy. They found serrated grain boundaries as a result of combine addition, which helped to reduce grain boundary sliding. Both Ca, and Ce reacted with Al and formed thermally stable intermetallics. Lower Al concentration in Mg matrix lowered the precipitation rate during high temperature exposure, and a small amount of β-$Mg_{17}Al_{12}$ phase at grain boundaries improved creep resistance of the alloys. Combine addition of Ca and lanthanum (La)-rich misch metal on creep behaviour of the AZ91 alloy was explained by Wenwen et al. [104]. They reported the small addition of Ca in AZ91 alloy did not form any new phase, but refined as-cast microstructure and improved thermal stability of β-$Mg_{17}Al_{12}$ phase. La addition produced needle-shaped $Al_{11}La_3$ particles in microstructure and remain unaffected by a solution treatment. Remarkable improvement in creep resistance was noticed when both of them were added together. Creep rate of AZ91-0.3Ca-3.0La was one order lower than the base AZ91 alloy. The addition of Ca and Sr together in AZ91 alloy also exhibited better creep resistance. Both lowering stacking fault energy by Ca/Sr addition and the presence of Mg-Al-Ca-Sr-containing intermetallic at grain boundaries assisted in the improvement of creep resistance [8]. The addition of Sb to AZ91 alloy caused the strengthening of Mg matrix and grain

boundaries effectively by the formation of some rod-shaped Mg_3Sb_2 precipitates with hexagonal D52 structure. TEM analysis of creep tested AZ91-0.35Sb alloy exhibited high concentration and low recovery of dislocations at subgrain boundaries than that of the AZ91 alloy. This was due to the effective cordon to recovery process provided by Sb-rich particles [105]. Modification of β-$Mg_{17}Al_{12}$ phase morphology and microstructural refinement by Sb addition was reported by Guangyin et al. [106]. They reported 25% decrease in creep rate of Sb-containing AZ91 alloy at 423 K and 50 MPa. Possibilities of cross slip were reduced in base AZ91 alloy by the suppression of discontinuous precipitation and formation of Mg_3Sb_2 phase. Significant improvement in creep resistance up to 473 K was noticed when Sb is added with Bi to AZ91 alloy. The calculated activation energies of all the modified alloys were very close to 135 kJ/mol that concluded dislocation climb was the dominant creep mechanism. The rod-shaped Mg_3Bi_2 and Mg_3Sb_2 phase played a crucial role in improved creep resistance [7]. The combined addition of Sb and Si to AZ91 alloy resulted in extended creep life at 423 and 473 K due to the presence of thermally stable Mg_2Si phase [10].

2.4.6 Impression creep

In impression creep test, a flat end punch of diameter 'a' with cylindrical geometry is pressed against the test material under applied pressure 'P'. The depth of penetration of the punch or impression depth 'D' is monitored with respect to time. The impression creep curve is drawn by plotting impression depth versus time. The typical punch diameter of 0.5, 1.0, 1.5 and 2.0 mm was employed depending on the application. Punch penetration depth was measured by an LVDT-amplifier assembly. The following relationships permit the comparison of data obtained by impression and conventional tensile creep tests.

$$\dot{\varepsilon} = \frac{v_s}{d} \approx \frac{v_s}{a} \qquad 2.7$$

and

$$\sigma_i = 3\sigma_t \qquad 2.8$$

where $\dot{\varepsilon} = \frac{d\varepsilon}{dt}$ is the creep rate, v_s steady state punch velocity, σ_t applied stress (tensile creep), σ_i is the punching stress in impression creep test, d is depth of plastic zone underneath the

punch. The depth of plastic zone in impression creep was observed to be equal to 'a' as obtained by metallographic investigation carried out under the punch surface [107].

It is a sophisticated experimental method, which provides numerous advantages over the conventional creep test:

1. It requires small size specimen with minimal specimen preparation and considered as an economical method for developing advanced materials.
2. The capability to achieve constant stress with a constant load makes it feasible for conducting constant stress creep test.
3. A single specimen can be used to obtain the minimum or steady state creep rate at various temperature and stress levels. Therefore, microstructural constancy facilitates easy and accurate estimation of stress exponent and activation energy for creep deformation.
4. The deformation is more stable owing to the absence of tertiary creep stage. Therefore, it can also be used to study the creep behaviour of near brittle materials.
5. This test efficiently yields information on some special studies, which is hard to acquire in conventional creep tests, like investigating the creep behaviour of distinct zones in a weld structure [107].

2.4.7 Impression creep behaviour of Mg alloy

As mentioned in the previous section, the conventional tension and compression creep tests are time-consuming and require multiple specimens. In addition, there might be specimen-to-specimen microstructural variation, which causes difficulty in studying creep mechanisms. To overcome the problem, impression creep test gained importance. The technique requires small size specimen with minimal specimen preparation [107–109]. Creep behaviour of different Mg alloys was studied successfully using impression creep technique in the recent past. Rashno et al. [110] investigated creep behaviour of the MRI153 alloy and reported the dominant creep mechanism was pipe diffusion controlled dislocation climb. The addition of Sn to MRI153 alloy deteriorated its creep resistance due to reduced amount of Al_2Ca phase resulting from the formation of a new CaMgSn phase. Calculation of creep activation energy and stress exponent suggested climb-controlled dislocation creep as the dominant creep mechanism [70]. On the contrary, better creep resistance was observed by addition of Sn in the AZ91 alloy. Sn reacted with Mg and formed thermally stable Mg_2Sn phase evenly distributed along grain boundaries. The phase provided effective resistance to the recovery process and inhibited grain boundary sliding [111]. Kabirian and

Mahmudi [112] investigated creep behaviour of the AZ91 alloy by impression creep. They stated that microstructural instability at higher temperature led to the reduction in stress exponent. Dislocation climb was the favourable mechanism for creep. Effect of additions of Ca, REs, Si, Zr on creep performance of the AZ91 alloy was studied by impression creep by several researchers [113–116]. The alloying elements produced thermally stable intermetallics that provided an efficient barrier to dislocations movement. Thus, recovery process became difficult that resulted in lower creep rate of the alloy [112]. Combined addition of Ca and RE in AZ91 alloy further improved creep resistance. The presence of $Al_{11}RE_3$ and Al_2Ca intermetallics restricted recovery process and prevented the grain boundary sliding leading to better creep resistance [114]. Creep response of AZ91-RE-Ca alloy fabricated by HPDC and thixomold castings were nearly same, and it was pipe diffusion-controlled dislocation climb [117]. Researchers also studied the creep behaviour of lower Al-containing alloys like AZ31 and AZ61 by impression creep. In the case of AZ61, the dominant creep mechanism at low stresses was dislocation climb, whereas, at high stresses, the governing mechanism was power law break down [118]. Si addition improved creep performance of the AZ61 alloy by effective pinning of grains by the formation of intermetallic Mg_2Si phase. However, the addition did not affect stress exponent and dominant creep mechanism [116]. Geranmayeh et al. [119] investigated creep behaviour of the AZ61-0.7Si alloy by using both compression and impression creep methods. Ansary et al. [120] carried out impression and tensile creep tests on the AZ31 alloy. They observed an excellent correlation of results obtained by impression creep with that obtained by other types of creep tests. The addition of Ca and Sb in Mg-5Sn alloy improved creep resistance, and it was significantly better in aged condition due to the higher volume fraction of thermally stable CaMgSn or Mg_3Sb_2 phase along with Mg_2Sn phase. The thermally stable particles promote grain boundary strengthening which minimises recovery and recrystallization processes during deformation at high temperatures as mentioned above [121]. Peng et al. [122] tested creep behaviour of the ZA84-0.5Ca alloy. Change in stress exponent with the change in stress and temperature was the general trend when power law relation was employed. Activation energy reduced with the increase in punching stress. They proposed using hyperbolic sine law instead of the conventional power law for obtaining a single value of activation energy to determine deformation mechanism more precisely.

2.5 Corrosion

2.5.1 Definition

Degradation of material or metal by means of destruction of its surface in an aggressive environment is termed as corrosion. It is either chemical or electrochemical oxidation process. The valency of metal is generally changed to positive by transfer of electrons from the metal to surrounding environment or more precisely electrolyte such as liquid, gas and hybrid soil-liquid. An electrolyte is a reservoir of positively and negatively charged ions usually entitled cations and anions, respectively. In a corrosive environment minimum two reactions, i.e., anodic and cathodic reactions are required to proceed the corrosion irrespective to chemical or electrochemical nature of the process. Oxidation of metal occurs through anodic reaction and reduction ensues via cathodic reaction [123,124].

2.5.2 Types of corrosion

No unique classifications are existing for diverse types of corrosions. Some main categories or generally adopted corrosions are explained below.

2.5.2.1 Atmospheric corrosion

Atmospheric corrosion is the most general type of corrosion attack in which a uniform layer of oxide film developed on the entire surface of the metal while exposed to the corrosive atmosphere. Steel structure with a brown colour oxide film on its surface is a common example of such type of corrosion. Ferric hydroxide had a major contribution to form that surface layer which is usually known as rust. By the use of suitable Pourbaix diagram [125], one can deduce the effective oxidation processes [123,126]. In this diagram, the electric potential of metal is represented as pH of water at ambient temperature. Possible electrochemical processes can be predicted if the pH and potential of the electrochemical system are known. Metal oxidation region, metal protection by a stable oxide film on the surface and corrosion immune regions have a distinct presence in the plot.

2.5.2.2 Galvanic corrosion

Corrosion damage induced by the coupling of two dissimilar metals in an electrolyte is termed as galvanic corrosion. This process is an electrochemical process and by the establishment of electrical contact between both the metals, one metal become anode (more

negative potential) and corrode faster than the other which serve as a cathode (more positive potential). Potential differences among different materials are the driving force of such type of corrosion. Prediction of galvanic corrosion can be accomplished by the use of electromotive force (EMF) or standard electrode potential series for metal reduction. Selection of different metals for application plays a crucial role on the possibility of galvanic corrosion. For low galvanic coupling, materials with almost similar potential should be chosen. On the other hand, the higher potential difference was used for cathodic protection purpose. In this process, metal with more negative potential sacrificed itself for protecting the more valuable metal with less negative potential. Electrochemical power sources such as batteries; fuel cells etc. are the examples of galvanic corrosion in a more general way [124,127].

2.5.2.3 Pitting corrosion

Pitting is a localized form of corrosion. The presence of holes and cavities on the metal surface are the typical demonstration of the same. Initiation of the pits on the metal surface is difficult to detect through visual inspection owing to the small size. Visibility of the holes are increased after prolong exposure time. This phenomenon is usually observed on passive metals like Al when the surface protective film destroyed by chemical or mechanical means with no immediate re-passivation. The existence of pits can take various shapes like wide, narrow, shallow or deep. These pits cause rapid perforation of wall thickness. Surface defects such as failure of protective coating, mechanical discontinuities, inclusions or the presence of heterogeneous phases in the microstructure are the favourable sites for the formation of pits. The presence of aggressive chemical species in the environment is the prime cause of pitting corrosion in the defect-free material. The formation of a differential aeration cell by the environment initiates the pit formation at the anodic site. It was assumed that many redox reactions occurred at the localized sites during the formation and growth of pits. However, the rates of those reactions are very slow, and it does not affect the corrosion progress in an inward direction much [123,128].

2.5.2.4 Crevice corrosion

It is another type of localized electrochemical attack associated with the gap or crevice remained unattended during the process of joining of two metals. The severe form of the corrosion is observed when the electrolytic solution confined and remained stagnant inside

the occluded interstices or crevices ascribable to the low-temperature oxidation as an outcome of localized anodic reactions. This type of metal oxidation process takes prolong time to start but accelerates very fast after initiation. Except for its starting stage, the propagation mechanism is very similar to the pitting corrosion. Change in chemistry inside the crevice like deficiency of oxygen, increase in hydrogen and chloride concentration, etc. facilitated to initiate this form of corrosion. Owing to the reduced amount of oxygen, the cathodic reaction for oxygen reduction slowed down inside the crevice region and metal dissolution take place [123,124,129].

2.5.2.5 Stress corrosion cracking

The process of premature failure of structural components subjected to tensile as well as the corrosive environment at a stress label below YS is termed as stress corrosion cracking (SCC). It is a type of environmentally induced failure (EIF). Other environmentally induced failure (EIF) are corrosion fatigue cracking (CFC) and hydrogen induced cracking (HIC) [130].

2.5.3 Corrosion behaviour of magnesium

The high reactivity of Mg generally makes it prone to corrosion, and it is an important issue to consider. Chloride solution, typically 0.5-3.0% NaCl, was frequently used for corrosion studies. These solutions were used to mimic the different aggressive environmental conditions like road environment in different terrain or proximity to the sea endured by the metal and alloys during service.

2.5.3.1 Mechanism of corrosion

Among all engineering materials, Mg has the lowest standard electrode potential, i.e. –2.38 V (SHE); consequently, it can reduce hydrogen even at high pH values. In the case of Mg alloys, both water and oxygen reduction can be considered as a cathodic reaction [131]. Little amount of water is always present in open atmospheric conditions and formation of water film is evident on alloy surface. The film thickness on the surface can be defined by some factors such as relative humidity, temperature, and the presence of water soluble compounds. Transportation of oxygen through this water film during atmospheric corrosion is relatively easy, and the favourable reaction is the reduction of oxygen. On the other hand,

in bulk water, oxygen supply is insufficient, and water reduction is the favourable cathodic reaction. It mostly occurs at low pH values. Both cathodic and anodic reactions are as follows:

Cathodic reaction:

Water reduction:

$$2H_2O + 2e^- \rightarrow H_2(g) + 2OH^-(aq) \quad 2.9$$

Oxygen reduction:

$$O_2 + 2H_2O + 4e^- \rightarrow 4OH^-(aq) \quad 2.10$$

Anodic reaction:

$$Mg(s) \rightarrow Mg^{2+} + 2e^- \quad 2.11$$

Electrochemical dissociation reaction of Mg in aqueous solutions formed a crystalline film of $Mg(OH)_2$ and released H_2 gas. The concentration of oxygen is relatively inconsiderate in this type of reactions. The overall reaction is shown in equation 2.12.

$$Mg(s) + 2H_2O \rightarrow Mg(OH)_2 + H_2(g) \quad 2.12$$

Advancing of corrosion increases pH value in the proximity of metal surface to around 11 as a consequence of the formation of $Mg(OH)_2$. Different exposed conditions explicitly provide the capability of the film to protect the underneath surface. It was found that if the solution contains a small volume of water with nearly no species to harm $Mg(OH)_2$ film, then Mg is very resistant to corrosion [132,133]. In working environment of engineering applications, consideration of Mg as a choice of metal is forbidden because of its utmost corrosion active nature. In some environments, its corrosion tendency is as severe as to serve as a sacrificial anode to preserve less active structure from corrosion [134,135] e.g. buried pipelines, water-cooled rolling mills, hull of the big ships and pipe from deep water wells. The more negative standard electrode potential of Mg indicates high galvanic corrosion susceptibility of its alloys. The coupling of two metals generally forms an electrochemical cell which comprises an anode, cathode, and an electrolytic solution. In a two metal joining, one with more negative potential considered as active metal with reference to other. It has more free electrons to offer and suffered from anodic dissolution. On the other hand, the one with more noble potential cathodically protected from corrosion.

2.5.4 Corrosion behaviour of AZ91 alloy

The AZ91 alloy consists of two major phases, i.e., α-Mg (a substitutional solid solution of Al in Mg) and β-$Mg_{17}Al_{12}$ phase (an intermetallic compound precipitated at grain boundaries). Song et al. [136,137] studied the effect of Al in commercial Mg-Al alloy and found that 2.0Al (wt.%) addition resulted in a corrosion rate of 114 mm/y and it was reduced to 101 mm/y with 9.0Al (wt.%). The presence of Al in the matrix phase prevented the localised corrosion in great extent and reduced corrosion by the formation of a stable passive film on the alloy surface [138]. Significant improvement in corrosion resistance of Mg-alloys was observed by Lunder et al. [139] when Al concentration was higher than 8.0 (wt.%) in the α-Mg phase. They reported active anodic dissolution when Al content was below 8.0 (wt.%). Mathieu et al. [140] proposed that the semi-solid process would be a better way to reduce the corrosion rate in AZ91 alloy because it assists Al enrichment in α-Mg phase. Warner et al. [141] studied the rapidly solidified ribbons of Mg-9Al alloys and suggested that greater than 5.0Al (wt.%) was sufficient to bring down the corrosion rate. Hermann et al. [142] reported a progressively better corrosion resistance along with more noble corrosion potential values when Al concentration varies from 9.6 to 23.4 (wt.%) in the Mg-Al alloys fabricated by rapid solidification process. Precipitation of β-$Mg_{17}Al_{12}$ phase and its distribution in the microstructure have a great effect on corrosion behaviour of the alloy [143–145]. Some studies claimed that the β-$Mg_{17}Al_{12}$ phase acted as a barrier against corrosion and improved the corrosion resistance of the alloy [125,145,146]. It can play a role of the barrier and inhibits corrosion only when the distribution of β-$Mg_{17}Al_{12}$ phase is continuous with high mass fraction, and smaller grain size [137]. Conversely, enhanced corrosion rate was observed when the grain size was large, and the distance between β-$Mg_{17}Al_{12}$ phases were increased [136]. Mass fraction of β-$Mg_{17}Al_{12}$ phase in the microstructure is the deciding factor to switch the nature from corrosion inhibitor to corrosion promoter. High galvanic activity was reported when the volume fraction of β-$Mg_{17}Al_{12}$ phase was low and vice-versa [136,147]. Zhao et al. [148] studied the influence of β-$Mg_{17}Al_{12}$ phase morphology on the corrosion behaviour of the AZ91 alloy. The corrosion barrier effect was provided by the fine (α-Mg + β-$Mg_{17}Al_{12}$) lamellar micro-constituent owing to the presence of β-$Mg_{17}Al_{12}$ phase in plate form. On the other hand, nano-sized β-$Mg_{17}Al_{12}$ precipitates accelerated micro-galvanic corrosion and enhanced corrosion rate. Song et al. [136,145] reported the higher cathodic activity in β-$Mg_{17}Al_{12}$ phase with much lower anodic dissolution below pitting potential. At corrosion potential,

the i_{corr} value of β-$Mg_{17}Al_{12}$ phase was much lower than that of α-Mg phase, which ensured the stability of β-$Mg_{17}Al_{12}$ phase in NaCl solution. Ambat et al. [147] investigated the corrosion behaviour of die-cast and gravity-cast AZ91D alloy. Die-cast alloy showed better corrosion resistance due to fine grain structure and continuous distribution of β-$Mg_{17}Al_{12}$ phase. Also, in another study, they found very high corrosion rate of both the alloys in highly acidic media with the comparison to neutral and highly alkaline solutions. Corrosion rate further boosts up with an increase in chloride ion concentration in the solution at all pH levels [149]. Mathieu et al. [150] studied the corrosion behaviour of AZ91D alloys processed by HPDC and semi-solid processing (SSP). They found higher corrosion resistance of SSP fabricated AZ91D alloy than HPDC irrespective of corrosion testing methods. The corrosion resistance of α-Mg and β-$Mg_{17}Al_{12}$ phases in AZ91 alloy was studied by Mathieu et al. [140]. Higher Al content in α-Mg enhances the corrosion resistance by the formation of an Al enriched superficial layer. The β-$Mg_{17}Al_{12}$ phase was better corrosion resistant than the α-phase, and its chemical behaviour depended on pH of the solution. Song et al. [151] investigated corrosion behaviour of the die-cast AZ91D alloy aged at 433 K for a variable time duration (up to 585 h). They noted significant improvement in corrosion resistance in the early stages of ageing. This behaviour was attributed to effective blocking of corrosion propagation by the continuous β-$Mg_{17}Al_{12}$ phase network. The corrosion behavior of as-cast (F), homogenized (T4), and artificially-aged (T6) AZ91 alloy was investigated by Lunder et al. [152] in chloride media. The best corrosion resistance was exhibited by artificially-aged (T6) AZ91 alloy. Zhao et al. [153] studied the corrosion behaviour of as-cast and homogenization annealing (HA) heat treated (at 683 K for 10 h) AZ91 alloy and found almost similar corrosion resistance. The addition of Zn shifted the potential of α-Mg and β-$Mg_{17}Al_{12}$ phases towards more noble values. However, the susceptibility to filiform corrosion of AZ alloys also increased with the increase of Zn in the range of 0-3 (wt.%) [139].

2.5.5 Corrosion behaviour of modified AZ91 alloys

The studies on corrosion response of the AZ91 alloy following elemental additions are limited. Wu et al. [12] studied corrosion behaviour of the AZ91 with additions of RE and Ca. They reported that the additions of RE and Ca in the AZ91 alloy resulted in improved corrosion response by formation of reticular Al_2Ca phase that acted as an effective barrier against corrosion. Fan et al. [154] investigated the role of Ce on modification of

microstructure, mechanical and corrosion properties of the AZ91D alloy. They concluded that addition of Ce refined the β-$Mg_{17}Al_{12}$ phase and also formed a new Al_4Ce phase, which significantly improved mechanical behaviour of the AZ91D alloy. The refined and continuous β-$Mg_{17}Al_{12}$ phase acted as a corrosion barrier. Further, higher positive breakdown potential of the AZCe alloy indicated that the protective film on the surface of AZCe alloy was more effective than that on the surface of the AZ91D alloy. Corrosion behaviour of Ho added AZ91 alloy in 3.5 % NaCl was examined by Zhou et al. [155]. They reported that Ho addition enhanced corrosion resistance of the AZ9l alloy owing to easy oxidation and passivation of the Ho, Al, Mg and Mn elements present in the Ho consisting phase. Also, the addition of Ho diminished the concentration of Fe and fraction of the β-$Mg_{17}Al_{12}$ phase in the alloys as well as drastically weakened micro-galvanic corrosion tendency. The corrosion film generated on the surface of the Ho-containing alloys was relatively more protective, complete and compact than that on the surface of Mg-Al alloy with no Ho addition. Srinivasan et al. [156] studied the effect of small additions (individual and combined) of Sb and Si on electrochemical corrosion behaviour of the AZ91 alloy. They observed that addition of Sb to AZ91-Si alloy transformed the Mg_2Si phase into polygonal shape and distributed it more evenly at grain boundaries. Minor improvement in corrosion behaviour was observed when Si was added, whereas, the mixed content of Sb and Si improved corrosion behaviour notably. Fine and even distribution of polygonal shaped Mg_2Si intermetallic efficiently inhibited corrosion as compared to the coarse Mg_2Si phase. The individual addition of Sb reduced corrosion resistance due to the formation of Mg_3Sb_2 intermetallic, which increased cathodic activity and therefore, decreased corrosion resistance of the AZ91 alloy. Zhou et al. [157] studied the effect of Bi, Ca and Sb additions on corrosion behaviour of the AZ91 alloy. In their study, the addition of Bi or Sb refined the β-$Mg_{17}Al_{12}$ phase and led to the formation of the needle shaped Mg_3Bi_2 or Mg_3Sb_2 phases distributed primarily along grain boundaries. Severe corrosion was reported on the Mg_3Bi_2 and Mg_3Sb_2 particles. Mixed addition of Bi and Sb to the alloy considerably increased its corrosion. The addition of 0.14Ca (wt.%) to AZ91 formed new Mg_2Ca and $Mg_{17}Al_8Ca_{0.5}$ phases that did not improve its corrosion resistance although it was not detrimental at all. Candan et al. [158] studied corrosion performance of the AZ91 alloy with 0.2 to1.0 Pb (wt.%). The addition of 1.0Pb (wt.%) improved corrosion resistance by 98% due to suppression of intermetallic formation and increased Al content in α-Mg. Sudholz et al. [159] represented a survey of corrosion results of AZ91E alloy with different and typical alloying additions. They pointed out that the alloying addition beyond solubility limit was

detrimental to corrosion resistance. The performance was superior with alloying additions when the content was within the solubility limit. They concluded that Y, Ce, Ti, and Sc were beneficial to the corrosion resistance of the alloy. Arrabal et al. [160] investigated corrosion behaviour of the AZ91D-based alloys comprising up to 1.5Nd (wt.%) in 3.5NaCl (wt.%) at ambient temperature. The addition of Nd prevented micro-galvanic couples that were harmful to corrosion of AZ91D alloys. The addition of 0.7-0.8 Nd (wt.%) decreased corrosion rate of the same by about 90%, while, further increase of Nd content reduced corrosion rate. In a recent study, Arrabal et al. [161] evaluated corrosion performance of the AZ91 alloy with a various content of Nd as per PV1210 standard and concluded that the optimum content of Nd is 0.5 (wt.%). In another study of corrosion behaviour of Nd and Gd added AZ91D alloy Arrabal et al. [162] reported the formation of Al_2RE and Al-Mn-RE containing phases with reduced amount of β-$Mg_{17}Al_{12}$ phase. The additions of Gd and Nd in their study were not beneficial to corrosion of the AZ91D alloy. Effect of Y addition on the corrosion resistance of AZ91 alloy was investigated by Luo et al. [163]. They observed the best corrosion resistance with 0.3Y (wt.%) addition. Further increase in Y content resulted in higher corrosion rate.

2.6 Motivation for the present work

The aforementioned literature review evidenced that among the several Mg alloys, the AZ91 is still a workhorse alloy for automobile industries and its use is limited to interior parts that are mostly die-cast. The major growth areas for Mg alloys in automobile use are the powertrain applications where mechanical properties including creep resistance in the temperature range of 423-573 K is a major requirement. Although the AZ91 alloy offers an excellent combination of ambient temperature strength and ductility, good corrosion resistance and good die-castability, however, it does not exhibit the required elevated temperature performance. This alloy has drawbacks of a drastic reduction in tensile properties and creep resistance above 393 K owing to the softening of the β-$Mg_{17}Al_{12}$ phase present along grain boundaries, which made it inadequate for major powertrain applications. Several attempts were made to modify the microstructure of AZ91 alloy through alloying additions in order to improve its high temperature properties. The additions of the alloying elements mainly form a thermally stable intermetallic with Mg and Al at grain boundaries, and they provide an effective barrier for dislocation and grain boundary movement even at a higher temperature. The review of the alloying additions to AZ91 alloy concludes that the

individual additions of Ca and Sb are more effective in enhancing creep resistance owing to the presence of higher melting point Al_2Ca and Mg_3Sb_2 phases formed following the additions of Ca and Sb, respectively. Further, it was observed that some combined additions were more effective in enhancing ambient and elevated temperatures mechanical properties including creep behaviour. Therefore, combined additions of Ca and Sb to AZ91 alloy will bring plausible improvement in the above-mentioned properties as well, which is investigated in the present thesis. For comparison, the aforementioned properties are also evaluated on the AZ91 alloy with and without individual additions of Ca and Sb.

Chapter 3

Experimental procedure

This chapter presents the description of the materials used for the present investigation, their detailed processing and characterization techniques used for them.

3.1 Fabrication of alloy

The present investigation comprised of six alloys containing AZ91 Mg alloy and its modified alloys with the individual as well as combined additions of Ca and Sb. Commercial AZ91 Mg alloy ingots and pure Ca (purity 99.9%), and Sb (purity 99.9%) granules were used to produce the AZ91-Ca-Sb-based alloys. The various combinations of Ca and Sb added in the AZ91 alloy, the achieved composition with detailed chemical compositions of the alloys along with their corresponding abbreviated nomenclatures are shown in Table 3.1 and 3.2. The melting was carried out in an electrical resistance furnace using graphite crucible having a capacity of 1.0 kg. All the alloys were fabricated using the direct squeeze-casting process. The actual photograph of the squeeze-cast set up employed in the present investigation is shown in Fig. 3.1. The detailed steps followed for the fabrication of the alloys are summarized in the flow chart shown in Fig. 3.2. In this process, the calculated amount of AZ91 alloy ingots were added in the crucible, and it was then kept inside the furnace at 993 K for 80 min for complete melting. Predetermined quantities of Ca and Sb were incorporated to the melt at the same temperature, and the melt was continuously stirred for another 10 min in order to ensure the uniform distribution of the alloying elements. Stirring of the melt was stopped for about 5 min before pouring to settle down the oxide particles and other inclusions at the bottom of the crucible. The melt was then poured at 993 K manually into a steel mould (dimension: 75 mm diameter and 90 mm height) preheated to 523 K. The infiltration process took about 15 s. A direct squeeze-casting pressure of 120 MPa was applied on the melt till the end of solidification using a vertical hydraulic press of capacity 80 Ton. The solidification took approximately 60 s. During melting and after skimming, solid flux provided by FOSECO Industries Limited were used to protect the melt

from oxidation. A mixture of SF_6 (0.5 vol.%) and Ar (99.5 vol.%) was purged to protect the melt during pouring. The casting of 75-80 mm length and 75 mm diameter was produced.

Table 3.1: Target composition, achieved composition and designation of the alloys.

Target composition	**Achieved composition**	**Alloy designation**
AZ91-0.6Sb	AZ91-0.59Sb	AZY911
AZ91-1.0Ca	AZ91-0.89Ca	AZX911
AZ91-1.0Ca–0.3Sb	AZ91-0.91Ca-0.31Sb	AZXY9110
AZ91-1.0Ca–0.6Sb	AZ91-0.89Ca-0.62Sb	AZXY9111
AZ91-2.0Ca–0.3Sb	AZ91-1.80Ca-0.33Sb	AZXY9120

Table 3.2: Detailed chemical composition of the alloys.

Target composition	**Detailed achieved composition (wt.%)**								
	Al	**Zn**	**Mn**	**Ca**	**Sb**	**Fe**	**Ni**	**Cu**	**Mg**
AZ91	9.41	0.98	0.39	-	-	0.0013	0.0008	0.0091	Bal.
AZ91-0.6Sb	8.89	0.77	0.28	-	0.59	0.0019	0.0007	0.0080	Bal.
AZ91-1.0Ca	8.55	0.56	0.35	8.89	-	0.0016	0.0011	0.0085	Bal.
AZ91-1.0Ca–0.3Sb	8.66	0.49	0.29	0.91	0.31	0.0018	0.0008	0.0097	Bal.
AZ91-1.0Ca–0.6Sb	8.47	0.78	0.34	0.89	0.62	0.0017	0.0009	0.0092	Bal.
AZ91-2.0Ca–0.3Sb	8.72	0.69	0.36	1.80	0.33	0.0021	0.0009	0.0089	Bal.

Fig. 3.1. Actual photograph of the electrical resistance pit furnace, squeeze-casting setup and other accessories employed for carrying out the casting operation.

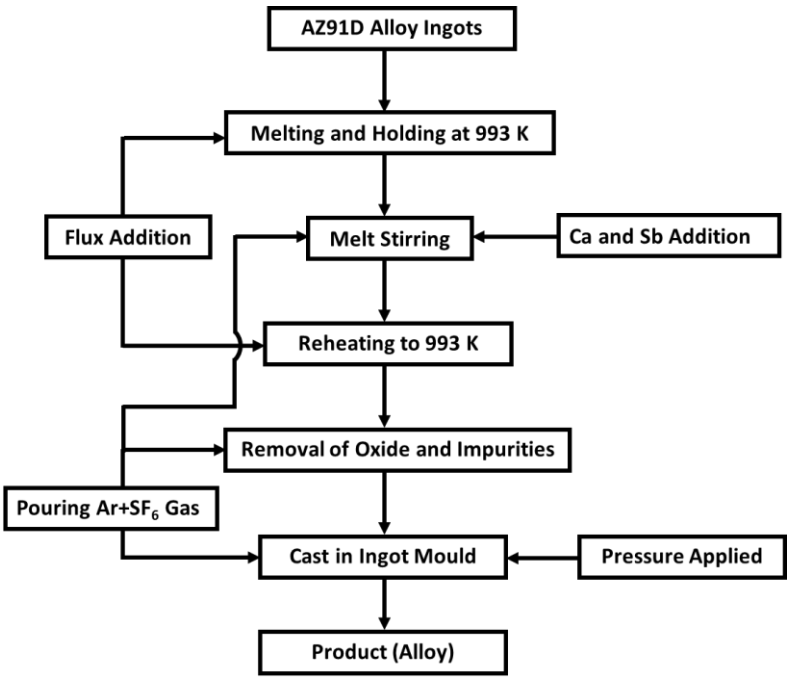

Fig. 3.2. Flow chart showing the detailed steps followed for the fabrication of the alloys.

3.2 Specimen preparation

The standard metallographic technique was employed in order to prepare the specimens for microstructural analysis. For etching, a solution of 100 ml ethanol, 20 ml of distilled water, 10 ml acetic acid and 6 gm picric acid was used. The specimens for tensile tests were prepared in accordance with ASTM E8M-03 standard. For both impression creep and corrosion testing, cylindrical specimens with a diameter of 25 mm and thickness of 6 mm were machined from the castings by using wire electrical discharge machining (EDM). For conventional creep testing, specimens of the dimension of 6 mm diameter and 15 mm length were machined from the alloys by wire EDM. For corrosion tests, surfaces of the as-cast AZ91 alloy and its modified alloys were slightly grinded with silicon carbide papers of various grades (up to 3000 grit) and deionized water was used as a coolant. The specimens were then cleaned ultrasonically and dried in air prior to tests. For analysis of the corrosion films formed on the specimen surfaces by FTIR spectroscopy, 1 mg of corrosion products was blended with a spectroscopic grade potassium bromide (KBr) powder to obtain 200 mg of a mixture. The mixture was then grinded in a mortar and pressed to pellets in a die. Pure KBr pellet of the same weight and size was used to obtain the background spectrum.

3.3 Characterizations of the alloys

3.3.1 X-Ray diffraction (XRD)

The phases present in the squeeze-cast alloys as well as corroded specimens were identified by an X-ray diffractometer (XRD) (Model: PANalytical X'Pert HighScore) employing CuKα (λ=1.541 A°) radiation. A scan rate of 2 º/min in the scan range of 10-90 º with a step size of 0.03 was employed.

3.3.2 Optical microscopy (OM)

Microstructures of all the squeeze-cast alloy specimens were examined by using an optical microscopy (Model: ZEISS Axiovision I10). The grain size measurement of all the alloys was carried out by mean linear intercept method according to the ASTM E1382-97(2010) standard.

3.3.3 Electron probe microanalysis (EPMA)

Microstructures of all the squeeze-cast alloy specimens were examined by using an electron probe microanalysis (EPMA) (Model: JEOL JXA 8530F). Microanalysis of the elements present in the specimens was also carried out by the same EPMA. Elemental mapping was recorded from the specimens after removing corrosion product in order to identify the phases that were unaffected due to corrosion.

3.3.4 Scanning electron microscopy (SEM)

The fracture surfaces of the broken tensile specimens were examined under a field emission scanning electron microscopy (FESEM) (Model: FEI Nova NanoSEM 450) equipped with an energy dispersive X-ray spectroscopy (EDS). Microstructures of all the creep tested as well as the corroded specimens were examined by using a scanning electron microscopy (SEM) (Model: FEI Quanta 200) furnished with energy dispersive X-ray spectroscopy (EDS) (Model: Oxford Instruments). The punched area on the impression creep tested specimen was bisected vertically along diameter in order to observe deformed zone beneath the indenter for possible microstructural changes.

3.3.5 Fourier transform infrared spectroscopy (FTIR)

Corrosion films formed on the specimen surfaces were examined by FTIR spectroscopy (Model: Shimadzu IR Prestige-21). FTIR spectra were recorded at ambient temperature in the mid-IR region of 4000-400 cm^{-1}.

3.3.6 Mechanical characterization

3.3.6.1 Tensile tests

Tensile tests of all the specimens were carried out in accordance with ASTM E8M-03 standard using a universal testing machine (Model: INSTRON 5967). The specimens were tested at ambient, 423 K and 473 K temperatures. A minimum of three specimens was tested at each temperature, and the average value is reported here as tensile properties.

3.3.6.2 Impression creep test

The impression creep testing setup employed here was provided by Spranktronics Bangalore, India. It is a lever based setup (ratio 1:10), and the lever is connected to a pull rod. One cage holding the specimen is attached to the pull rod and another cage holding the indenter is fastened to a fixed base plate. Both cages were kept inside an electrically heated tubular furnace. A load cell having the maximum capacity of 980 N is attached to the load train, and it measures the load with an accuracy of ±0.1% of full scale. In this system, a cylindrical shaped indenter made of tungsten carbide was impressed on the specimen, and the depth of penetration (h) was recorded as a function of time (t) using a PC-based online data acquisition system. The temperature was regulated with an accuracy of ±1 °C and the precision on depth measurement was ±0.001 mm. Prior to the tests, at least 60 min was allowed for attaining complete thermal equilibrium of the whole assembly of the specimen chamber. All the specimens were slightly grinded with various grades of emery papers before carrying out the tests. The specimens were then cleaned thoroughly by ultrasonic cleaner and dried using hot air blow. The impression creep tests were conducted in the stress range of 300 to 480 MPa and temperature range of 423 to 523 K for a dwell time of 7200 s.

3.3.6.3 Compressive creep test

Compressive creep tests were carried out on all the alloys using a lever arm (10:1) creep testing machine (Model: ATS 2330) at a temperature 473 K and stress of 70 MPa. All the tests were continued till the minimum creep rate was attained.

3.3.7 Corrosion test

The electrochemical corrosion tests were performed in 0.5NaCl (wt.%) solution at neutral pH with specimen exposed area of 0.5 cm^2 with the help of a computer controlled GillAC potentiostat/galvanostat at ambient temperature (25±1.0 °C). In the present study, the concentration of NaCl solution used for performing the corrosion experiments had been decided as per the available literature [164–166]. A three electrode corrosion cell (250 ml) was used, and it consisted of a Pt counter electrode, an Ag/AgCl (3 mol/l KCl) reference and specimen as the working electrode. Each experiment consisted of three sequential tests, and details of these tests are mentioned below. All the tests were conducted on the specimens without any intermediate surface treatment. Before the tests, all the specimens were allowed to stay in the solution for 30 minutes in open circuit condition to ascertain the

stability of the potential. This potential referred as open circuit potential (OCP). Electrochemical impedance spectroscopy (EIS) was performed at OCP in the frequency range of 100 kHz-0.01 Hz using the sinusoidal signal of amplitude ±5 mV. The first EIS scan was corresponding to 0 h and the measurement was repeated after every 2 h. An EIS spectrum analyser software was employed to analyse and simulate the impedance behaviour of the fabricated alloys and accordingly, the electrical equivalent circuit was proposed. Potentiodynamic polarization scan was performed from -200 mV vs. Ag/AgCl/Sat. KCl relative to OCP following a scan rate of 12 mV/min. Tests were ended as the corrosion current density exceed 1 mA/cm^2 in order to reduce damage due to corrosion on the specimen surfaces before the start of next sequence. Different parameters of potentiodynamic polarization study were evaluated from the polarization curves using Tafel extrapolation method.

The specimens were thoroughly cleaned in deionized water after corrosion tests and dried in air. All the specimens before and after removal of corrosion film were observed under a microscope. Corrosion film was removed as per ASTM G1-03 standard employing a solution of distilled water pertaining 200 g chromic acid, 20 g barium nitrate, and 10 g silver nitrate. The specimen was stirred for 1 min in the solution kept in a beaker. The specimen was then thoroughly rinsed in ethanol, cleaned in deionized water and dried in air.

Chapter 4

Microstructural characterization

This chapter deals with the detailed microstructural characterization of all the squeeze-cast AZ91-based alloys. The changes in the microstructure following the individual and combined additions of Sb and Ca to the AZ91 alloy are investigated employing XRD, optical microscopy and EPMA. The phases present in all the squeeze-cast alloys are identified by XRD. Microstructures are examined by using an optical microscopy and an EPMA. Microanalysis of the elements present in the specimens was carried out by the EPMA.

4.1 Phase analysis by XRD

The solubility of Ca and Sb in Mg at ambient temperature is limited, and accordingly, the addition of these elements to Mg easily results in the formation of Ca and Sb containing intermetallics in Mg alloys. The XRD patterns obtained from all the alloys are shown in Fig. 4.1. It is evident from the figure that all the alloys consist of primary Mg (α-Mg) peaks along with the peaks corresponding to β-$Mg_{17}Al_{12}$ phase. Besides α-Mg and β-$Mg_{17}Al_{12}$, Mg_3Sb_2 in the AZY911 alloy; Al_2Ca in the AZX911 alloy; and both Al_2Ca as well as Ca_2Sb (M. P. 1100 K) in the AZXY9110, AZXY9111, AZXY9120 alloys are the main phases present in the as-cast condition. The intensity of the peak corresponding to β-$Mg_{17}Al_{12}$ phase present in the AZXY9120 is relatively weaker, which indicates the amount of β-$Mg_{17}Al_{12}$ phase formation is lower in this alloy containing the highest amount of Ca. The suppression of β-$Mg_{17}Al_{12}$ phase formation in Mg-Al alloys with addition of Ca was observed by other researchers as well [12,17]. Wu et al. [12] observed the complete suppression of β-$Mg_{17}Al_{12}$ phase formation with the addition of 4.0Ca (wt.%) in the Mg-Al alloy. The alloys employed in the present investigation contain a maximum of 2.0Ca (wt.%), and it is not enough to suppress fully the formation of low melting point β-$Mg_{17}Al_{12}$ phase (M. P. 710 K). There was no evidence of formation of Mg_2Ca, Al_4Ca and $(Mg,Al)_2Ca$ phases in the alloys.

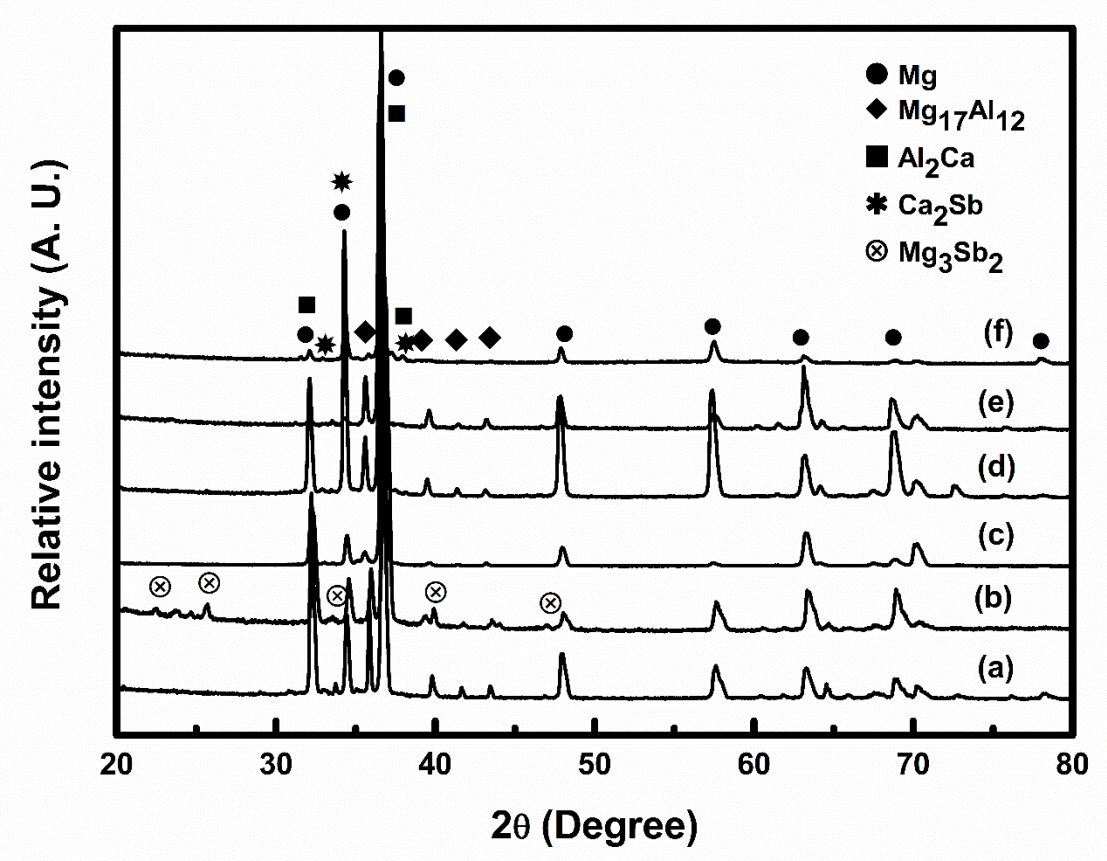

Fig. 4.1. XRD patterns obtained from the squeeze-cast (a) AZ91, (b) AZY911, (c) AZX911, (d) AZXY9110, (e) AZXY9111 and (f) AZXY9120 alloys.

4.2 Microstructural observation by optical microscopy

Fig. 4.2(a-f) displays optical micrographs of all the squeeze-cast AZ91-based alloys. The differences among the various micrographs are clearly visible. All the alloys exhibit dendritic microstructures with some second phases distributed in the interdendritic regions. The morphologies of the dendritic microstructures remain almost same in all the alloys, although it is slightly different in the AZXY9120 alloy. Evidently, the additions of Ca and/or Sb resulted in significant refinement of the dendrite cell size and β-$Mg_{17}Al_{12}$ phase in the microstructures. The microstructural refinement is more pronounce in the alloys containing combined additions (i.e., AZXY9110 and AZXY9111) compared to the alloys containing individual additions (i.e., AZX911 and AZY911) except for the AZXY9120 alloy. The dendritic cell size in the AZXY9120 alloy containing 2.0Ca and 0.3Sb (wt.%) was relatively coarse and morphology was slightly different as a result of the formation of higher volume fraction of lamellar eutectic of α-Mg and Al_2Ca phase (shown in EPMA micrograph later on) along the grain boundaries that was not observed in the alloys containing less than 2.0Ca (wt.%) employed. The difference in refinement in the microstructures following individual additions of Ca and Sb was not very distinct. The same was true for combined additions of Ca and Sb in the AZXY9110 and AZXY9111 alloys.

4.3 Microstructural observation by EPMA

Fig. 4.3(a-f) shows the EPMA micrographs of all the squeeze-cast alloys. The micrograph of AZ91 alloy (Fig. 4.3(a)) comprises of primary Mg (α-Mg) matrix surrounded by the lamellar eutectic consisting of alternate layers of α-Mg and β-$Mg_{17}Al_{12}$ as well as massive β-$Mg_{17}Al_{12}$ phase. Further, discontinuous precipitation of β-$Mg_{17}Al_{12}$ phase at few places in the micrograph can be observed. EDS analysis was taken from the grain interior of the micrograph shown in Fig. 4.3(b) exhibited an average composition of Mg-2.1Al (at.%), which corresponds to primary Mg (α-Mg). The presence of α-Mg was confirmed in other alloys as well. The EDS analysis from the dull bulky phase of the AZX911 alloy shown in Fig. 4.3(c) revealed an average composition of Mg-40.5Al-3.0Ca (at.%), which confirms the presence of β-$Mg_{17}Al_{12}$ phase. Nevertheless, 3.0Ca (at.%) is present in the β-$Mg_{17}Al_{12}$ phase. Suzuki et al. [167] and Li et al. [14] too reported about 4.0 (at.%) and little solubility of Ca in β-$Mg_{17}Al_{12}$ phase, respectively. The presence of Ca in β-$Mg_{17}Al_{12}$ phase was reported to increase its thermal stability [104,168].

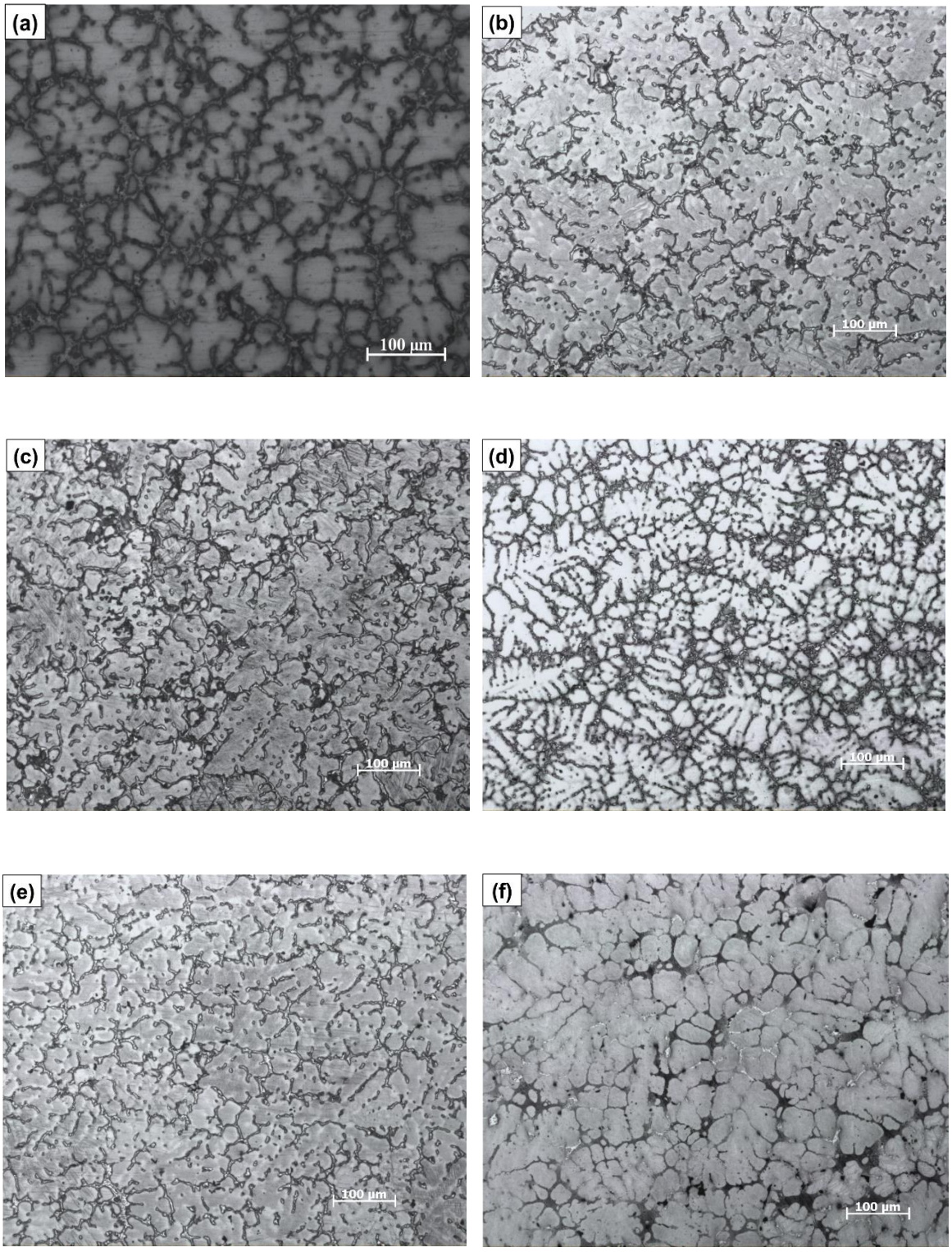

Fig. 4.2. Optical micrographs of the squeeze-cast (a) AZ91, (b) AZY911, (c) AZX911, (d) AZXY9110, (e) AZXY9111, and (f) AZXY9120 alloys.

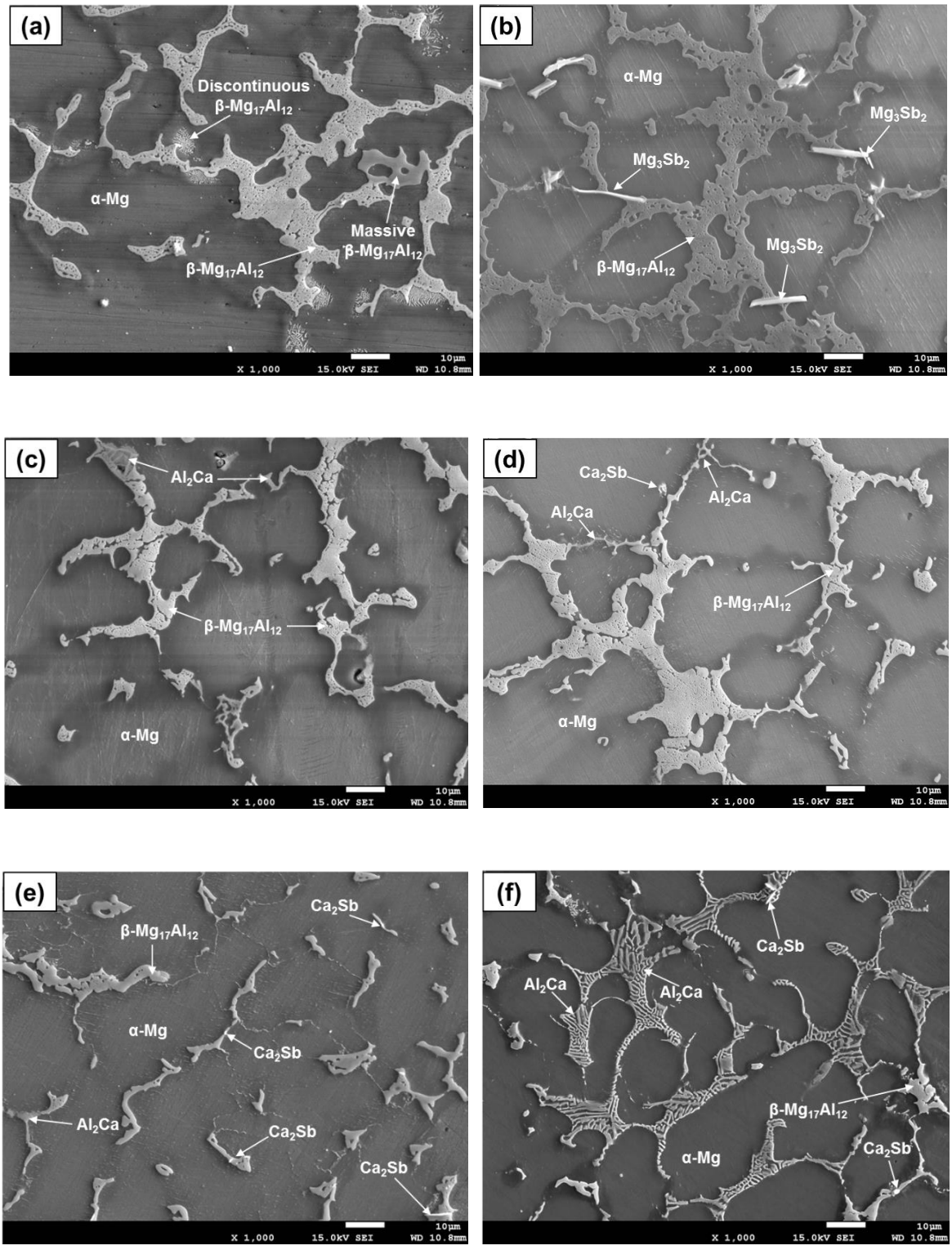

Fig. 4.3. EPMA micrographs of the squeeze-cast (a) AZ91, (b) AZY911, (c) AZX911, (d) AZXY9110, (e) AZXY9111, and (f) AZXY9120 alloys.

A similar observation, i.e., the β-$Mg_{17}Al_{12}$ phase having a little solubility of Ca was also drawn for the rest alloys (i.e., AZXY9110, AZXY9111, and AZXY9120) containing Ca. Representative EDS spectrums along with the regions of exact EDS analysis for the alloys are included in Fig. 4.4. The obvious change in the microstructures of all the modified squeeze-cast AZ91-based alloys was the reduced dimension of eutectic formed along the grain boundaries, i.e., refinement of β-$Mg_{17}Al_{12}$ phase and reduction of grain size. It means both Ca and Sb assisted refining the eutectic phase at the grain boundaries. A similar observation, i.e., refinement of the precipitates as well as the entire microstructure following additions of rare earth Ce additions has also been reported by Chen et al. [169]. The observed refinement of β-$Mg_{17}Al_{12}$ phase was more pronounced in the alloys containing combined additions of Ca and Sb. With the increase of Ca content, a new reticular Al-Ca-rich lamellar eutectic phase was evolved along with β-$Mg_{17}Al_{12}$ phase at grain boundaries of the AZXY9110, AZXY9111 and AZXY9120 alloys containing combined additions of Ca and Sb (Fig. 4.3(d-f)). Furthermore, with increasing Ca addition, the volume fraction of α-Mg is increased. Among the alloys the one containing 2.0Ca (wt.%), i.e., AZXY9120 exhibited higher volume fraction of Al-Ca-rich phase. Accordingly, the amount of β-$Mg_{17}Al_{12}$ phase reduced in it and an Al-Ca-rich network of white lamellae at the grain boundaries and triple points formed throughout the microstructure. EDS analysis was taken from the Al-Ca-rich phase in the micrograph shown in Fig. 4.3(f) exhibited an average composition of Mg-63.1Al-26.8Ca (at.%). Thus, the atomic concentration ratio of Al to Ca is 2.35, which is close to 2.0 corresponding to that of Al_2Ca. The present EDS result matches pretty well with the EDS result, i.e., Mg-66Al-27Ca (at.%) taken by Suzuki et al. [170] from the grain boundary phase using TEM in the Mg-5Al-3Ca (wt.%) alloy. The type of intermetallic compound formed following the addition of Ca to Mg-Al alloys depend on the Ca/Al mass ratio. The presence of both Mg_2Ca and Al_2Ca was detected with a mass ratio of more than ~0.8, however, below this value the Al_2Ca phase alone was observed [168,171]. In all the Ca containing alloys employed, the mass ratio of Ca/Al is 0.11 (for AZXY9110, AZXY9111, and AZX911) and 0.22 (for AZXY9120) and accordingly, Al_2Ca phase alone is expected. Wu et al. [12] observed that Al_2Ca phase appeared when more than 1.0Ca (wt.%) was added to the Mg-9Al-0.5Zn (wt.%) alloy. With increasing Ca addition, they observed the amount of Al_2Ca phase increased, and the amount of β-$Mg_{17}Al_{12}$ phase decreased; β-$Mg_{17}Al_{12}$ phase disappeared altogether at 4.0Ca (wt.%) addition, which is good for creep resistance. The presence of Al_2Ca phase in Ca containing AZ-based alloys has also been reported in several other literatures [12,13,172–174].

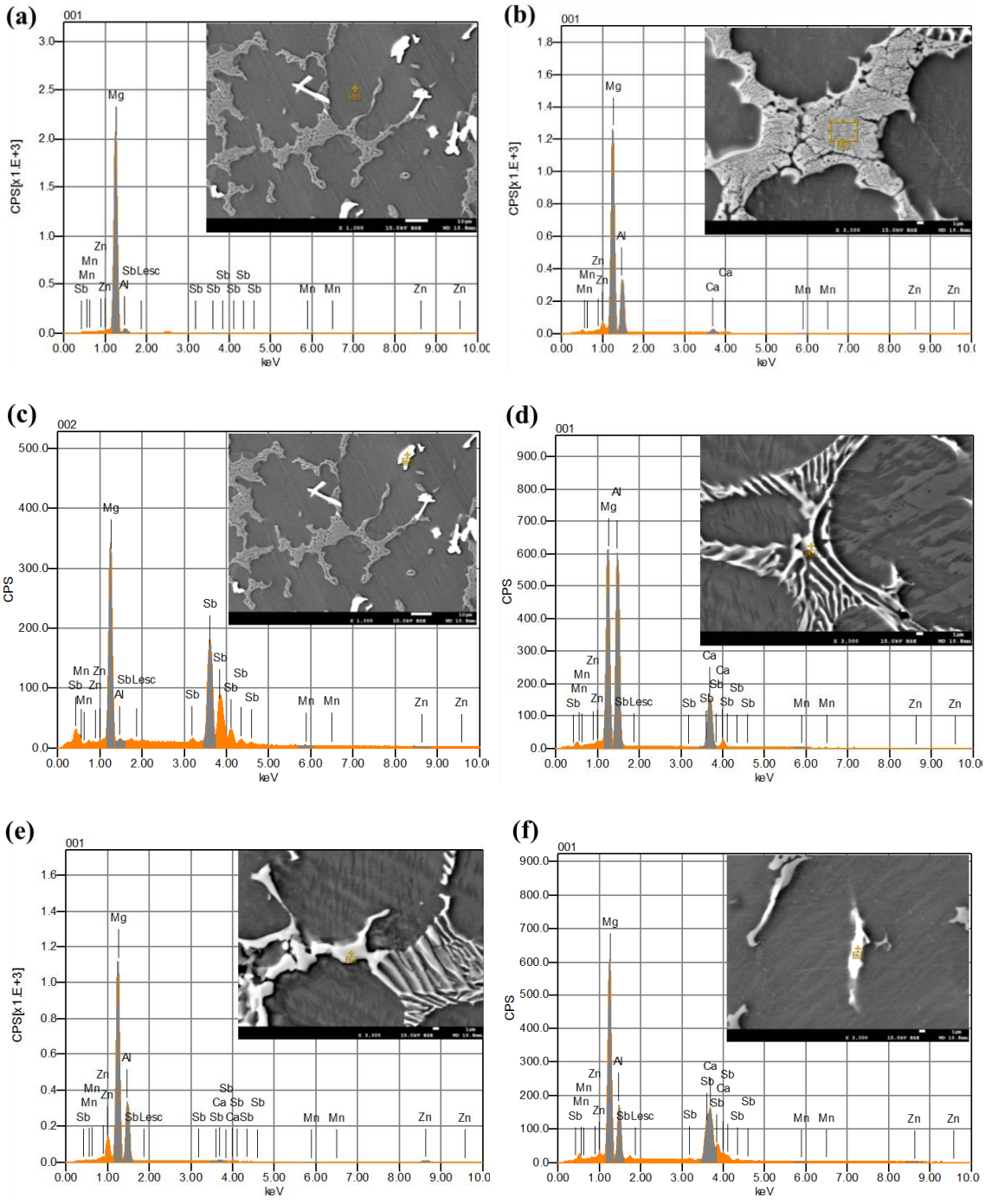

Fig. 4.4. Representative EDS spectrums along with the regions of exact EDS analyses corresponding to the (a) α-Mg phase in the AZY911 alloy; (b) β-$Mg_{17}Al_{12}$ phase in the AZX911 alloy; (c) Mg_3Sb_2 phase in the AZY911 alloy; (d) Al_2Ca and (e) β-$Mg_{17}Al_{12}$ phases in the AZXY9120 alloy; and (f) Ca_2Sb phase in the AZXY9111 alloy.

There was no evidence of formation of discontinuous β-$Mg_{17}Al_{12}$ phase in the newly developed squeeze-cast alloys, unlike AZ91 alloy. Sb addition resulted in the formation of rod-shaped precipitates distributed at grain boundaries and grain interior (Fig. 4.3(b)) in the AZY911 alloy containing 1.0Sb (wt.%) alone. EDS analysis taken from these precipitates exhibited an average composition of Mg-29.3Sb-0.8Al (at.%), and the precipitates were identified as a Mg_3Sb_2 phase. Guangyin et al. [105] too confirmed the formation of Mg_3Sb_2 phase in an AZ91 alloy containing (0-0.7) Sb (wt.%) using TEM. In all the three alloys containing combined additions, the morphology of the Sb-rich phase changed fully and altogether a new irregular-shaped Ca-Sb-rich precipitates formed. Based on microanalysis carried out by EDS along with XRD data, the precipitates were identified as a Ca_2Sb phase. The Ca_2Sb phase is having a tetragonal crystal structure and brittle in nature [175]. It was observed that the amount of Ca_2Sb phase was the maximum in the AZXY9111 alloy containing 1.0Ca and 0.6Sb (wt.%). The amount of Ca_2Sb phase was relatively less in the AZXY9110 and AZXY9120 alloys due to the smaller content of Sb, i.e., 0.3 (wt.%). The values of electronegativity of Mg, Al, Zn, Mn, Ca and Sb are 1.31, 1.61, 1.65, 1.55, 1.00 and 2.05, respectively [15,76]. It is obvious that the largest difference in electronegativity exists between Ca and Sb. The higher electronegativity difference between Ca and Sb would preferably favour the formation of Ca-Sb-containing intermetallic, and accordingly, a new Ca_2Sb phase formed suppressing Mg_3Sb_2 phase in the alloys containing combined additions.

4.4 Elemental mapping by EPMA

In order to further clarify the distribution of Ca and Sb in the squeeze-cast AZ91-Ca-Sb alloys, the elemental mapping is carried out using EPMA. Fig. 4.5 shows the mapping of the major elements present in the AZXY9110 alloy, as a representative EPMA elemental mapping for the alloys containing combined additions, corresponding to the SE and its BSE images are shown in Fig. 4.5. It is clear from the elemental mapping that the grain boundary phases are mainly enriched in Mg, Al, Ca and Zn. About (3.0-5.0)Ca (wt.%) was dissolved in β-$Mg_{17}Al_{12}$ phase. The solubility of Ca in the primary Mg was less than 0.5 (wt.%), which is negligible. Zn was dissolved in β-$Mg_{17}Al_{12}$ phase by about 3.5 (wt.%), which was reported by other researchers as well [176]. The solubility of Zn in Mg is only about 0.5 (wt.%). Therefore, it is expected that the additional amount of Zn is dissolved in β-$Mg_{17}Al_{12}$ phase. The grain boundaries were containing Al-Ca-rich and Mg-Al-rich phases. Few irregular shaped Ca-Sb-rich phase were also observed.

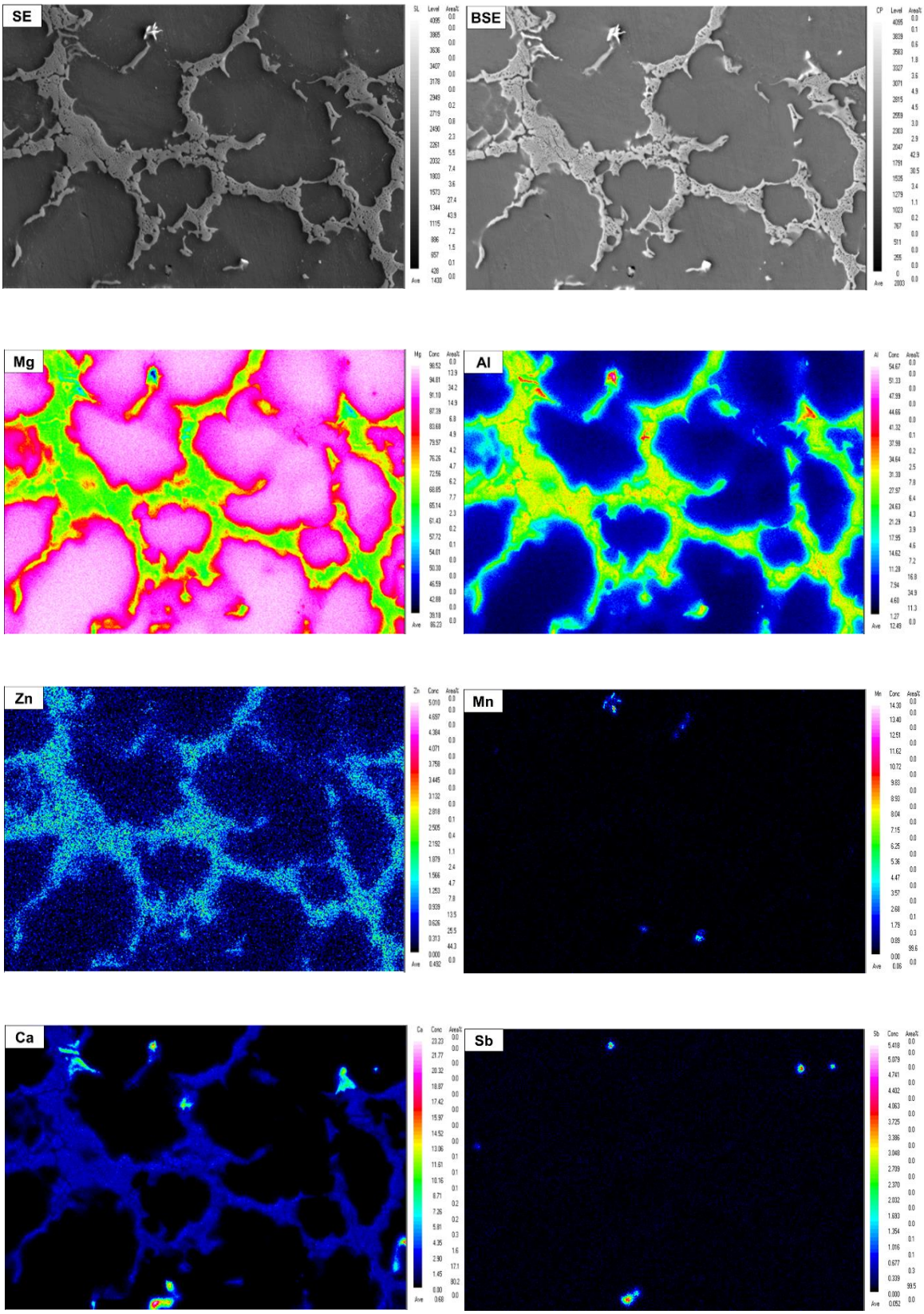

Fig. 4.5. EPMA elemental mapping of the different elements present in the squeeze-cast AZXY9110 alloy.

4.5 Summary of chapter 4

In this chapter, the detailed microstructural characterization of all the squeeze-cast AZ91-based alloys have been examined. The outcomes arising out from the investigation are as follows:

i. Both individual and combined additions of Ca and Sb refined the grain size and β-$Mg_{17}Al_{12}$ phase, which was more pronounced with combined additions.

ii. The difference in the refinement in the microstructures following individual additions was not very distinct. The same was true for combined additions in the AZXY9110 and AZXY9111 alloys. The dendritic cell size in the AZXY9120 alloy was relatively coarse, and morphology was slightly different as a result of the formation of the higher volume fraction of a lamellar eutectic of α-Mg and Al_2Ca phase.

iii. All the alloys consist of α-Mg and β-$Mg_{17}Al_{12}$ phases. Besides, α-Mg and β-$Mg_{17}Al_{12}$ phases, rod-shaped Mg_3Sb_2 phase in the AZY911 alloy; a new reticular shaped Al_2Ca phase in the AZX911 alloy; and both Al_2Ca as well as irregular shaped Ca_2Sb in the AZXY9110, AZXY9111, and AZXY9120 alloys were the main phases present in as-cast condition. The combined additions formed an additional Ca_2Sb phase suppressing Mg_3Sb_2 phase.

iv. The amount of β-$Mg_{17}Al_{12}$ phase formation was the lowest in the AZXY9120 alloy containing the highest amount of Ca.

v. The elemental mapping taken from the AZXY9110 alloy confirmed that the grain boundary phases were mainly enriched in Mg, Al, Ca and Zn.

Chapter 5

Tensile behaviour

In this chapter, the ambient and elevated temperature tensile properties of all the modified AZ91 alloys are investigated. Detailed analysis of the fracture surfaces of the tested specimens are also carried out. Finally, a correlation is made between the tensile behaviour of the alloys and their respective as-cast microstructures.

5.1 Tensile properties

Fig. 5.1(a-c) shows the typical stress-strain curves obtained from all the alloys tested at ambient, 423 K and 473 K temperature. All the curves exhibit an initial elastic region followed by plastic region. No clear yield point was observed in the stress-strain plots of all the alloys, which is the characteristics of the non-ferrous alloy. The shapes of the stress-strain curves changed with the increase in temperature from ambient to 473 K and related to some softening processes.

Fig. 5.2(a) shows the tensile properties of all the investigated squeeze-cast alloys tested at ambient temperature. It is observed that the additions of Ca and/or Sb to AZ91 alloy have a significant influence on the tensile properties. The ductility (%Elongation) and UTS of all the alloys decreased drastically with a corresponding increase in YS (0.2% proof stress) as compared to that of the base AZ91 alloy. The decrease in ductility and UTS, and the increase in YS were influenced more by the Ca than Sb addition. The ductility of the alloys (except AZXY9110) containing combined additions is almost equal to that of the alloys containing individual additions. However, the AZXY9110 alloy containing 1.0Ca and 0.3Sb (wt.%) exhibited the highest ductility at this temperature among the modified AZ91-based alloys employed. Further, increase in Sb content from 0.3 to 0.6 (wt.%) in combined additions decreased ductility of the alloys. The present observation is consistent with the reported results that the AZ91 alloy exhibits the best combination of tensile properties with a maximum Sb content of 0.5 (wt.%) [73]. A similar trend, i.e., decrease in ductility and UTS with an increase in YS for all the alloys containing individual and combined additions was

also observed at 423 K as shown in Fig. 5.2(b). Likewise, the alloys tested at 473 K exhibited an increase in YS, and its trend was similar to that observed at lower temperatures. On the other hand, ductility and UTS increased significantly at this temperature as shown in Fig. 5.2(c). Obviously, ductility gradually increases with a corresponding decrease in YS and UTS for all the alloys with increase in temperature from ambient to elevated temperatures up to 473 K. However, the increase in ductility at 423 K was marginal and became significant at 473 K. The best tensile properties at all the temperatures employed was obtained in the AZXY9110 alloy containing 1.0Ca and 0.3Sb (wt.%). It exhibited 6.2, 6.7 and 14.2% ductility with corresponding 152, 122 and 108 MPa YS at ambient, 423 K and 473 K, respectively.

The improved YS could be triggered by the reduction in grain size observed in all the modified alloys. The increase in YS is explained by Hall-Petch relation where the YS of a given material is inversely proportional to the square root of the average grain size as follows

$$\sigma_{0.2} = \sigma_0 + kd^{-\frac{1}{2}} \qquad 5.1$$

where $\sigma_{0.2}$ is the YS, σ_0 is the friction stress (intercept stress), k is the locking parameter (the Hall-Petch slope), and d is the grain diameter [18]. The observed tensile behaviour of the AZ91 alloy modified by Ca and/or Sb additions could be connected with the presence of Al_2Ca, Mg_3Sb_2 and Ca_2Sb phases that suppress the formation of the β-$Mg_{17}Al_{12}$ phase at grain boundaries. Thus, the aggregations of Ca and/or Sb at the grain boundaries inhibited α-Mg grain growth resulting grain refinement of the alloys and accordingly, YS is improved. Further, the YS values were estimated using the Hall-Petch relation in equation 5.1, and the results are shown in Table 5.1. For conventional as-cast AZ91 Mg alloy, K=167.2 mPa√μm and σ_0 = 74.2 MPa [177]. It is obvious that the experimentally measured YS values of the alloys are higher than the calculated values. There are several possible explanations for this variation. First, the values of K and σ_0 corresponding to squeeze AZ91 alloy is not available. Second, possible dispersion strengthening of the intermetallic phases also played an important role in increasing YS. Thirdly, the squeeze-cast alloys are having reduced gas and shrinkage porosities, which contributed positively to improved YS of the alloys.

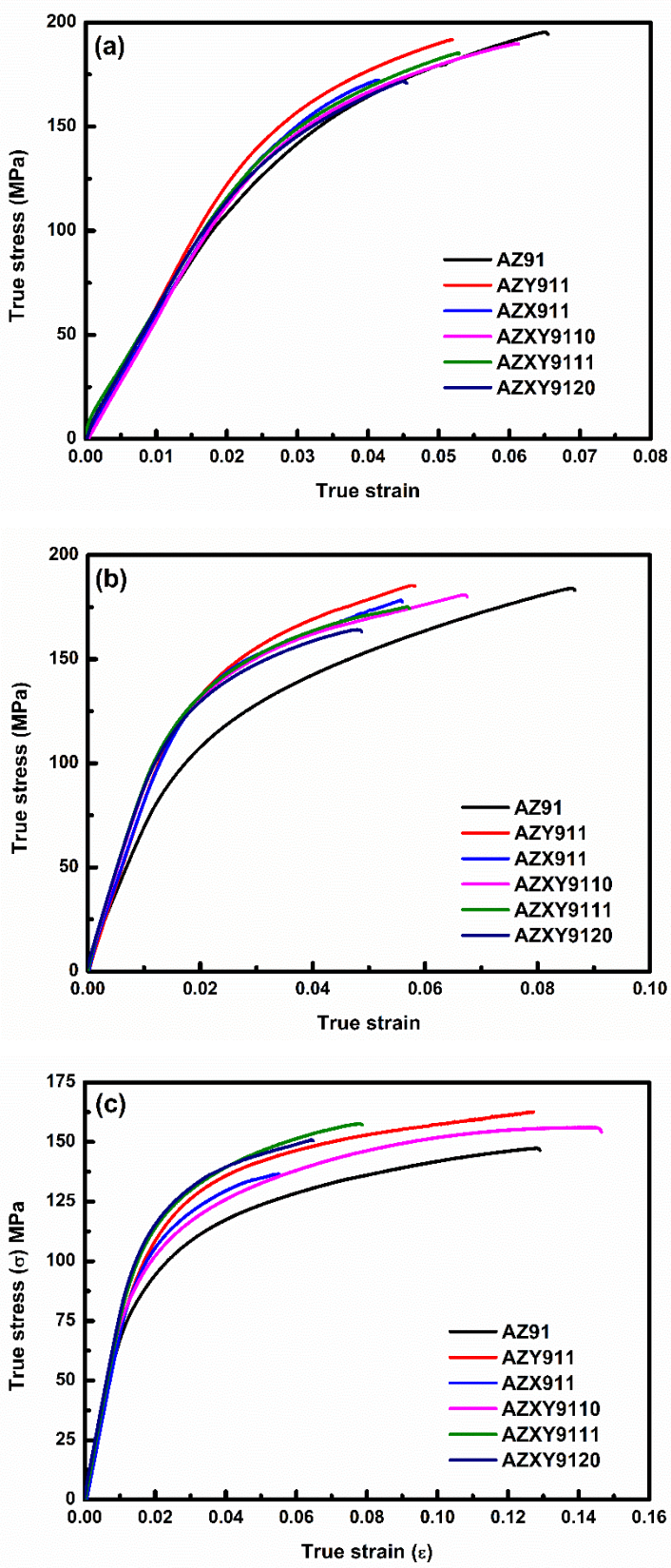

Fig. 5.1. True stress- true strain curves of all the fabricated alloys at (a) room temperature (b) 423 K and (c) 473 K.

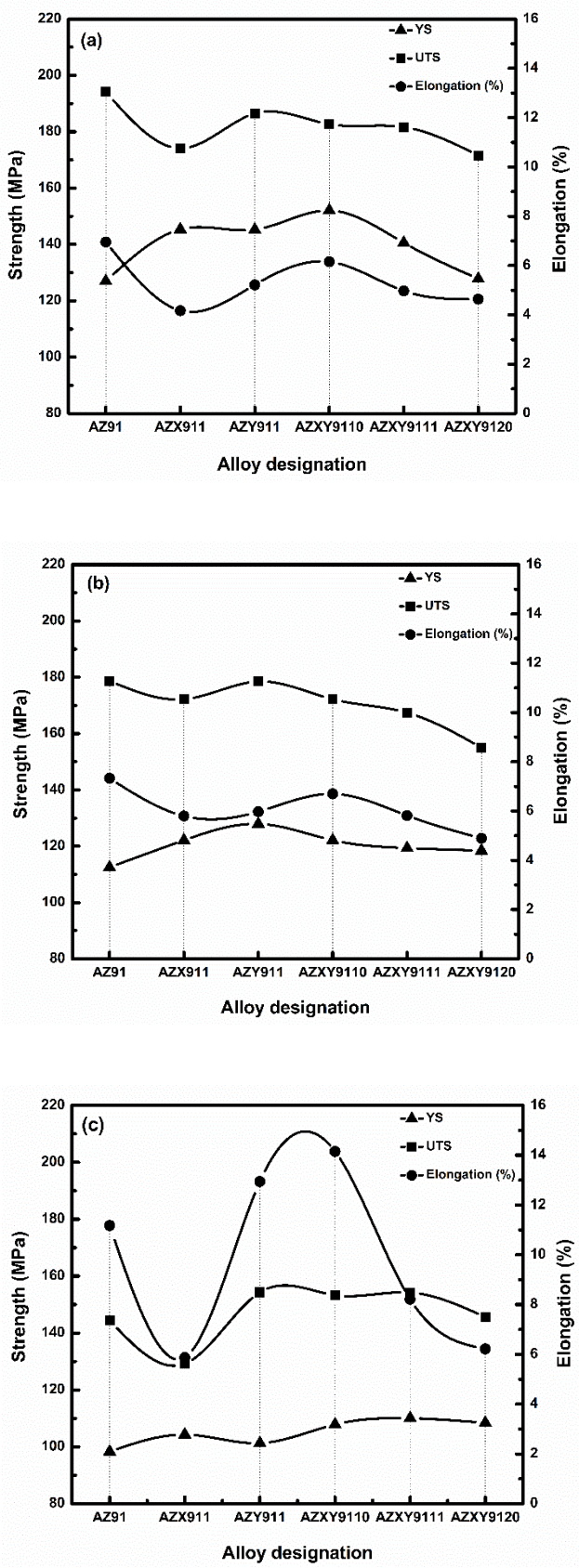

Fig. 5.2. Tensile properties of all the squeeze-cast alloys at (a) ambient, (b) 423 K and (c) 473 K temperatures.

Table 5.1: Comparison of the calculated (using Hall-Petch equation) and experimentally measured yield strength of the alloys.

Alloy	Calculated grain size (μm)	Calculated YS (MPa)	Experimentally obtained YS (MPa)
AZ91	26.4±3.0	106.7	127.0
AZX911	18.2±2.8	113.4	145.4
AZY911	19.4±2.1	112.2	145.3
AZXY9110	14.1±1.8	118.7	152.1
AZXY9111	17.5±2.1	114.2	140.6
AZXY9120	22.4±3.1	109.5	127.8

The thermally stable Al_2Ca, Mg_3Sb_2 and Ca_2Sb phases present in these alloys are brittle in nature, and especially Al_2Ca phase is prone to break because of its relatively higher brittleness than β-$Mg_{17}Al_{12}$ phase [17], which resulted in a worse combination of ductility and UTS. The coarse and reticular Al_2Ca phase distributed at the grain boundaries; the needle-shaped Mg_3Sb_2 phase distributed at the grain boundaries and within grain; as well as the presence of irregular Ca_2Sb phase might cut apart the matrix leading to the reduction of ductility and UTS in the alloys containing both individual and combined additions. Moreover, with an increase in Ca content from 0 to 2.0 (wt.%) hot tearing susceptibility increases significantly [14], which could be the plausible cause for deterioration of ductility and UTS of the alloys. Li et al. [14] too reported decreased ductility and UTS with improved YS in consequence of the enhanced hot tearing susceptibility following (0-1.0)Ca (wt.%) additions. Therefore, the additions of (0-2.0)Ca and (0-0.6)Sb (wt.%) on the microstructure and tensile properties of AZ91 alloys revealed dual effect. The additions refined the grains of the alloys and thereby improved their YS. On the other hand, due to the formation of Al_2Ca and Ca_2Sb phases, ductility and UTS of the alloys worsen. The relatively higher amount of Ca addition resulting larger volume fraction of Al_2Ca phase exhibited a more pronounced effect on tensile properties than that of Sb addition. The superior tensile properties of the AZXY9110 alloy was attributed to the presence of a negligible amount of brittle Al_2Ca and Ca_2Sb intermetallic phases resulting from the optimum content of Ca and Sb. However, the presence of higher amounts of Al_2Ca and Ca_2Sb phases in the microstructures of both the AZXY9111 (with relatively more Ca_2Sb phase) and AZXY9120 (with relatively more Al_2Ca phase) alloys as compared to that of the AZXY9110 alloy

deteriorates their tensile properties. Dramatically decrease in UTS in the AZXY9120 alloy with 2.0Ca (wt.%) addition signify that the connected network of Al_2Ca phase is definitely detrimental to UTS.

5.2 Fractured surface analysis

The micrograph of the fracture surface of the broken tensile specimen of AZXY9110 alloy, as a representative micrograph for the alloys containing combined additions, tested at ambient temperature is shown in Fig. 5.3(a). Evidently, the fracture surface reveals well-defined cleavage type of failure with multiple secondary cracks (shown by A). Numerous cleavage planes (shown by B) with cleavage steps of various sizes along with a few narrow river patterns (shown by C) were observed. These are the characteristic features of brittle transgranular cleavage fracture that represents brittle fracture occurring along crystallographic planes. Cleavage fracture consists of flat facets exhibiting river patterns that are caused by the cracks propagating inside the crystal lattice along several parallel planes leading to a series of plateaus and ledges [18]. It is well known that the commencement of microcracks is mostly influenced by the nature and presence of the second phase. In AZXY9110 alloy, the β-$Mg_{17}Al_{12}$ phase is very susceptible to fracture because of its brittleness [43]. When the load is applied during a tensile test, microcracks are likely to initiate at the eutectic formed along the grain boundaries, thereby making the alloy brittle. The formation of secondary cracks along the eutectic structure in the AZ91 alloy was concluded from microstructural analysis by Patel et al. [178]. The same is expected from Al_2Ca phase due to its relatively higher brittleness than β-$Mg_{17}Al_{12}$ phase. In some region, a quasi-cleavage plane (shown by D) with shallow dimples were also indicated. Additionally, a few micro voids (shown by E) and little plastic deformation (shown by F) were observed on the fracture surface.

The improvement in ductility and UTS in the AZXY9110 alloy tested at 473 K can be correlated to the fracture surface shown in Fig. 5.3(b). The micrograph exhibited a greater number of plastic deformation zones spread almost evenly over the entire fracture surface (shown by F) as compared to that of the specimen tested at ambient temperature. This ensures high elongation obtained at 473 K. Nevertheless, the existence of cleavage plane with secondary cracks observed along with the deformation zone ensures brittle fracture. In the specimen tested at 473 K, the fracture mode changed from cleavage to quasi-cleavage.

This is likely as a result of the activation of additional slip systems containing prismatic and pyramidal planes along which cross-slip takes place at elevated temperature [179] exhibiting higher ductility and UTS at 473 K. In quasi-cleavage type fracture, the cracks initiate and propagate locally and finally form a shallow dimple like morphology on the fracture surface. This is supported by the number of shallow dimples (shown by D) observed on the micrograph of the tensile fractured surface. In addition, the micro voids (shown by E) present on the fracture surface were also more. A significant amount of energy is consumed in the process of formation of the micro voids and for their subsequent coalescence under the applied tensile stress, which resulted in more ductility in the AZXY9110 alloy tested at 473 K.

In Table 5.2, the ambient temperature tensile properties of the squeeze-cast alloys are compared with the reported values of the tensile properties of the alloys produced by gravity-casting. It is obvious that the squeeze-cast alloys exhibited better tensile properties as compared to that of the alloys fabricated by gravity-casting. It is reported that the addition of Ca beyond 1.0 (wt.%) or Sb beyond 0.5 (wt.%) to AZ91 alloy fabricated by conventional casting is extremely harmful to ambient temperature mechanical properties and decreases both ductility and UTS drastically [12–15]. While the squeeze-cast AZ91-based alloys exhibited much better tensile properties than that produced by conventional casting even with high Ca and/or Sb content. The squeeze-cast AZ91 and AZXY9120 alloys exhibited 288.9% and 170.6% improvements in ductility with a corresponding 32.9% and 13.9% improvements in UTS, respectively, compared to the alloys prepared by gravity-casting by Yuán et al. [76]. Thus, the squeeze-casting has the potential to overcome the negative effect of ambient temperature tensile properties caused by the addition of Ca and/or Sb into AZ91 alloy.

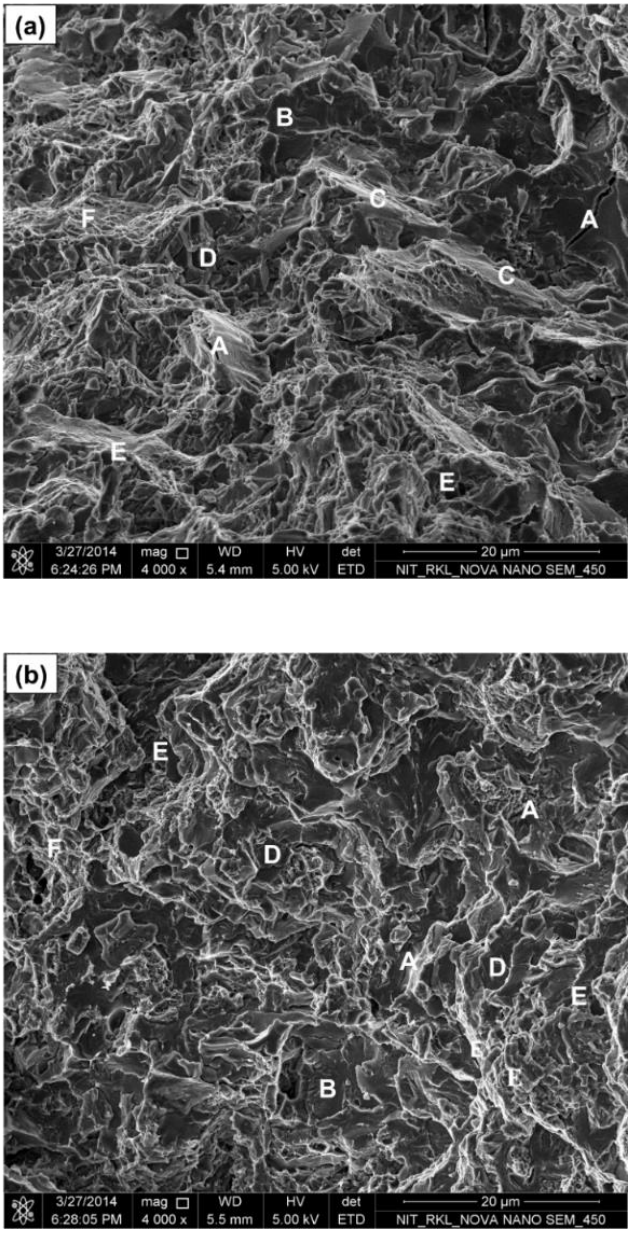

Fig. 5.3. Fracture surfaces of the broken tensile specimens of the squeeze-cast AZXY9110 alloy tested at (a) ambient and (b) 473 K temperatures.

Table 5.2: Comparison of ambient temperature tensile properties of the squeeze-cast alloys with that reported for the gravity-cast alloys.

Source	Alloy composition	Casting route	YS (MPa)	UTS (MPa)	%El
Wang et al. [13]	AZ91	GC	-	162.0	2.1
Guangyin et al. [7]	AZ91	GC	106.0	222.0	5.3
Hirai et al. [8]	AZ91	GC	-	228.0	3.7
Li et al. [14]	AZ91D	GC	71.7	161.1	1.7
Wu et al. [12]	AZ91D	GC	87.1	148.6	1.8
Boby et al. [180]	AZ91	GC	105.0	193.0	1.0
Yuán et al. [76]	AZ91	GC	-	146.0	1.8
Present study	AZ91	SC	127.0	194.0	7.0
Wu et al. [12]	AZ91-1Ca	GC	83.6	161.4	1.9
Li et al. [14]	AZ91D-1Ca	GC	86.7	138.9	1.0
Wang et al. [13]	AZ91-1Ca	GC	-	153.2	1.8
Present study	AZ91-1Ca (AZX911)	SC	145.4	174.1	4.2
Wang et al. [73]	AZ91-0.5Sb	GC	-	178.3	3.7
Boby et al. [180]	AZ91-0.5Sb	GC	109.0	215.0	2.0
Present study	AZ91-0.6Sb (AZY911)	SC	145.3	186.5	5.2
Yuán et al. [76]	AZ91-2Ca-0.4Sb	GC	-	151.0	1.7
Present study	AZ91-2Ca-0.3Sb (AZXY9120)	SC	128.0	172.0	4.6

5.3 Summary of Chapter 5

In this chapter, the ambient and elevated temperature tensile properties of all the modified AZ91 alloys are investigated. The main conclusions from the investigation are listed below:

i. Additions of both Ca and Sb increased YS at both ambient and elevated temperatures up to 473 K. However, both ductility and UTS decreased first up to 423 K and then increased at 473 K. The increase in YS was attributed to the grain refinement, whereas, the presence of brittle Al_2Ca, Mg_3Sb_2, and Ca_2Sb phases resulted in the reduction of ductility and UTS in the alloys.

ii. The best tensile properties were obtained in the AZXY9110 alloy owing to the presence of a negligible amount of brittle Al_2Ca, and Ca_2Sb phases resulted from the optimum content of 1.0Ca and 0.3Sb (wt.%).

iii. The fracture surface of the tensile specimen tested at ambient temperature confirmed cleavage failure that changed to quasi-cleavage at 473 K.

iv. The squeeze-cast alloys even with high Ca and/or Sb content exhibited better tensile properties overcoming the detrimental effects of Ca and/or Sb additions to AZ91 alloy compared to that of the gravity-cast alloys reported in the literature.

Chapter 6

Creep behaviour

This chapter deals with the detailed investigation of creep behaviour, using impression creep technique, of all the fabricated alloys. A correlation is made between the observed creep rates and the as-cast microstructures of all the alloys based on the dominant creep mechanism as well as post creep microstructural analysis. Finally, the observed trend on creep behaviour is further confirmed by carrying out conventional compressive creep tests on all the alloys.

6.1 Impression creep response

The typical impression creep curves (i.e. depth of penetration (h) vs. time (t)) obtained from all the fabricated alloys tested at a temperature of 473 K and stress of 480 MPa are shown in Fig. 6.1(a). To ascertain the attainment of steady state, the variation of impression velocity (i.e., dh/dt) with time (t) corresponding to Fig. 6.1(a) was plotted, and shown in Fig. 6.1(b). All the impression creep curves exhibited instantaneous impression depth along with well-defined primary (transient) and secondary creep stages. No tertiary creep stage was found owing to compressive nature of the test where necking did not take place. The absence of tertiary stage in impression creep test facilitated prolong secondary creep stage with stable deformation zone under the punch. The variation of impression velocity (dh/dt) with impression (punch) depth (h) corresponding to Fig. 6.1(a) is shown in Fig. 6.1(c). It is evident that following an initial instant punch velocity, the velocity remained mostly constant with further increase in punch depth. A steep decrease in punch velocity at the beginning of primary creep stage was observed. After this stage, test entered in a constant velocity region, i.e., secondary creep stage. The highest punch depth was recorded for the AZ91 alloy, whereas, the lowest was for the AZXY9120 alloy over the same time period. The slopes of the steady state zone (i.e., secondary stage) dropped by introducing Ca and Sb as alloying elements in the AZ91 alloy. It means Ca, and Sb restricted penetration of punch in the specimen, which indicated better creep resistance of the modified alloys. The steady state impression velocities calculated from the secondary stages of the curves in Fig.

6.1(a) are shown in Fig. 6.1(d). It is obvious that the additions of Ca and/or Sb to AZ91 alloy improved creep resistance as compared to the base alloy. The improvement was more pronounced by the combined additions (except AZXY9111) than the individual additions. The individual addition of Ca was better than the Sb addition. Among the modified alloys the AZXY9120 containing 2.0Ca and 0.3Sb (wt.%) exhibited the best creep resistance at the temperature and stress levels employed. Further increase in Sb content from 0.3 to 0.6 (wt.%) in the AZXY9111 alloy decreased its creep resistance, and it was inferior to that of the alloy pertaining individual addition of Ca, i.e., AZX911. The creep rate of the AZXY9110 alloy containing 1.0Ca and 0.3Sb (wt.%) was superior to that of the AZXY9111 alloy and inferior to that of the AZXY9120 alloy.

In order to examine the effect of temperature and stress on impression creep behaviour, all the alloys were tested at different temperature and stress levels. Creep plots corresponding to the base AZ91 alloy and AZXY9120 alloy as a representative for the modified alloys are shown in Fig. 6.2 and 6.3, respectively. With the increase in both temperature and stress, slopes of all the curves increased, and the effect was more pronounced with an increase in temperature as creep rate depends exponentially on it. It was observed that at high temperature and stress, creep resistance of the AZXY9120 alloy was far better than that of the AZ91 alloy. 3D representations depicting temperature and stress dependence of the steady state impression velocities for both the AZ91 and AZXY9120 alloys are shown in Fig. 6.4(a and b). It is obvious that the dependence of impression velocity on temperature and stress is more pronounce in the AZ91 alloy. It exhibited very high impression velocity at 498 K itself, and therefore, it was not tested further at a higher temperature (i.e., 523 K) at the stress levels mentioned. The steady state impression velocities of the AZ91 alloy produced by different casting techniques are summarized in Table 6.1. It is obvious that the squeeze-cast alloys exhibited superior creep behaviour as compared to that of the alloys fabricated by gravity-casting and HPDC, which is in line with the reported literature [38,39].

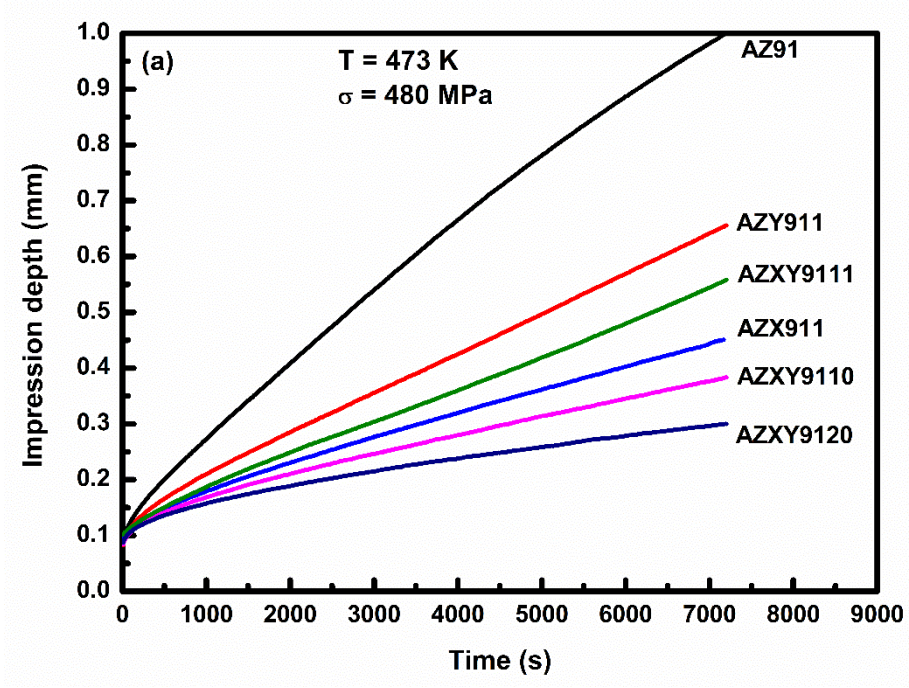
(a)
T = 473 K
σ = 480 MPa
AZ91
AZY911
AZXY9111
AZX911
AZXY9110
AZXY9120
Impression depth (mm)
Time (s)
0.0
0.1
0.2
0.3
0.4
0.5
0.6
0.7
0.8
0.9
1.0
0
1000
2000
3000
4000
5000
6000
7000
8000
9000

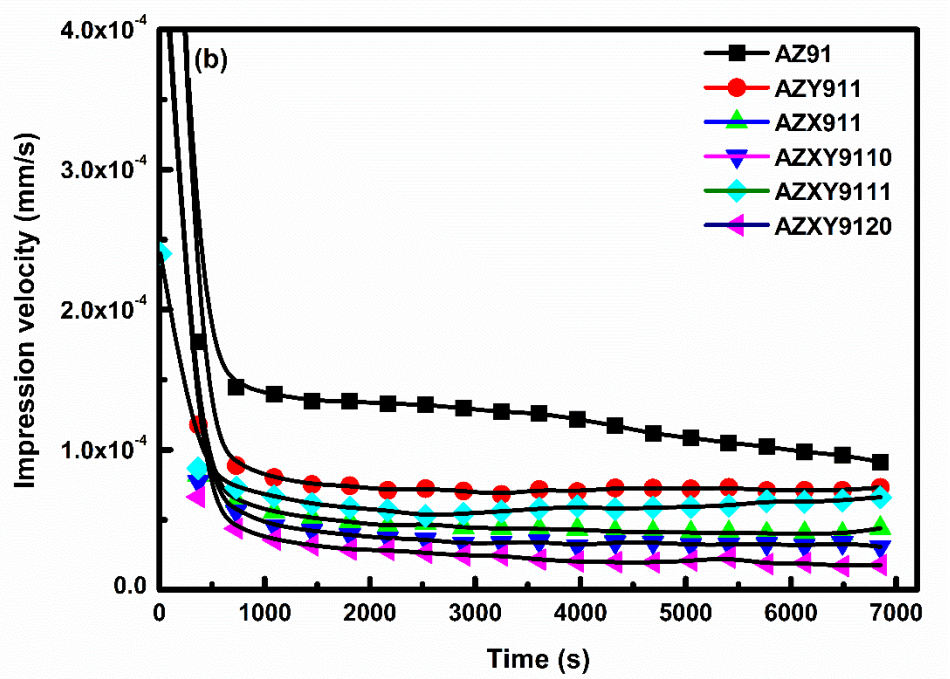
(b)
AZ91
AZY911
AZX911
AZXY9110
AZXY9111
AZXY9120
Impression velocity (mm/s)
Time (s)
4.0x10-4
3.0x10-4
2.0x10-4
1.0x10-4
0.0
0
1000
2000
3000
4000
5000
6000
7000

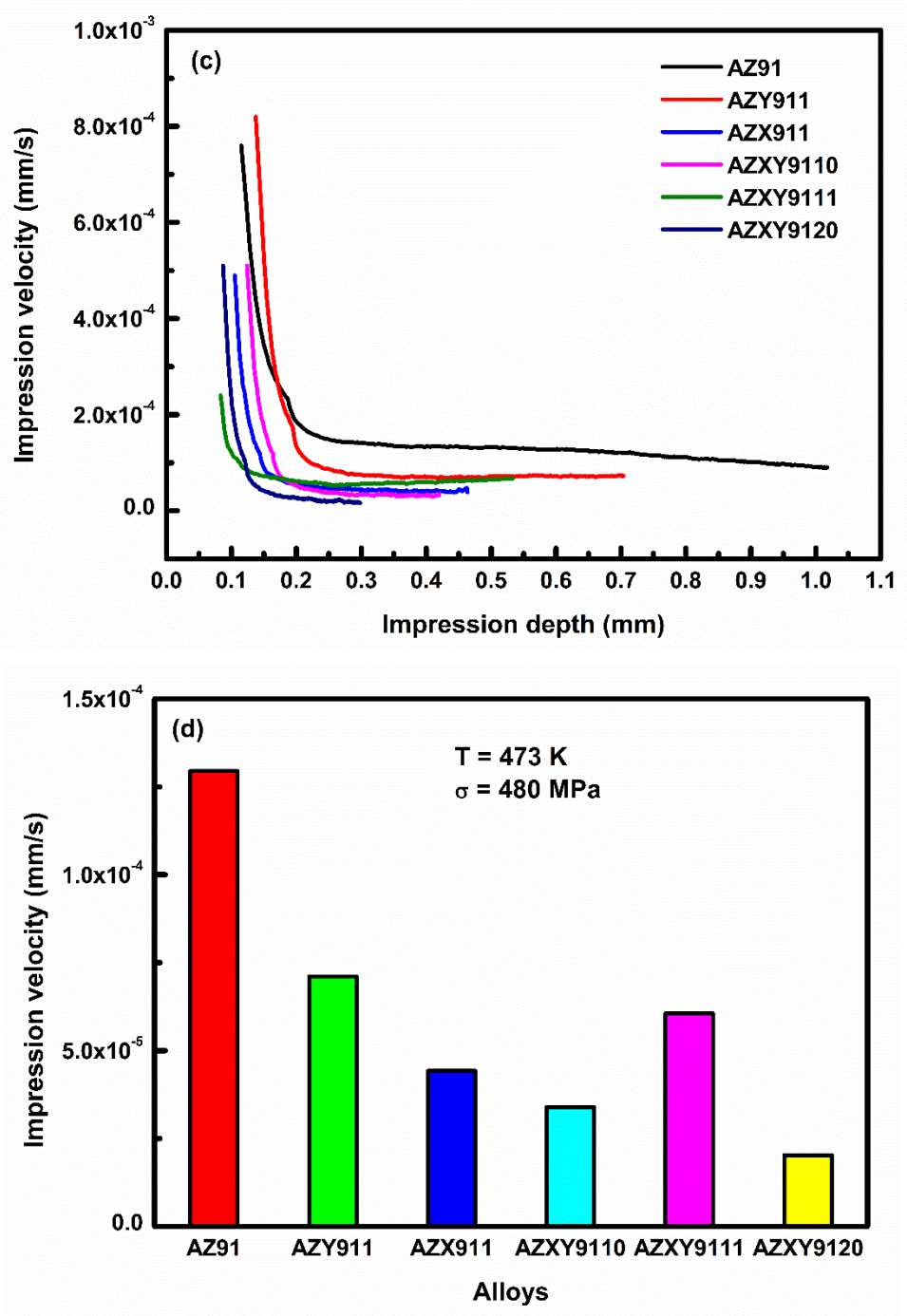

Fig. 6.1. (a) Typical impression depth vs. time plots for all the alloys creep tested at 480 MPa stress and temperatures of 473 K; and variation of (b) impression velocity with time, (c) impression velocity with depth, (d) steady state impression velocities corresponding to (a).

Table 6.1: Summary of steady state impression velocities of the AZ91 alloy produced by different casting techniques.

Source	**Casting route**	**Steady state impression velocities (mm/s)**					
Present study	Squeeze-cast		**300 MPa**	**345 MPa**	**390 MPa**	**435 MPa**	**480 MPa**
		498 K	2.43×10^{-5}	6.12×10^{-5}	1.24×10^{-4}	2.37×10^{-4}	4.03×10^{-4}
		473 K	6.20×10^{-6}	1.34×10^{-5}	3.12×10^{-5}	7.63×10^{-5}	1.04×10^{-4}
		448 K	1.10×10^{-6}	2.75×10^{-6}	5.25×10^{-6}	1.02×10^{-5}	1.47×10^{-5}
		423 K	5.71×10^{-7}	1.12×10^{-6}	1.88×10^{-6}	4.38×10^{-6}	6.06×10^{-6}
Mahmudi and Moeendarbari [111]	Gravity-cast		**300 MPa**	**350 MPa**	**400 MPa**	**450 MPa**	**500 MPa**
		498 K	2.91×10^{-5}	7.42×10^{-5}	1.40×10^{-4}	-	-
		473 K	8.97×10^{-6}	2.40×10^{-5}	3.41×10^{-5}	7.74×10^{-5}	1.27×10^{-4}
		448 K	-	-	1.10×10^{-5}	1.94×10^{-5}	3.57×10^{-5}
Kabirian and Mahmudi [112]	Gravity-cast		**300 MPa**	**350 MPa**	**400 MPa**	**450 MPa**	**500 MPa**
		485 K	8.73×10^{-6}	1.79×10^{-5}	4.86×10^{-5}	7.17×10^{-5}	1.25×10^{-4}
		455 K	1.47×10^{-6}	4.01×10^{-6}	9.47×10^{-6}	1.82×10^{-5}	2.53×10^{-5}
		425 K	-	-	-	3.01×10^{-6}	6.71×10^{-6}
Nami et al. [114]	HPDC		**295 MPa**	**330 MPa**	**370 MPa**	**415 MPa**	**450 MPa**
		485 K	4.11×10^{-5}	5.95×10^{-5}	1.11×10^{-4}	2.28×10^{-4}	4.79×10^{-4}
		470 K	8.78×10^{-6}	1.76×10^{-5}	3.23×10^{-5}	7.70×10^{-5}	9.78×10^{-5}
		450 K	2.36×10^{-6}	6.14×10^{-6}	1.56×10^{-5}	2.21×10^{-5}	2.87×10^{-5}
		425 K	4.19×10^{-7}	1.04×10^{-6}	2.48×10^{-6}	3.44×10^{-6}	7.52×10^{-6}

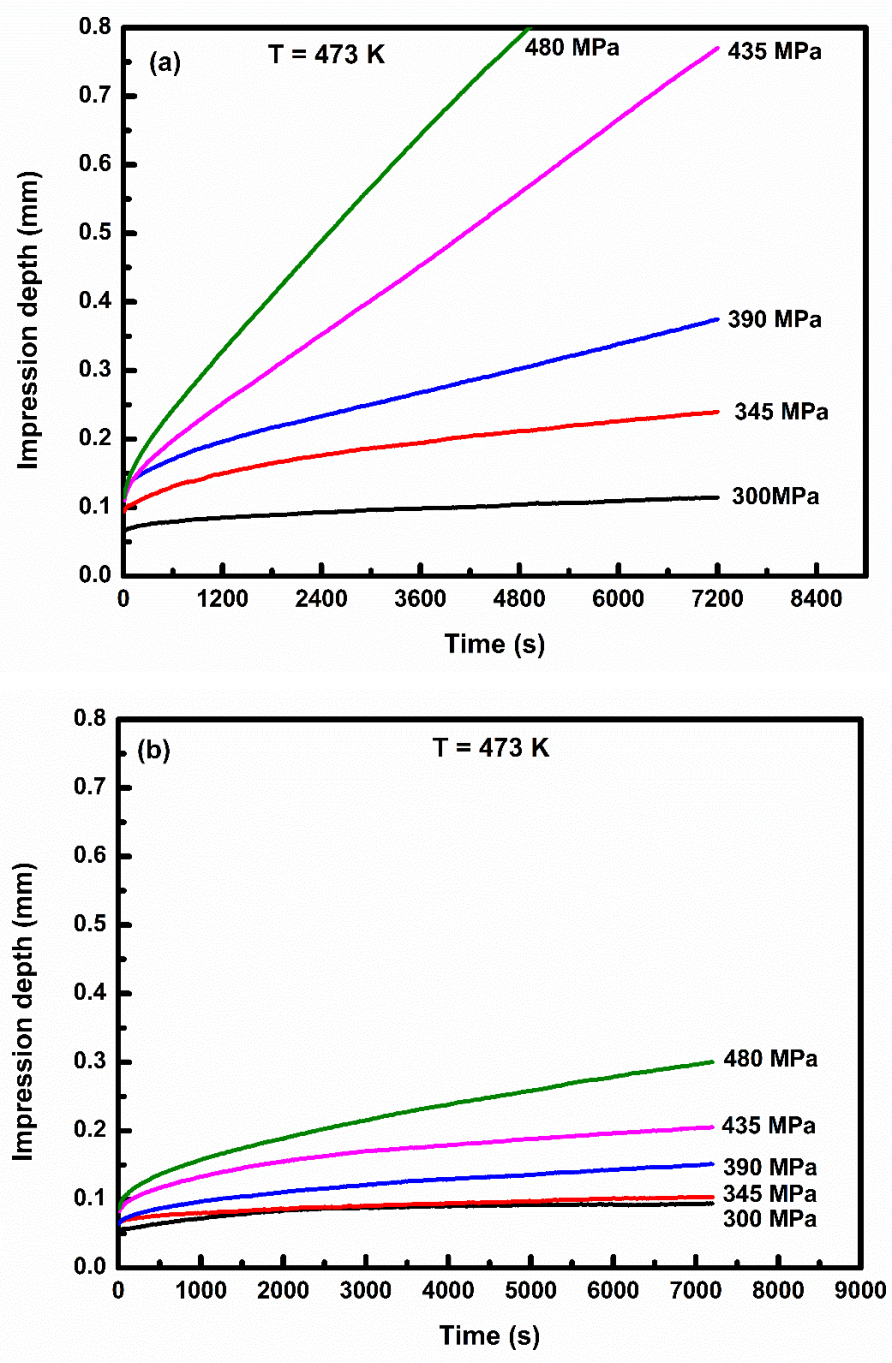

Fig. 6.2. Effect of applied stress on impression depth at constant temperature for the (a) AZ91 and (b) AZXY9120 alloys.

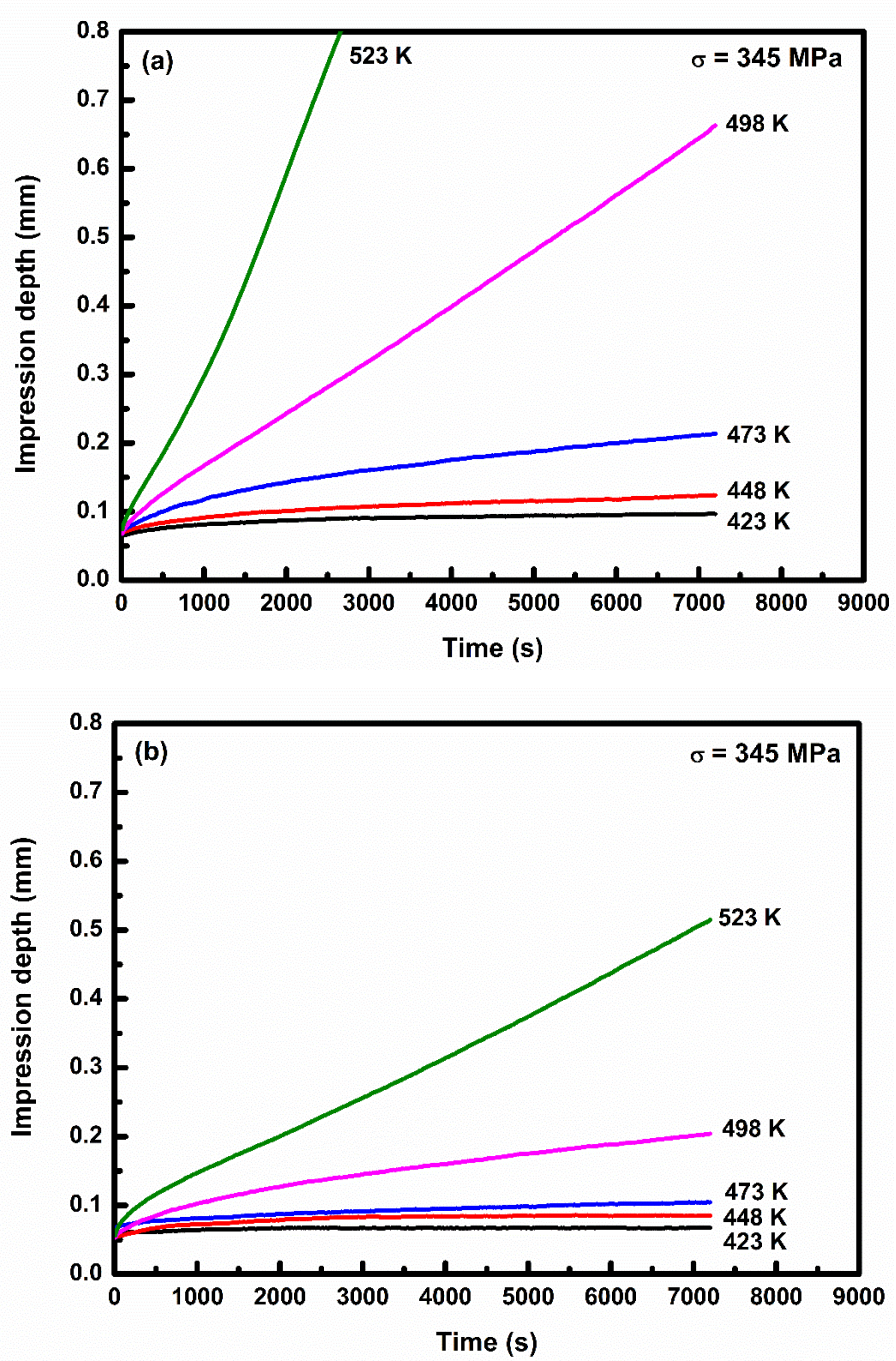

Fig. 6.3. Effect of temperature on impression depth at constant stress for the (a) AZ91 and (b) AZXY9120 alloys.

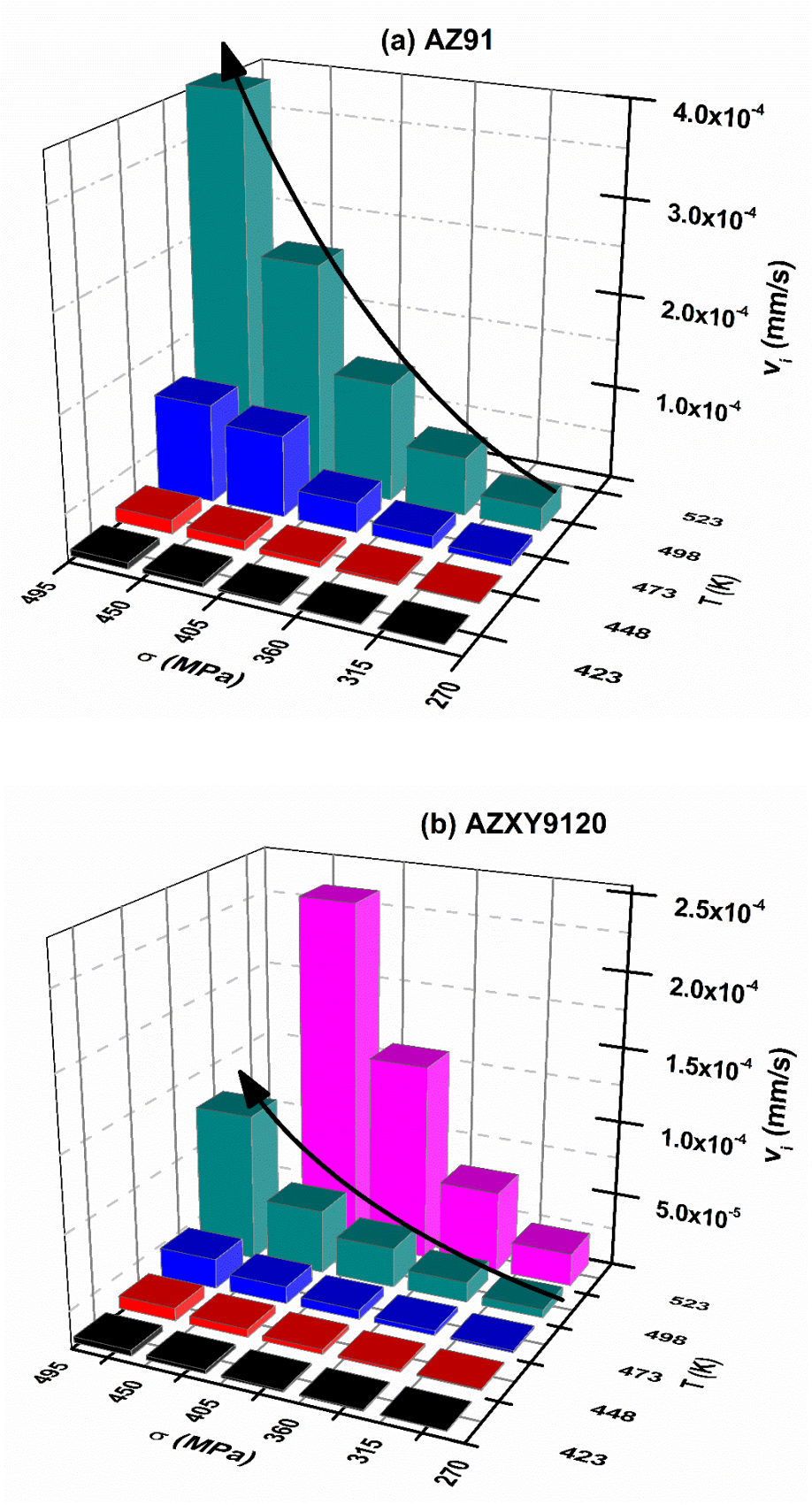

Fig. 6.4. 3D representations depicting the effect of both temperature and stress on steady state impression velocities for the (a) AZ91 and (b) AZXY9120 alloys.

In AZ91 alloy, the appearance of the β-$Mg_{17}Al_{12}$ phase in microstructure is vital in determining its creep behaviour. The melting point of the β-$Mg_{17}Al_{12}$ phase (710 K) is low, and accordingly, it gets soften and coarsen with increase in temperature. This aspect severely affects grain boundary strength of the AZ91 alloy at an elevated temperature resulting its poor creep resistance [112,181–183]. EPMA elemental mapping taken from the as-cast AZ91 alloy is shown in Fig. 6.5. Rapid solidification rate associated with squeeze-casting resulted in supersaturation of Al at the region immediately next to grain boundaries, which might contribute to solid solution strengthening of the alloy to some extent. However, β-$Mg_{17}Al_{12}$ phase precipitated out from the supersaturated α-Mg during a long exposure at elevated temperature, which negatively contributed to creep resistance of the AZ91 alloy.

Complete suppression and partial inhibition of the β-$Mg_{17}Al_{12}$ phase by introducing thermally stable intermetallic compounds in microstructure are the possible ways to improve creep resistance of the AZ91 alloy. Both Ca and Sb additions to AZ91 alloy produced intermetallic compounds that were stable at elevated temperature. The addition of Ca in the AZ91 alloy formed Al_2Ca phase that was thermally stable. Further, during solidification, some amount of Ca was trapped in the β-$Mg_{17}Al_{12}$ phase, which improved its thermal stability by increasing its melting point [70,104]. Thus, the introduction of intermetallic Al_2Ca phase in the microstructure and partial improvement of melting point of β-$Mg_{17}Al_{12}$ phase directly translated into better creep resistance of the Ca containing alloy.

The addition of Sb to AZ91 also improved its creep resistance. Rod-shaped Mg_3Sb_2 particles bridged grain boundaries, and few were even stretched into both grains, as shown in Fig. 4.3(b). High thermal stability of the Mg_3Sb_2 phase (M. P. 1501 K) made it suitable for hindering grain boundary sliding at elevated temperature. Guangyin et al. [106] checked thermal stability of the phase and observed no change in shape or size following 12 h solution treatment at 693 K. Discontinuous precipitations of β-$Mg_{17}Al_{12}$ as present in the AZ91 alloy was not observed in the alloy with Sb addition. Unlike Ca addition, Sb could not enhance thermal stability of the β-$Mg_{17}Al_{12}$ phase, as the later was not dissolved in it. Thus, Sb added alloy exhibited better creep resistance than the AZ91 alloy; however, it was inferior to the other modified alloys.

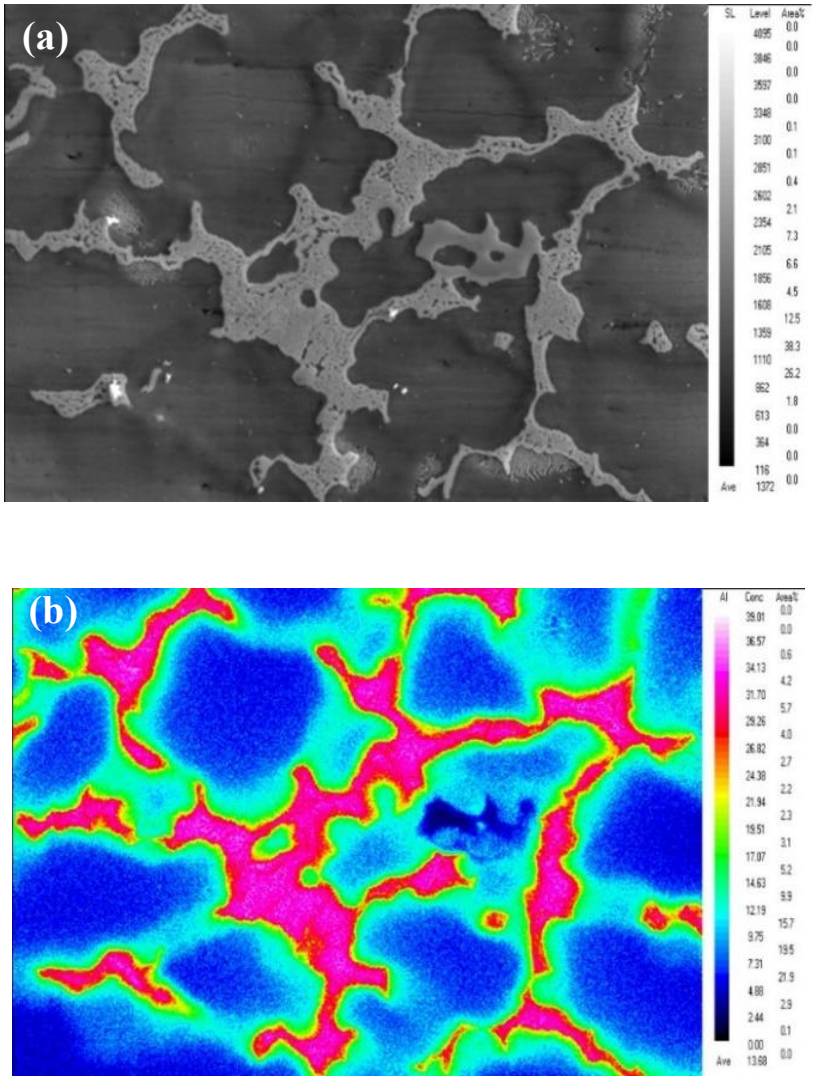

Fig. 6.5. EPMA elemental mapping corresponding to Al present in the AZ91 alloy.

Combined additions of Ca and Sb to the AZ91 alloy resulted in Al_2Ca and Ca_2Sb intermetallic phases formation along with β-$Mg_{17}Al_{12}$ phase. Among the alloys pertaining combined additions, the AZXY9120 alloy exhibited the best creep resistance. The superior creep resistance was attributed to the reduced amount of β-$Mg_{17}Al_{12}$ phase and relatively higher content of Al_2Ca phase. The lamellar Al_2Ca phase prevented grain boundary sliding efficiently. The rigid network of the Al_2Ca phase slowed down recovery process, restraining slips within grains. EPMA elemental mapping corresponding to Al in the AZXY9120 alloy is shown in Fig. 6.6. Negligible Al supersaturation in α-Mg was observed, and therefore, the contribution from solid solution strengthening of Al was not significant. However, it reduced the risk of precipitating out of the β-$Mg_{17}Al_{12}$ phase from α-Mg during long exposure at elevated temperature, which also positively contributed in improving creep resistance of the AZXY9120 alloy. The Sb-containing particles in the AZXY9120 alloy were Ca_2Sb, and its melting point is 1100 K. This phase too thermally stable owing to its higher melting point. Thermal stability of the Al_2Ca phase is more compared to the Ca_2Sb phase because of higher melting point (i.e., 1352 K) of the former phase. Both Al_2Ca and Ca_2Sb phases being thermally stable contributed positively to improve creep resistance of the AZXY9120 alloy. However, the volume fraction of the Ca_2Sb phase was very less and accordingly, the contribution from Ca_2Sb was negligible as compared to that by Al_2Ca phase. It was not possible to separate out the contribution arising out of the individual phase to improve creep resistance of the AZXY9120 alloy. Creep resistance of the AZXY9110 alloy was slightly inferior to the AZXY9120 alloy owing to lower Ca content in the former alloy. The AZXY9111 alloy pertaining further higher amount of Sb, i.e., 0.6 (wt.%) exhibited creep resistance inferior to the AZXY9110 alloy. Higher content of Ca and Sb in the AZXY9111 alloy resulted in the higher amount of Ca_2Sb phase as the highest electronegativity difference exists between the two elements, resulting a lower amount of Al_2Ca phase formation. Thus, the presence of significant percentage of β-$Mg_{17}Al_{12}$ phase along with the relatively lower amount of Al_2Ca and Ca_2Sb phases in the AZXY9111 alloy deterred its creep resistance.

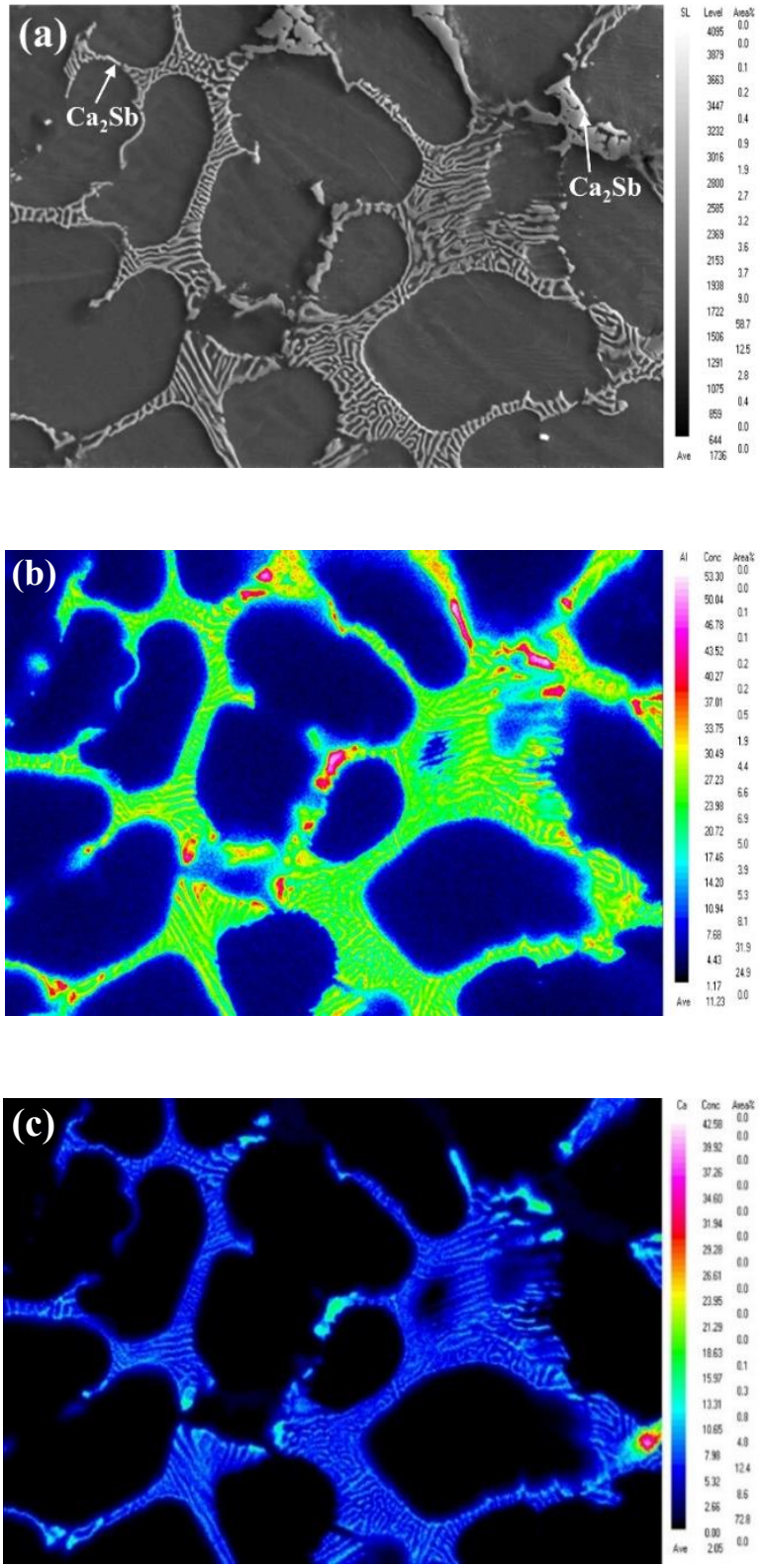

Fig. 6.6. EPMA elemental mapping corresponding to Al and Ca present in the AZXY9120 alloy.

6.2 Assessment of creep mechanism

Temperature (T) and applied stress (σ) have a profound effect on minimum creep rate ($\dot{\varepsilon}$) of metals and alloys, and the correlation among them is usually described by the Norton–Arrhenius equation as follows:

$$\dot{\varepsilon} = \frac{ADGb}{kT}\left(\frac{\sigma}{G}\right)^n \tag{6.1}$$

where A is a material constant, D is diffusion coefficient, G is shear modulus, b is burgers vector, k is Boltzmann constant, and T is absolute temperature. The diffusion coefficient is generally expressed as:

$$D = D_0 e^{\left(-\frac{Q}{RT}\right)} \tag{6.2}$$

where D_0 is a pre-exponential factor for diffusion (frequency factor) and Q is apparent activation energy. On the basis of equations 6.1 and 6.2, Mukherjee et al. [89] proposed an empirical relation for metals and alloys, which is well known as Mukherjee-Bird-Dorn equation.

$$\dot{\varepsilon} = \frac{AD_0Gb}{kT}\left(\frac{\sigma}{G}\right)^n e^{\left(-\frac{Q}{RT}\right)} \tag{6.3}$$

Incorporating grain size effect on creep behaviour the equation takes the following form

$$\dot{\varepsilon} = A\left(\frac{b}{d}\right)^p \left(\frac{D_0Gb}{kT}\right)\left(\frac{\sigma}{G}\right)^n e^{\left(-\frac{Q}{RT}\right)} \tag{6.4}$$

where d is grain size and p is grain size exponent. Equations 6.3 and 6.4 are well-known power law equations for creep and depict creep mechanism very accurately for a wide range of applied stresses. For correlating impression creep results with that of conventional creep the following conversion were proposed in the literature [107,184]

$$\sigma = \frac{\sigma_i}{c_1} \tag{6.5}$$

and,

$$\dot{\varepsilon} = \frac{v_i}{\emptyset c_2} \tag{6.6}$$

where, σ_i = impression stress = $\frac{4L}{\pi\emptyset^2}$, v_i = impression velocity = $\frac{dh}{dt}$

h = impression depth, L = load applied, $\emptyset$ = punch diameter, $c_1 \cong 3$ and $c_2 \cong 1$

With the help of equations 6.5 and 6.6, the equation 6.4 can be written as

$$\frac{v_i T}{G} = A_1 \left(\frac{\sigma_i}{G}\right)^n e^{\left(-\frac{Q}{RT}\right)} \qquad 6.7$$

where $A_1 = \frac{A\emptyset b c_2 D_0}{k c_1^n}\left(\frac{b}{d}\right)^p$ is a constant.

It was reported that the value of shear modulus was explicitly dependent on experimental temperature and it was calculated for the AZ91 alloy by the following equation [183]:

$$G\ (MPa) = 18460 - 8.2T(K) \qquad 6.8$$

The values of stress exponents were calculated by plotting $\ln(v_i T/G)$ against $\ln(\sigma_i/G)$ at a particular temperature, as shown in Fig. 6.7. The values of activation energies were calculated by plotting $\ln(v_i T/G)$ against $1/T$ at a constant applied stress, as shown in Fig. 6.8. The activation energy along with stress exponent were used to determine the dominant creep mechanism. The creep mechanism operated in pure Mg and its alloys are diffusion creep for n=1, grain boundary sliding for n=2 and dislocation creep for n=3-7. The information about particular diffusion mode in specific creep deformation mechanism is provided by the value of corresponding activation energy. Its value close to that required for lattice self-diffusion of Mg i.e., 135 kJ/mol along with stress exponent values from 4 to 6 suggested dislocation climb-controlled by lattice self-diffusion is the dominant creep mechanism.

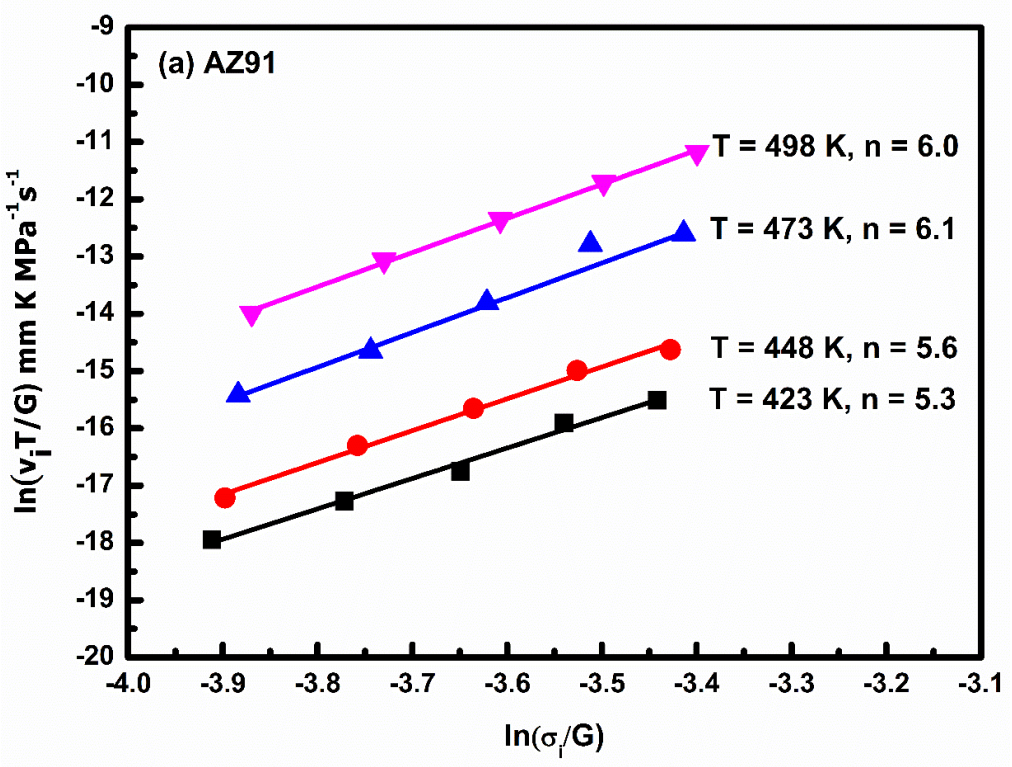
(a) AZ91
T = 498 K, n = 6.0
T = 473 K, n = 6.1
T = 448 K, n = 5.6
T = 423 K, n = 5.3
ln(v_i T/G) mm K MPa^-1 s^-1
ln(σ_i/G)
-9
-10
-11
-12
-13
-14
-15
-16
-17
-18
-19
-20
-4.0
-3.9
-3.8
-3.7
-3.6
-3.5
-3.4
-3.3
-3.2
-3.1

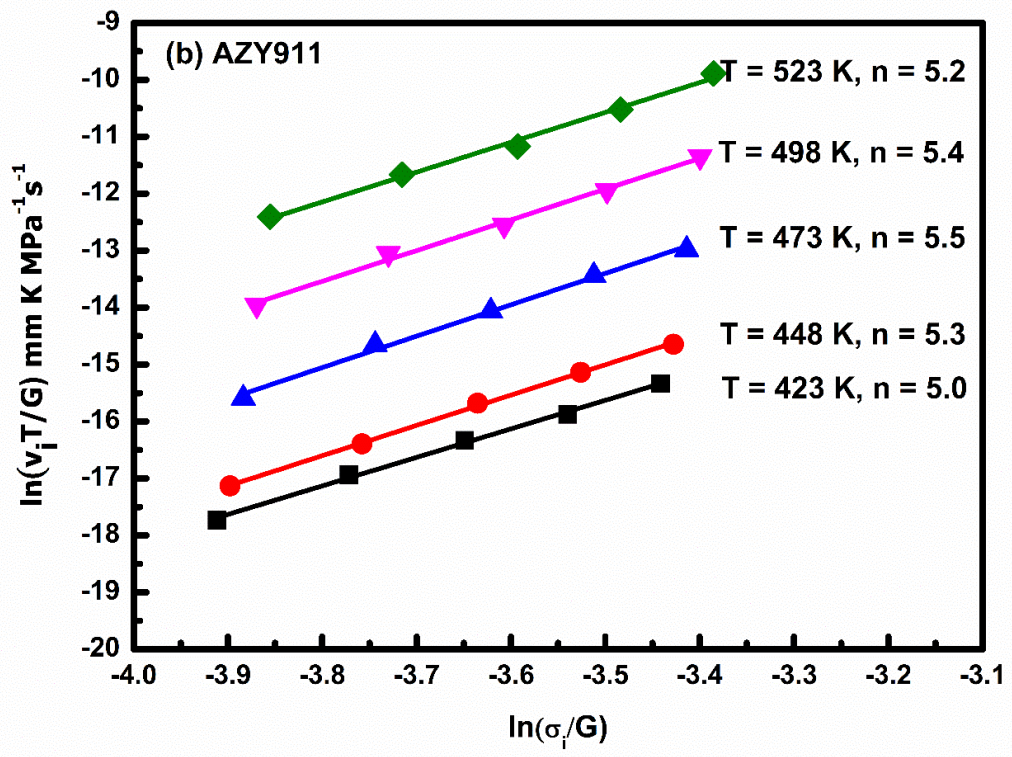
(b) AZY911
T = 523 K, n = 5.2
T = 498 K, n = 5.4
T = 473 K, n = 5.5
T = 448 K, n = 5.3
T = 423 K, n = 5.0
ln(v_i T/G) mm K MPa^-1 s^-1
ln(σ_i/G)
-9
-10
-11
-12
-13
-14
-15
-16
-17
-18
-19
-20
-4.0
-3.9
-3.8
-3.7
-3.6
-3.5
-3.4
-3.3
-3.2
-3.1

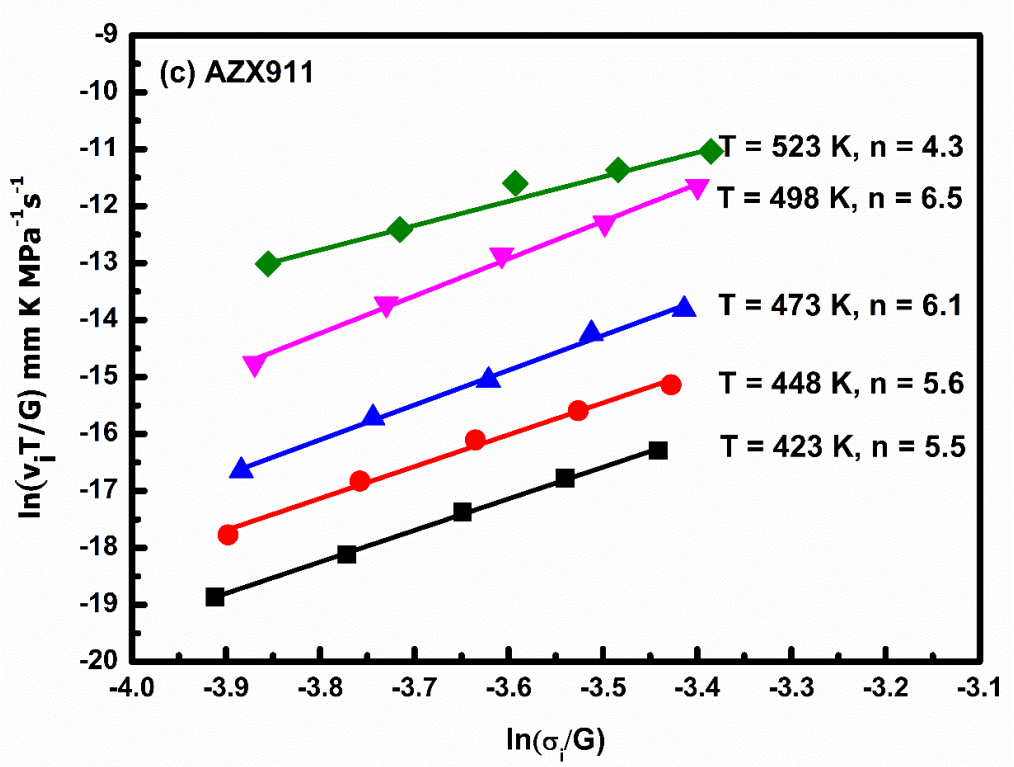
(c) AZX911
T = 523 K, n = 4.3
T = 498 K, n = 6.5
T = 473 K, n = 6.1
T = 448 K, n = 5.6
T = 423 K, n = 5.5
ln(v_i T/G) mm K MPa^-1 s^-1
ln(σ_i/G)
-9
-10
-11
-12
-13
-14
-15
-16
-17
-18
-19
-20
-4.0
-3.9
-3.8
-3.7
-3.6
-3.5
-3.4
-3.3
-3.2
-3.1

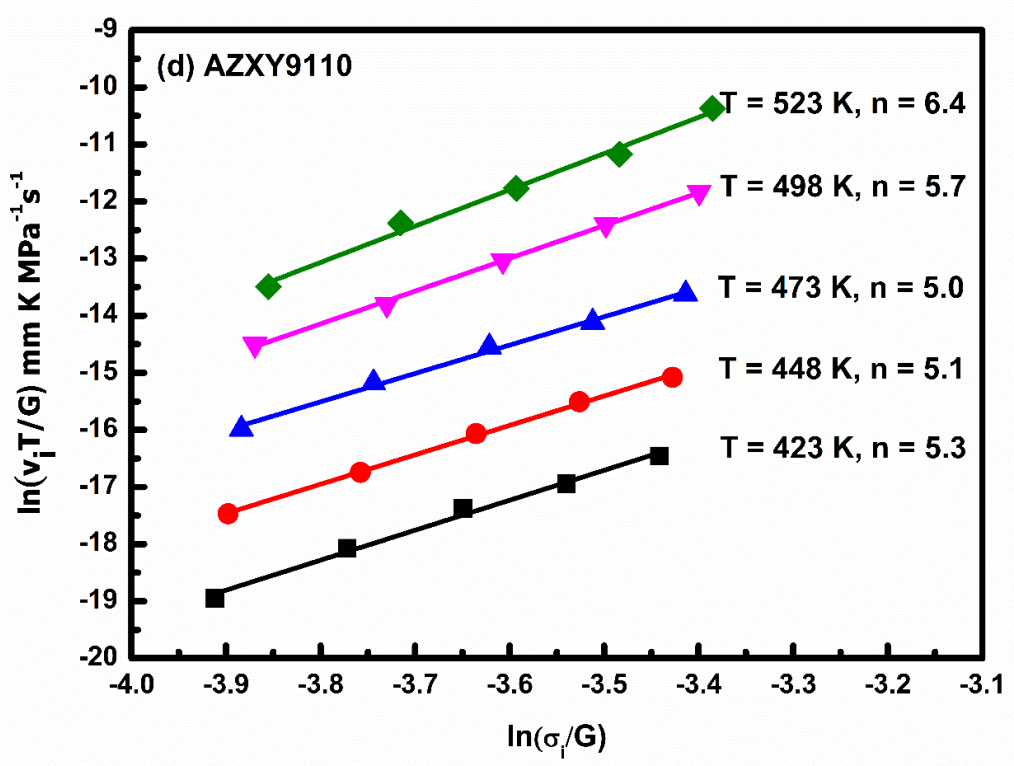
(d) AZXY9110
T = 523 K, n = 6.4
T = 498 K, n = 5.7
T = 473 K, n = 5.0
T = 448 K, n = 5.1
T = 423 K, n = 5.3
ln(v_i T/G) mm K MPa^-1 s^-1
ln(σ_i/G)
-9
-10
-11
-12
-13
-14
-15
-16
-17
-18
-19
-20
-4.0
-3.9
-3.8
-3.7
-3.6
-3.5
-3.4
-3.3
-3.2
-3.1

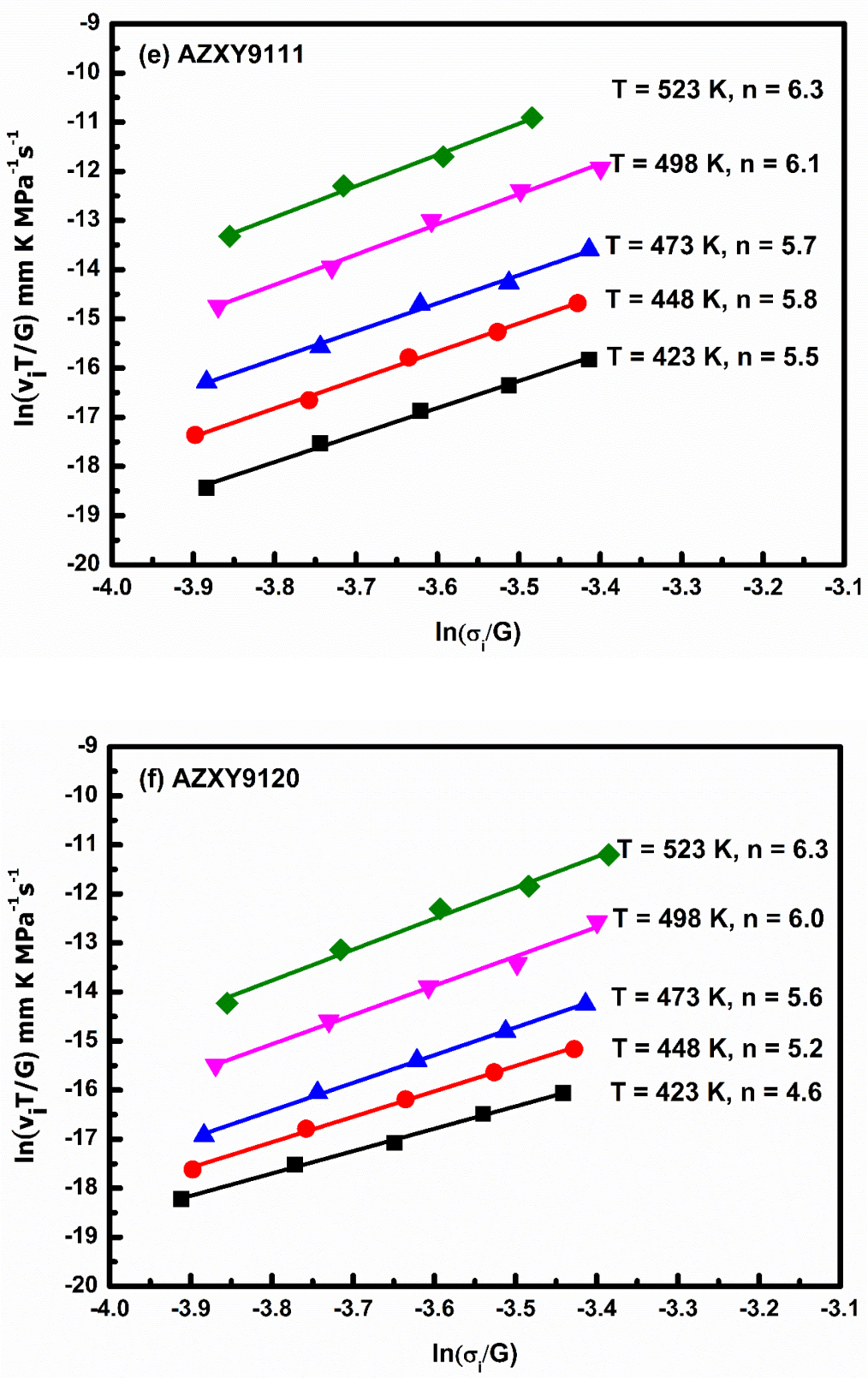

Fig. 6.7. Stress dependence of the steady state impression velocities at different temperatures for the (a) AZ91, (b) AZY911, (c) AZX911, (d) AZXY9110, (e) AZXY9111, and (f) AZXY9120 alloys.

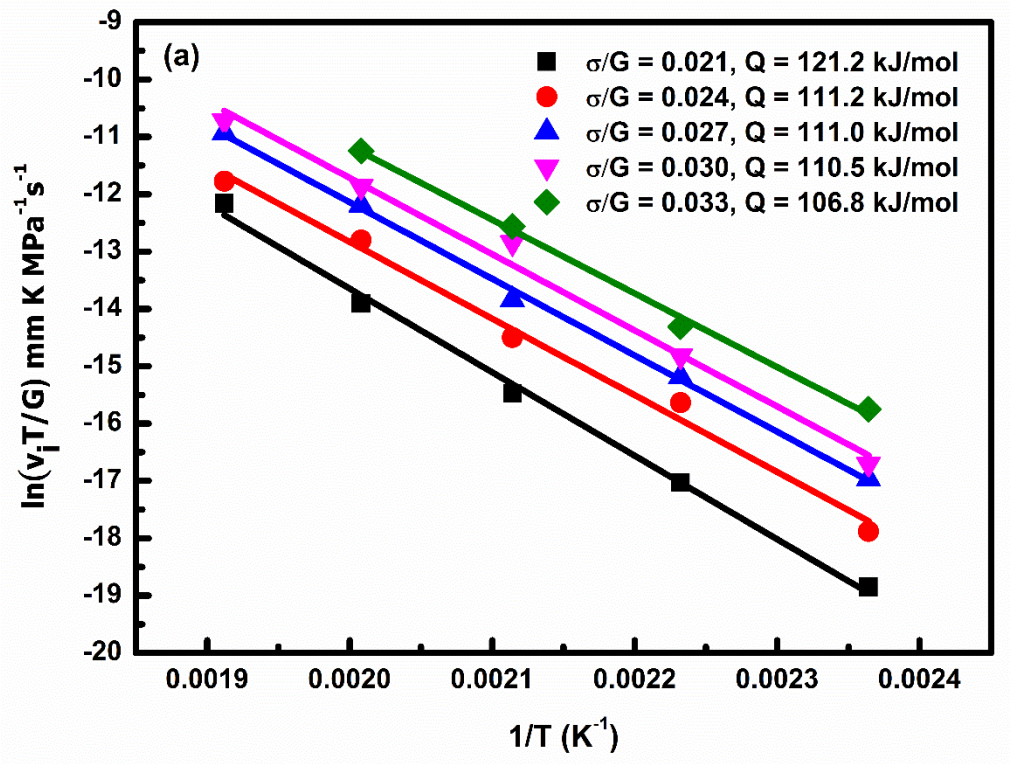
(a)
σ/G = 0.021, Q = 121.2 kJ/mol
σ/G = 0.024, Q = 111.2 kJ/mol
σ/G = 0.027, Q = 111.0 kJ/mol
σ/G = 0.030, Q = 110.5 kJ/mol
σ/G = 0.033, Q = 106.8 kJ/mol
ln(v_jT/G) mm K MPa^-1 s^-1
1/T (K^-1)
-9
-10
-11
-12
-13
-14
-15
-16
-17
-18
-19
-20
0.0019
0.0020
0.0021
0.0022
0.0023
0.0024

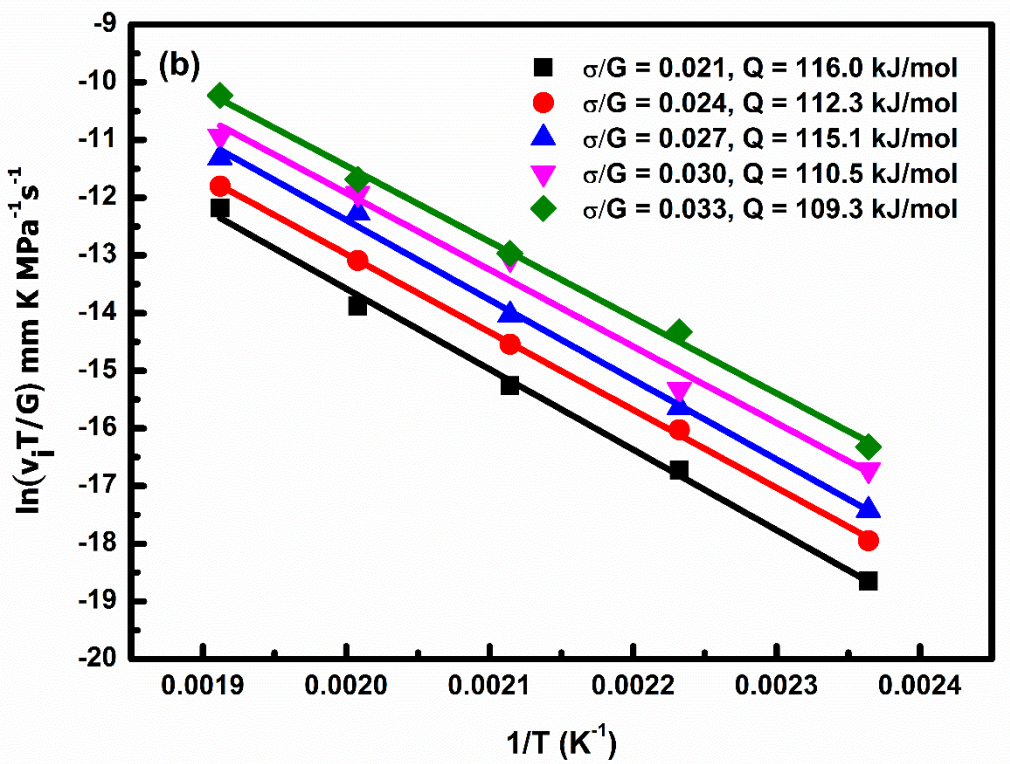
(b)
σ/G = 0.021, Q = 116.0 kJ/mol
σ/G = 0.024, Q = 112.3 kJ/mol
σ/G = 0.027, Q = 115.1 kJ/mol
σ/G = 0.030, Q = 110.5 kJ/mol
σ/G = 0.033, Q = 109.3 kJ/mol
ln(v_jT/G) mm K MPa^-1 s^-1
1/T (K^-1)
-9
-10
-11
-12
-13
-14
-15
-16
-17
-18
-19
-20
0.0019
0.0020
0.0021
0.0022
0.0023
0.0024

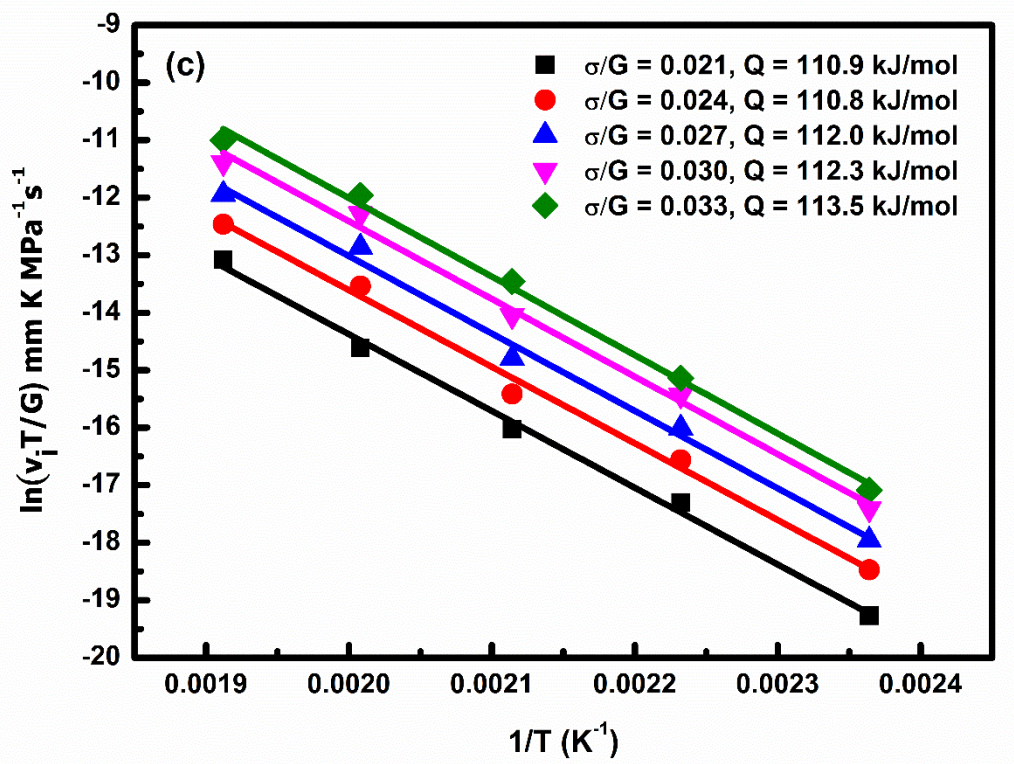
(c)
σ/G = 0.021, Q = 110.9 kJ/mol
σ/G = 0.024, Q = 110.8 kJ/mol
σ/G = 0.027, Q = 112.0 kJ/mol
σ/G = 0.030, Q = 112.3 kJ/mol
σ/G = 0.033, Q = 113.5 kJ/mol
ln(v_i T/G) mm K MPa^-1 s^-1
1/T (K^-1)
-9
-10
-11
-12
-13
-14
-15
-16
-17
-18
-19
-20
0.0019
0.0020
0.0021
0.0022
0.0023
0.0024

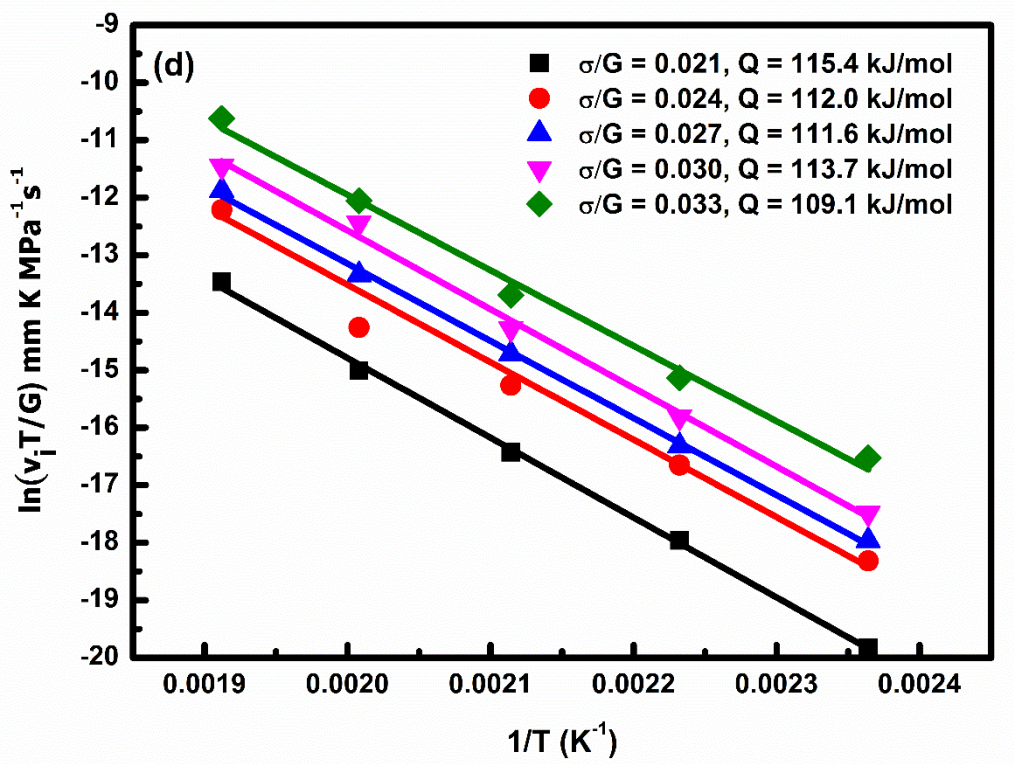
(d)
σ/G = 0.021, Q = 115.4 kJ/mol
σ/G = 0.024, Q = 112.0 kJ/mol
σ/G = 0.027, Q = 111.6 kJ/mol
σ/G = 0.030, Q = 113.7 kJ/mol
σ/G = 0.033, Q = 109.1 kJ/mol
ln(v_i T/G) mm K MPa^-1 s^-1
1/T (K^-1)
-9
-10
-11
-12
-13
-14
-15
-16
-17
-18
-19
-20
0.0019
0.0020
0.0021
0.0022
0.0023
0.0024

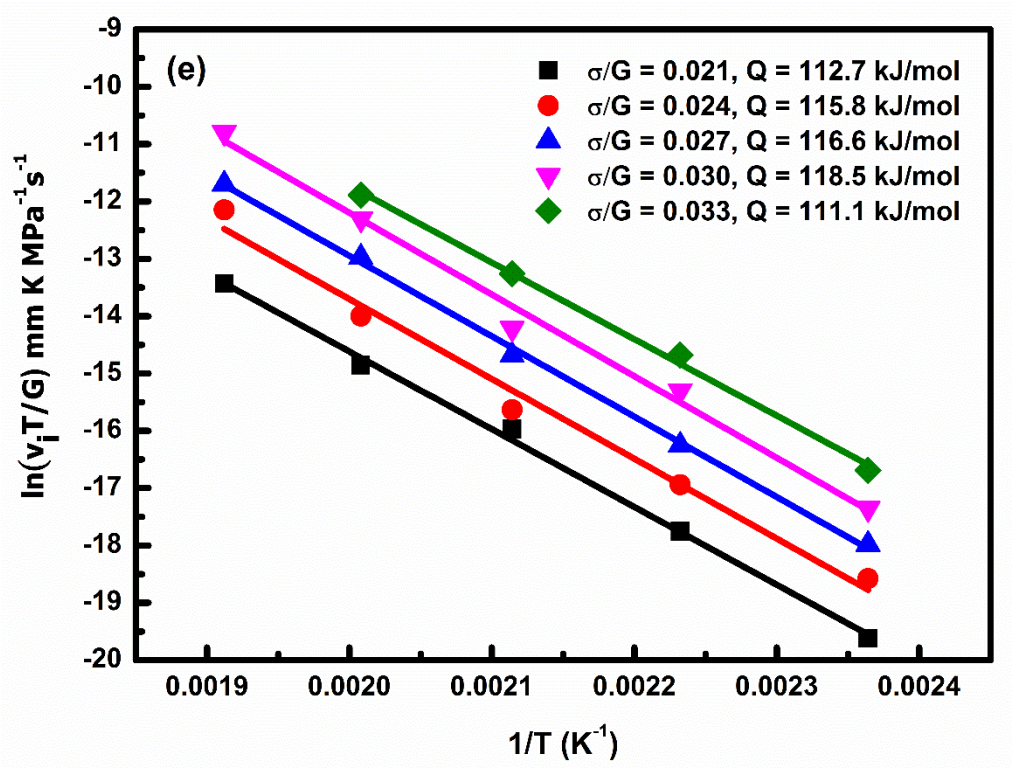

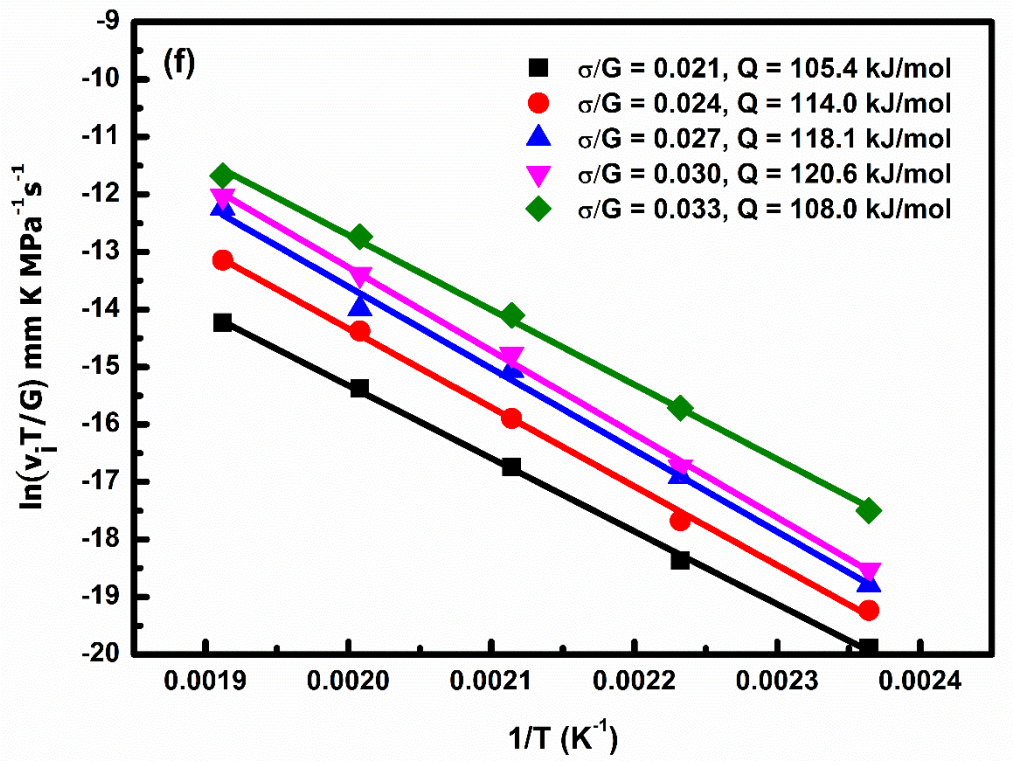

Fig. 6.8. Temperature dependence of the steady state impression velocities at different stresses for the (a) AZ91, (b) AZY911, (c) AZX911, (d) AZXY9110, (e) AZXY9111, and (f) AZXY9120 alloys.

The values of stress exponents in the present study were in the range of 5.3 to 6.0 for AZ91, 5.0 to 5.5 for AZY911, 4.3 to 6.5 for AZX911, 5.0 to 6.4 for AZXY9110, 5.5 to 6.3 for AZXY9111 and 4.6 to 6.3 for AZXY9120 alloys. Thus, the n values lie in the range of 4 to 7. The values of activation energies for the AZ91, AZY911, AZX911, AZXY9110, AZXY9111 and AZXY9120 alloys were 112.1±5.4, 112.6±2.9, 111.9±1.1, 112.4±2.4, 114.9±3.0 and 113.2±6.5 kJ/mol, respectively. The values of activation energies were in the range from 92 to 135 kJ/mol i.e. in between the activation energies required for pipe diffusion and lattice self-diffusion of Mg. Therefore, it was concluded that the dominant creep mechanism for all the alloys at the temperature and stress levels employed were dislocation creep controlled by pipe diffusion. Kabirian et al. [112] and Somekawa et al. [185] reported from their models that pipe diffusion in the AZ91 alloy changed to lattice self-diffusion at activation energies of 120 and 113 kJ/mol, respectively. In the present study, activation energies for all the alloys were in the range of 111.9±1.1 to 114.9±3.0 kJ/mol. Therefore, pipe diffusion likely changed to lattice self-diffusion.

6.3 Examination of microstructure after creep tests

To further interpret creep behaviour of the alloys, a detailed microstructural analysis of the creep tested specimens was carried out. The microstructures of all the alloys creep tested at 473 K, and 390 MPa are shown in Fig. 6.9(a-f). These microstructures essentially consist of the deformation zones underneath the punch and were obtained after bisecting the specimens along diagonal of the impressions. Three zones were recognized in the deformed microstructure below the punch in each tested specimen and were marked as zone ‘a’, zone ‘b’ and zone ‘c’. The extent of first two zones was dependent on the stability of the second phases present in the alloys and resistance provided by them against applied load. The stress field generated by the impressed cylindrical punch on the flat surface of the specimen was similar to Hertzian stress field. The contact pressure distribution by a cylindrical punch on flat surface of a specimen is given by [186],

$$\frac{\sigma_z}{P_m} = -\frac{1}{2}\left(1 - \frac{r^2}{R^2}\right)^{-1/2} \qquad 6.9$$

where, σ_z is normal surface stress, P_m is mean contact pressure, r is the distance from the punch centre and R is punch radius. σ_z is minimum when r = 0 i.e. at the centre of contact,

and it is equal to -0.5 P_m ('-' denotes compression). However, σ_z approaches infinity when r = R, i.e., at the edge. Outside the punch, $\sigma_z = 0$ along the surface. At immediate beneath the punch, at the centre i.e., at zone 'a', stress experienced was low and accordingly, it created a hemispherical dead zone with minimal microstructural changes. The characteristic was similar to the trait observed under applied hydrostatic pressure. In zone 'b', extensive shear deformation took place owing to the presence of very high stress at the edge. To accommodate it second phases were fragmented into small pieces and aligned towards the direction of material flow. Outside these two zones, i.e., in zone 'c', no significant deformation was observed. Further, zone 'b' exhibited different characteristics in different alloys. The AZ91 alloy exhibited substantial disintegration and elongation of the β-$Mg_{17}Al_{12}$ phase along the direction of material flow. Apart from fragmentation of β-$Mg_{17}Al_{12}$ phase, some refined particles of it were also observed in the microstructure near the punch edge, as observed in the magnified image shown in Fig. 6.9(a). These fine particles of β-$Mg_{17}Al_{12}$ phase precipitated out heterogeneously from the supersaturated α-Mg due to exposure at elevated temperature during creep test. Similar microstructural features, i.e., fragmentation and elongation of β-$Mg_{17}Al_{12}$ phase were also observed in both the AZY911 and AZXY9111 alloys, however, the extent was relatively less as compared to the AZ91 alloy. In the AZY911 alloy, thermally stable Mg_3Sb_2 particle provided grain boundary pinning effect and was broken into small pieces due to its higher brittleness. On the other hand, the microstructural changes in the AZXY9111 alloy were less severe compared to the AZY911 alloy due to the presence of Ca in the former alloy. The AZXY9120 alloy exhibited completely different morphology. It consisted a dense network of lamellar Al_2Ca phase along grain boundaries with very small amount of β-$Mg_{17}Al_{12}$ phase. Deformation zone in the microstructure of the AZXY9120 alloy was confined to a very narrow region. In addition, the amount of heterogeneously nucleated β-$Mg_{17}Al_{12}$ phase particles were less, as revealed in the magnified image shown in Fig. 6.9(f). In contrast, Al_2Ca phase preserved its continuity and slightly aligned in the flow direction. As the Ca content from 2.0 in the AZXY9120 alloy was reduced to 1.0 (wt.%) in the AZX911 and AZXY9110 alloys, the network of Al_2Ca phase suppressed and a considerable amount of β-$Mg_{17}Al_{12}$ phase formed. Accordingly, deformation zone encompassed bigger area than that in the AZXY9120 alloy and the β-$Mg_{17}Al_{12}$ phase aligned in the flow direction. Thus, the dense lamellar network of the thermally stable Al_2Ca phase sustained higher stresses without compromising its integrity and provided better creep resistance to the Ca containing alloys.

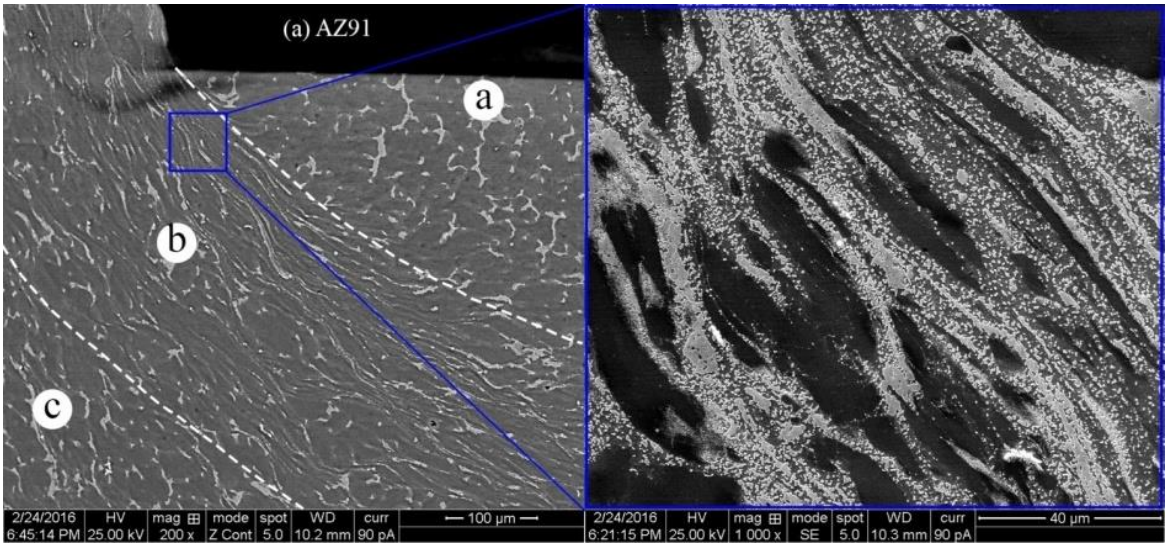
(a) AZ91
a
b
c
2/24/2016 6:45:14 PM HV 25.00 kV mag 200 x mode Z Cont spot 5.0 WD 10.2 mm curr 90 pA 100 µm
2/24/2016 6:21:15 PM HV 25.00 kV mag 1 000 x mode SE spot 5.0 WD 10.3 mm curr 90 pA 40 µm

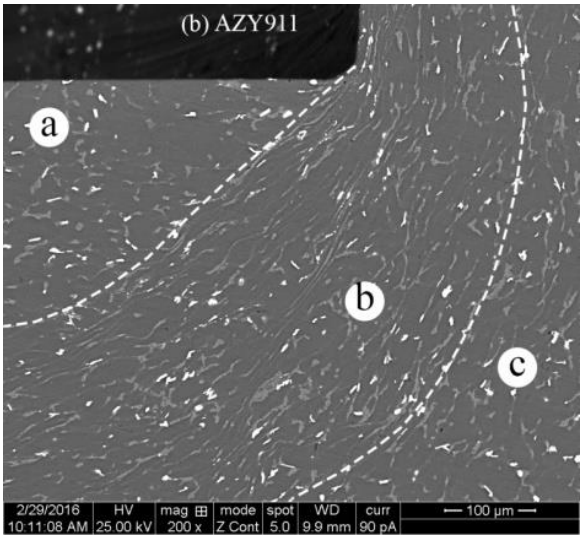
(b) AZY911
a
b
c
2/29/2016 10:11:08 AM HV 25.00 kV mag 200 x mode Z Cont spot 5.0 WD 9.9 mm curr 90 pA 100 µm

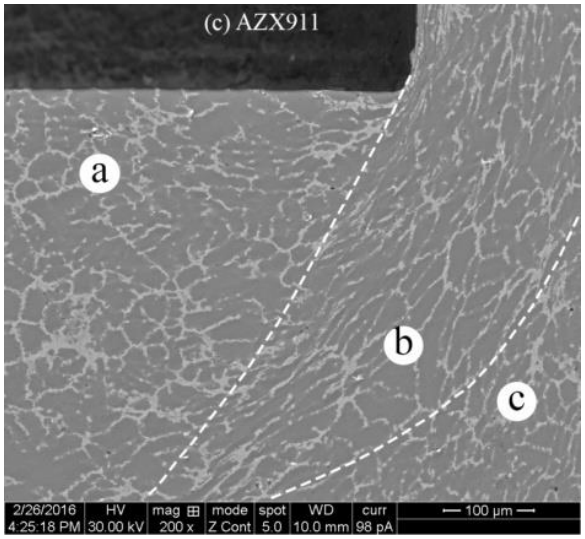
(c) AZX911
a
b
c
2/26/2016 4:25:18 PM HV 30.00 kV mag 200 x mode Z Cont spot 5.0 WD 10.0 mm curr 98 pA 100 µm

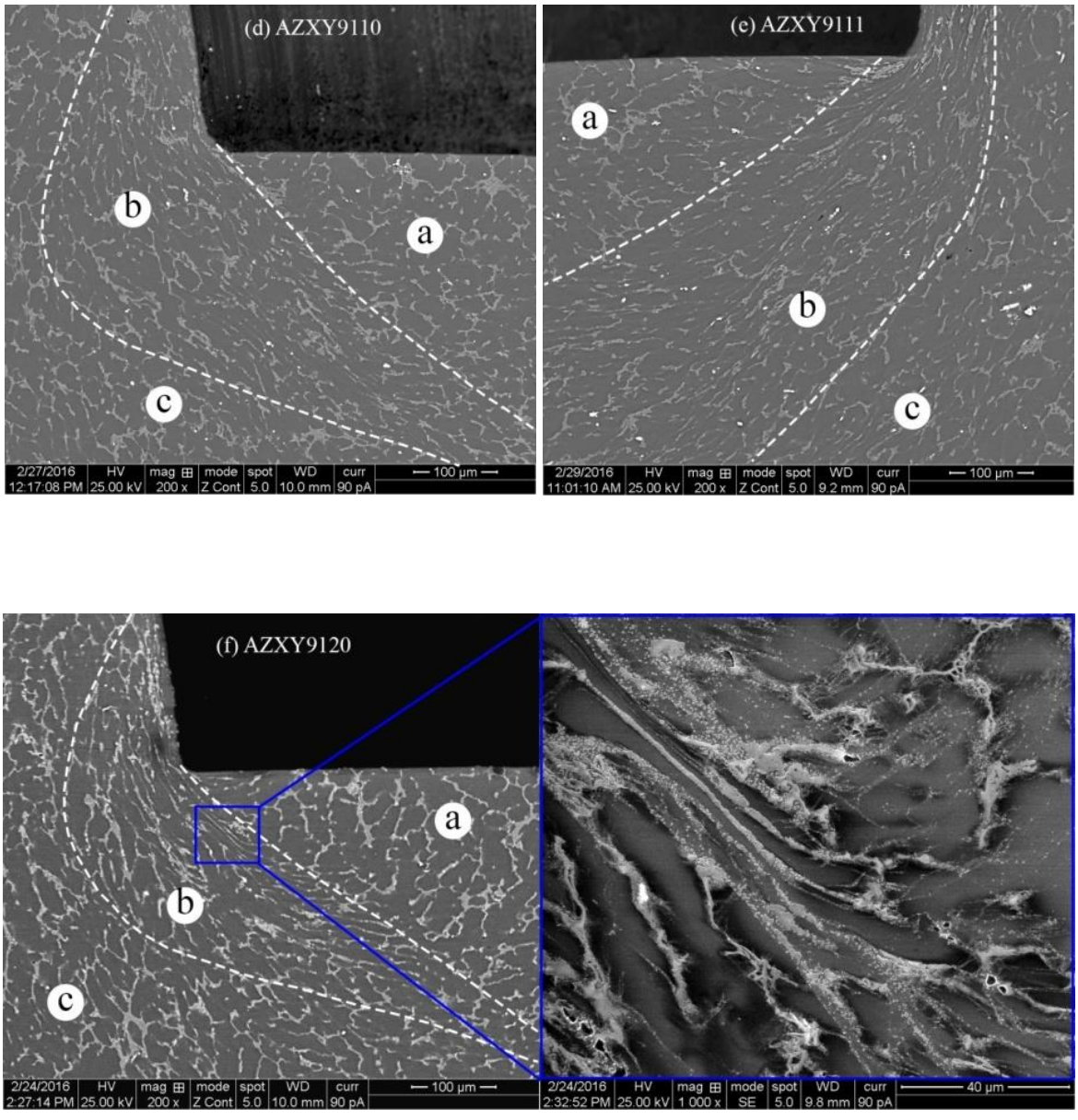

Fig. 6.9. SEM micrographs (in BSE mode) showing deformation patterns under the punch for the (a) AZ91 (with magnified view in SE mode), (b) AZY911, (c) AZX911, (d) AZXY9110, (e) AZXY9111, and (f) AZXY9120 (with magnified view in SE mode) alloys creep tested at 473 K and 390 MPa.

6.4 Verification of impression creep results by compressive creep

The observed trend in creep rates with respect to the individual and combined additions of Ca and Sb in the AZ91 alloy was further confirmed by carrying out conventional compressive creep tests on all the alloys. The typical compressive creep curves (strain vs. time) obtained at a temperature of 473 K and stress of 70 MPa for all the alloys are shown in Fig. 6.10(a). The variation of strain rate (creep rate) with time corresponding to Fig. 6.10(a) is shown in Fig. 6.10(b). The creep rates calculated from the secondary stages of the curves in Fig. 6.10(b) are shown in Fig. 6.10(c). It is evident that individual addition of Ca was better than the Sb addition. Among the modified alloys the AZXY9120 containing 2.0Ca and 0.3Sb (wt.%) exhibited the best creep resistance at the temperature and stress levels employed. Further increase in Sb content from 0.3 to 0.6 (wt.%) in the AZXY9111 alloy decreased its creep resistance, and it was inferior to that of the alloy pertaining individual addition of Ca, i.e., AZX911. The creep rate of the AZXY9110 alloy containing 1.0Ca and 0.3Sb (wt.%) was superior to that of the AZXY9111 alloy and inferior to that of the AZXY9120 alloy. The trend in creep rates with respect to alloying additions to the AZ91 alloy observed in the present investigation for both impression and compression creep are shown in Fig. 6.11. It is obvious that the trend in creep rates, i.e., impression velocities in impression creep, and strain rates in compression creep obtained with respect to the individual and combined additions of Ca and Sb to the AZ91 alloy was the same.

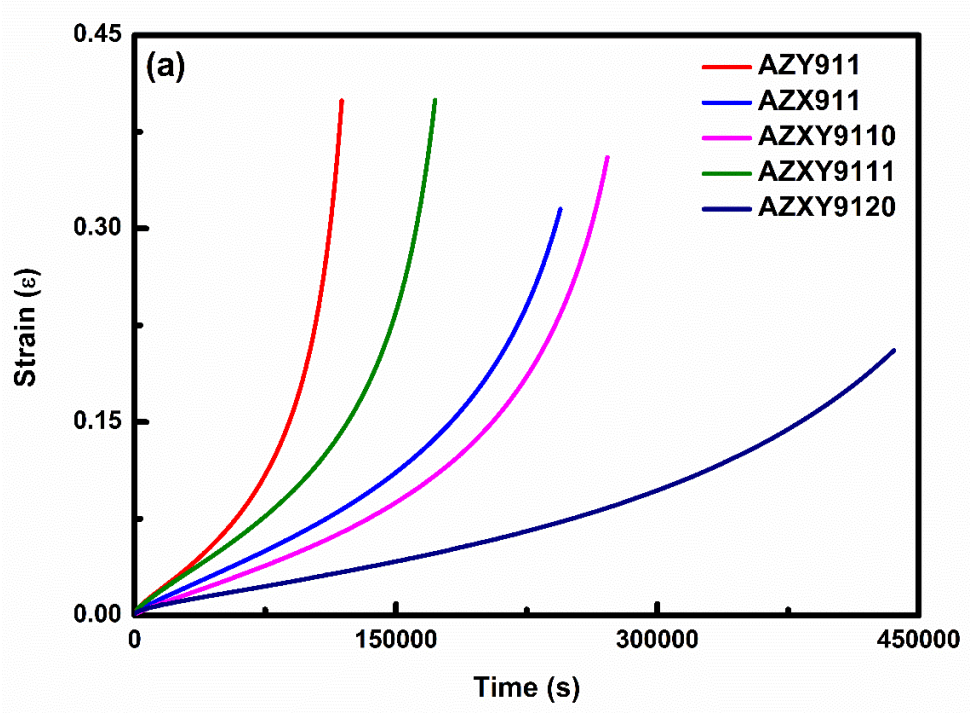
(a)
AZY911
AZX911
AZXY9110
AZXY9111
AZXY9120
Strain (ε)
0.45
0.30
0.15
0.00
0
150000
300000
450000
Time (s)

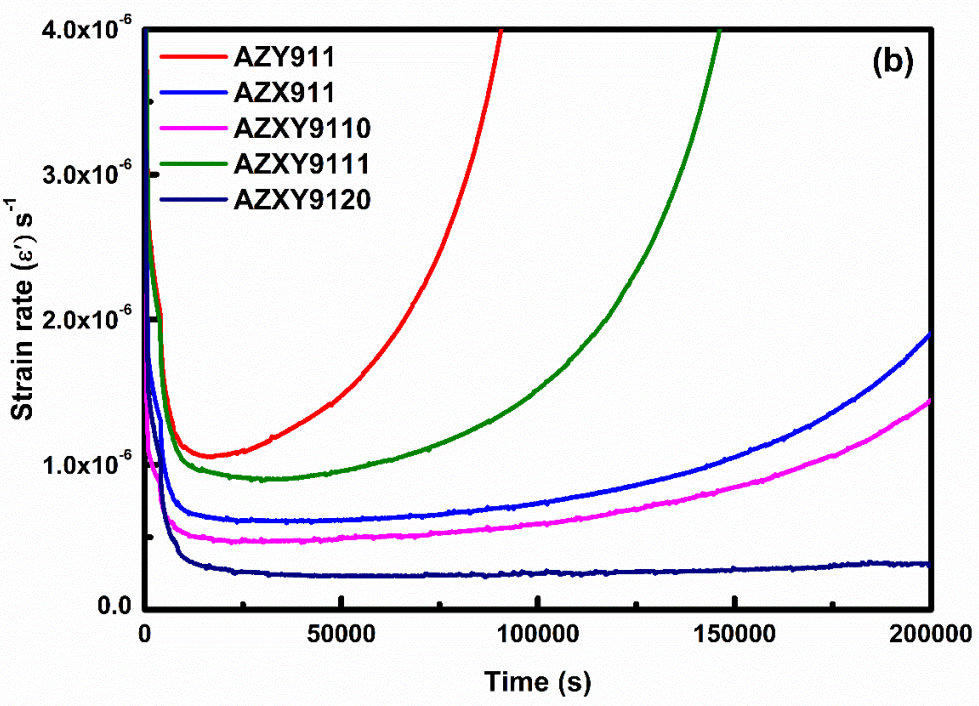
(b)
AZY911
AZX911
AZXY9110
AZXY9111
AZXY9120
Strain rate (ε') s-1
4.0x10-6
3.0x10-6
2.0x10-6
1.0x10-6
0.0
0
50000
100000
150000
200000
Time (s)

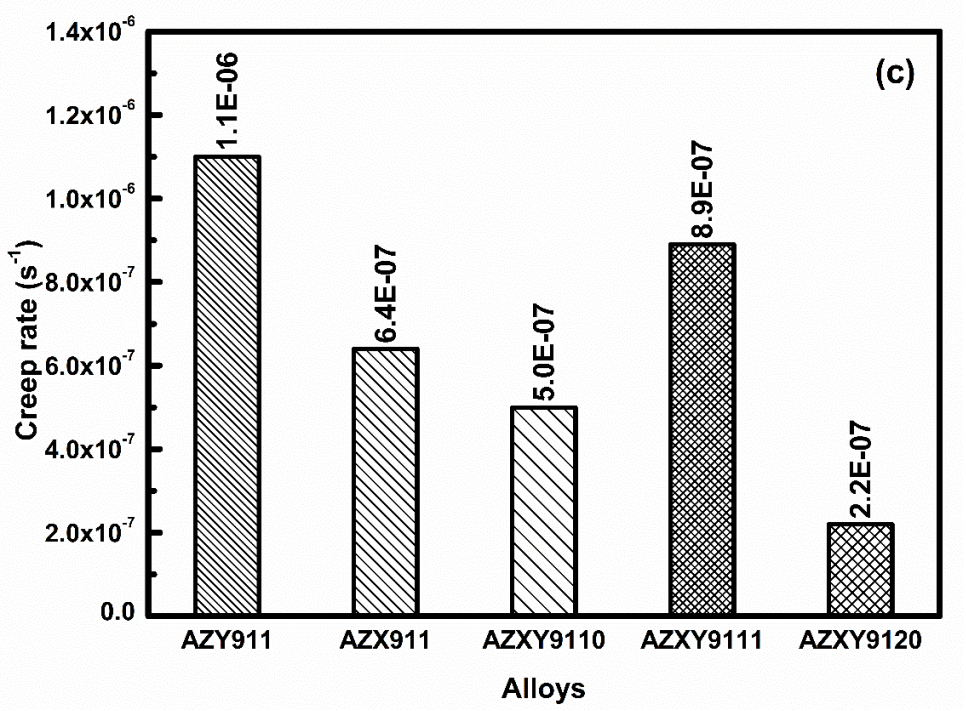

Fig. 6.10. (a) Typical compressive creep (strain vs. time) curves for all the alloys tested at temperature of 473 K and 70 MPa stress, (b) variation of strain rate vs. time corresponding to (a), and (c) summary of compression creep rates.

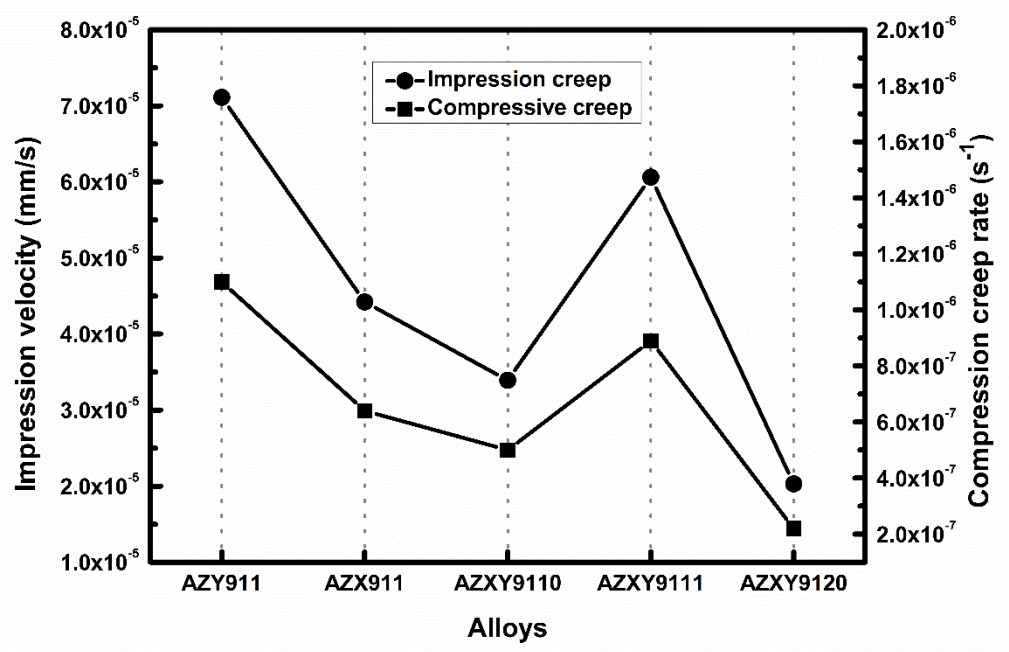

Fig. 6.11. The trend in creep rates with respect to the individual and combined additions of Ca and Sb to the AZ91 alloy observed in both impression and compression creep.

6.5 Summary of chapter 6

Impression creep behaviour of the squeeze-cast Ca and/or Sb added AZ91 Mg alloy was investigated in the temperature range of 423 to 523 K and stress level of 300 to 480 MPa. The outcomes of the study are enlisted.

i. Impression creep behaviour of the AZ91 alloy enhanced significantly by the additions of Ca and/or Sb. The improvement was more pronounced by combined additions (except AZXY9111) than the individual additions. The individual addition of Ca was superior to the Sb addition.

ii. The improvement was attributed to the presence of thermally stable Al_2Ca in the AZX911 alloy, Mg_3Sb_2 in the AZY911 alloy and both Al_2Ca as well as Ca_2Sb in the AZXY9110, AZXY9111, and AZXY9120 alloys in addition to the reduced β-$Mg_{17}Al_{12}$ phase. The Al_2Ca phase was more effective in improving creep resistance than the Mg_3Sb_2 phase.

iii. Among the modified alloys, the AZXY9120 alloy exhibited the best creep resistance at the temperature and stress levels employed owing to the presence of highest amount of dense network of lamellar Al_2Ca phase and least content of β-$Mg_{17}Al_{12}$ phase at grain boundaries.

iv. The values of stress exponents and activation energies were in the range of 4.3 to 6.4 and 111.9±1.1 to 114.9±3.0 kJ/mol, which suggested dislocation climb aided by pipe diffusion was the governing creep mechanism for all the alloys at the temperature and stress range employed.

v. Microstructural observation of the creep tested specimens revealed that the β-$Mg_{17}Al_{12}$ phase in the AZ91 alloy was severely fragmented and aligned in the direction of material flow, which deteriorated its creep resistance. In contrast, the dense lamellar network of the Al_2Ca phase in the AZXY9120 alloy sustained high stresses at elevated temperature without compromising its structural integrity, which resulted in its superior creep resistance.

vi. The observed trend in creep rates with respect to the individual and combined additions of Ca and Sb in the AZ91 alloy was further confirmed by carrying out conventional compressive creep tests on all the alloys.

Chapter 7

Corrosion behaviour

In an adverse working environment, suitability of a metal and alloy for a particular application can be estimated by its corrosion behaviour. The current chapter deals with the corrosion performance of modified AZ91 based alloys in an aqueous NaCl solution. Electrochemical cell performance is imitated through a suitable electrical equivalent circuit, which is in close agreement with the experimental data. An overview of post corrosion microstructure and its connection with the respective corrosion rate was also discussed in detail.

7.1 Nature of corrosion response

7.1.1 Open circuit potential

Fig. 7.1(a) shows the variation of OCP with time for all the AZ91-based alloys. It is evident from the figure that following a short transient period, the OCP values became almost stable. Initially, the electrode potential of almost all the alloys increased, which implies growth of surface films with the progress of corrosion [187,188]. The slight variation in potential indicated that the surface films were attacked by the chloride ions (Cl^-) present in the aqueous NaCl solution and then it was passivated by the presence of corrosion products. It might also be owing to the hydrogen evolution from the exposed surface to corrosive media. Finally, the electrode potential became stable, which suggests the attainment of steady state. Under steady state, a dynamic equilibrium is achieved between the corrosion products deposited at the surfaces and its dissolution owing to progressive corrosion. The steady state potential is referred as OCP. Further, the longer time of immersion did not alter the steady state potential of the alloys significantly.

The values of final stable OCP for all the alloys calculated from Fig. 7.1(a) are shown in Fig. 7.1(b). There is an obvious change in the OCP values owing to the additions of alloying elements to the AZ91 alloy.

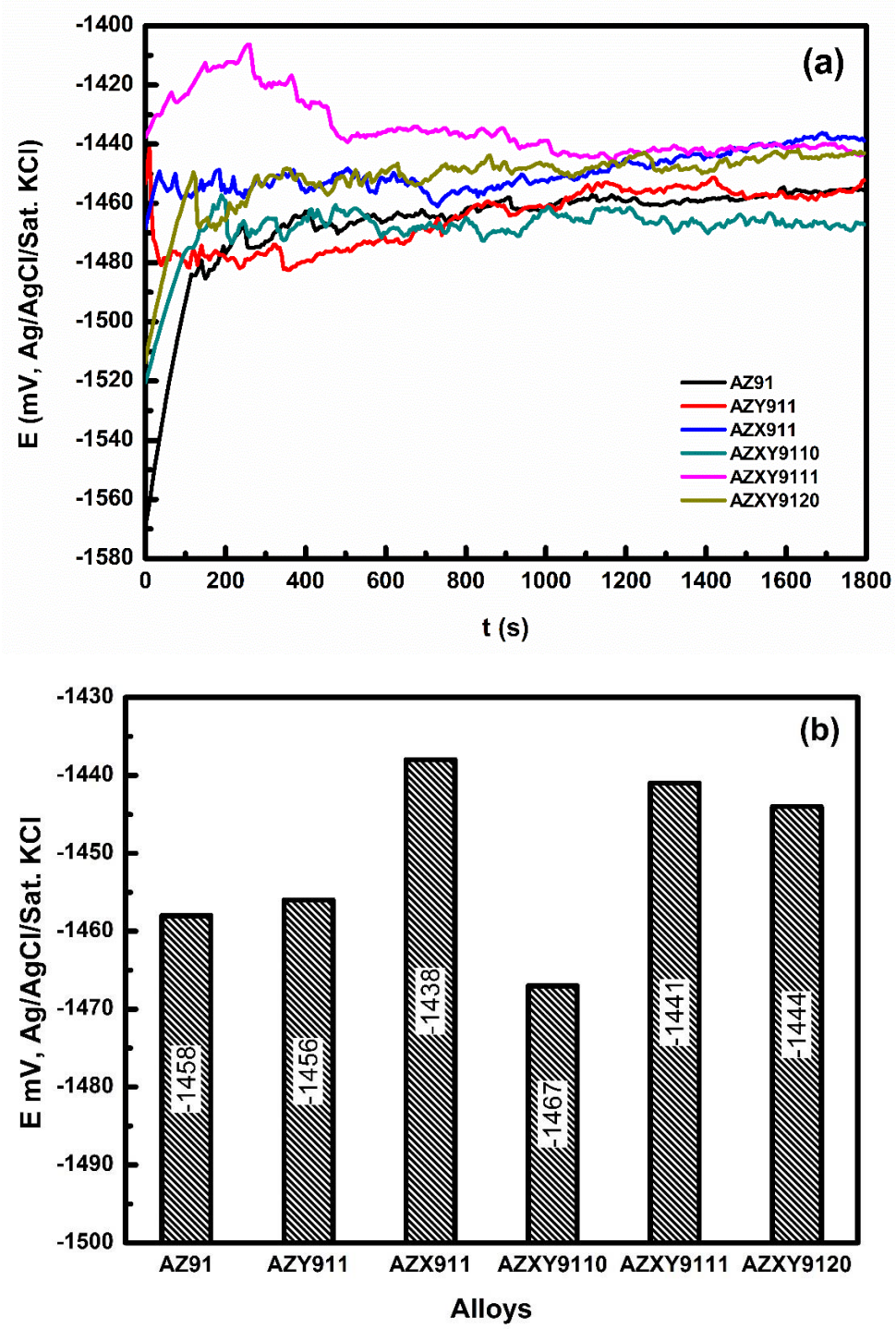

Fig. 7.1. (a) Variation of open circuit potential (OCP) with time, (b) values of final stable OCP calculated from (a) for all the alloys.

The alloying additions shifted the OCP towards more noble values except for the AZXY9110 alloy. For the AZXY9110 and AZX911 alloys, the final stable potential values of -1467 mV and -1438 mV were recorded, respectively. Therefore, the maximum shift in OCP values for the modified alloys was +29 mV only. However, there was not much variation of corrosion potentials among the alloys employed. Further, no specific trend was observed in the OCP values with respect to the Ca and Sb contents. The individual addition of Ca was better than that of the individual addition of Sb. The AZX911 alloy containing Ca exhibited the noblest OCP value among the alloys employed.

7.1.2 Nyquist and Bode plot analysis

Electrochemical impedance response of all the alloys was recorded periodically over 12 h. The Nyquist plots (NPs) as well as the corresponding Bode magnitude plots (BMPs), and Bode phase plots (BPPs) for all the alloys are shown in Fig. 7.2, 7.3, and 7.4, respectively. It is obvious from the figures that the impedance spectra contain three capacitive loops at low (LF), medium (MF) and high frequencies (HF). These loops were marked in Fig. 7.2(a) as loop 1, loop 2 and loop 3, respectively. In addition, an inductive loop at LF was also observed in all the alloys.

In order to explain the corrosion behaviour, an electrical equivalent circuit simulating the frequency dependent impedance response of all the alloys was proposed and shown in Fig. 7.5. The overall impedance of the circuit is as follows:

$$Z = Z_{R_S} + \frac{Z_{C_{DL}} Z_{R_{CT}}}{Z_{R_{CT}} + Z_{C_{DL}}} + \left(\frac{1}{Z_{CPE_F}} + \frac{1}{Z_{R_F} + \frac{Z_{R_1} Z_{CPE_1}}{Z_{R_1} + Z_{CPE_1}} + \frac{Z_{R_2} Z_L}{Z_{R_2} + Z_L}} \right)^{-1} \qquad 7.1$$

where Z is the overall impedance of the circuit, R_S is the solution resistance, R_{CT} is the charge transfer resistance, R_F is the film resistance, R_1 is the LF loop resistance for capacitive loop, R_2 is the LF loop resistance for inductive loop, C_{DL} is the electrical double layer capacitance, CPE_F is the constant phase element of the film, CPE_1 is the constant phase element of the capacitive loop observed at LF, and L is the inductance of the LF loop.

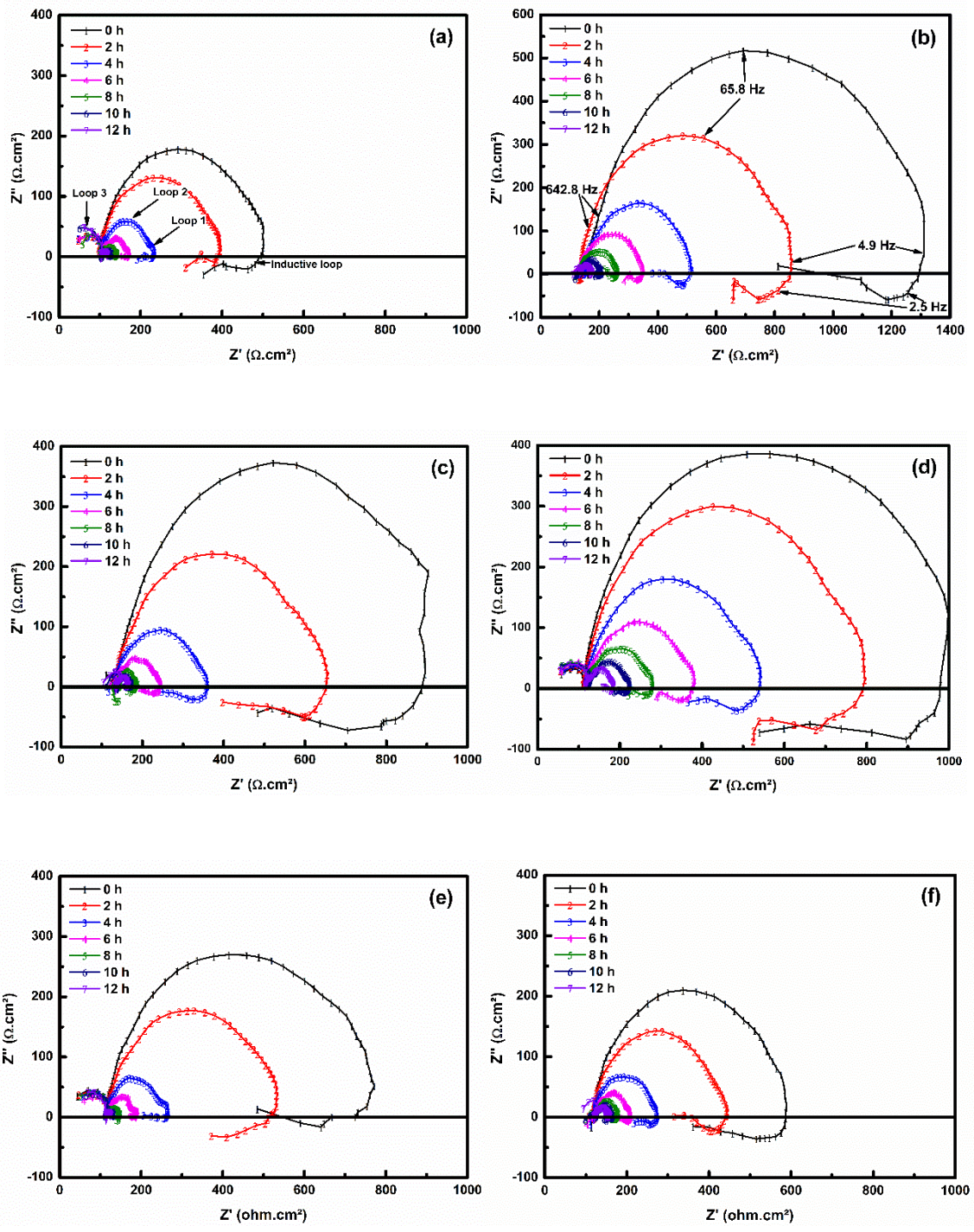

Fig. 7.2. Nyquist plots for the (a) AZ91, (b) AZY911, (c) AZX911, (d) AZXY9110, (e) AZXY9111 and (f) AZXY9120 alloys.

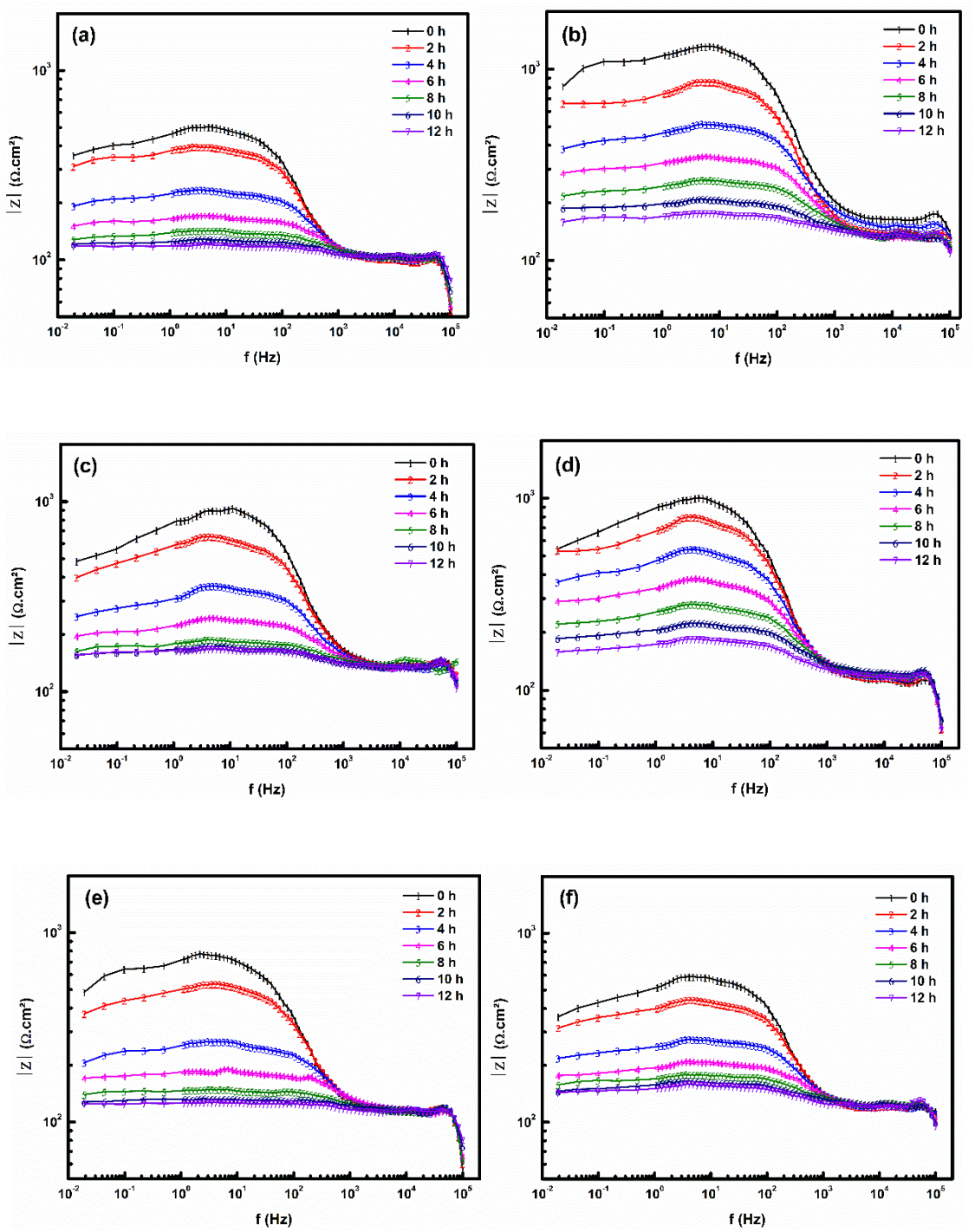

Fig. 7.3. Frequency vs. impedance Bode plots for the (a) AZ91, (b) AZY911, (c) AZX911, (d) AZXY9110, (e) AZXY9111 and (f) AZXY9120 alloys.

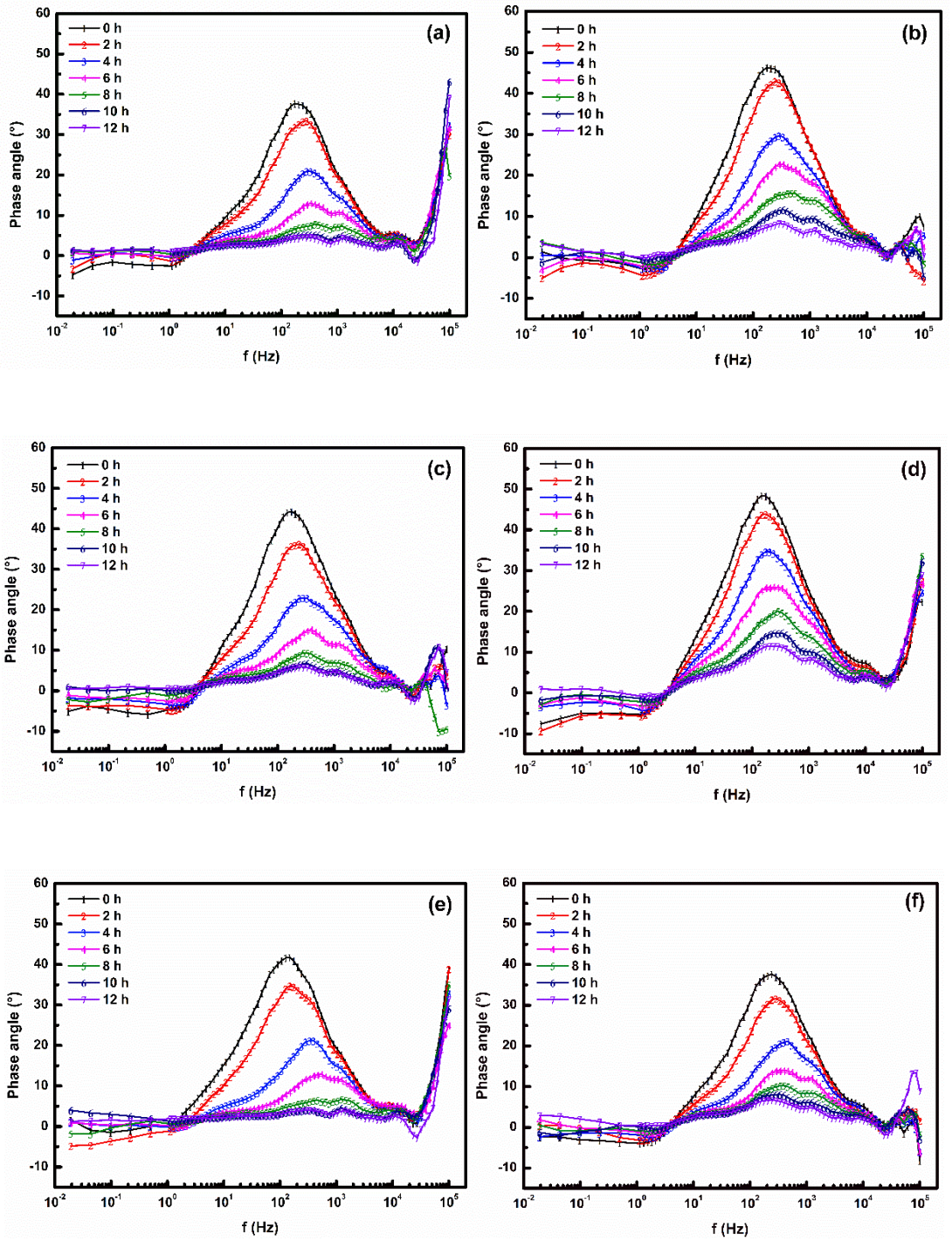

Fig. 7.4. Frequency vs. phase angle Bode plots for the (a) AZ91, (b) AZY911, (c) AZX911, (d) AZXY9110, (e) AZXY9111 and (f) AZXY9120 alloys.

Since the NPs of all the alloys exhibit depressed semicircles, constant phase elements (CPE) were considered instead of ideal capacitors for the loops at LF and MF, which provided consistency over the frequency range employed. The impedance of CPE is related to the characteristics of surface and electroactive species, and is expressed as [189,190]:

$$Z_{CPE} = \frac{1}{P(j\omega)^n} \qquad 7.2$$

Where $j = \sqrt{-1}$, P and n are empirical parameters, n=1, 0, -1 corresponds to pure capacitive, resistive and inductive behaviour exhibited by ideal flat surface, respectively, whereas, n=0.5 represents the capacitive behaviour of porous electrode [191]. The results indicated that the capacitance CPE_F is higher than CPE_1 for initial run. This is because CPE_F represents the capacitance of barrier film at corroded sites and CPE_1 is the protected non-degraded zone at the electrode surface. The values of R_{CT} and R_F decreased with increase in immersion time, which indicated reduced stability of the surface film.

Polarization resistance (R_P) was not determined directly from the diameter of the semi-circle of the NP owing to the presence of multiple RC loops. The same was calculated from the equivalent circuit since assumption of simple Randel circuit model overestimates it, resulting in an underestimation of corrosion rate [192]. The various parameters calculated based on the equivalent circuit is presented in Table 7.1 for all the alloys.

The RC loop at HF (i.e., loop 3) is attributed to the charge transfer resistance and the double layer capacitance of the outermost porous layer of the surface film. The RC loop at MF (i.e., loop 2) is related to the oxide layer formed by the presence of the additives, and it acted as a barrier layer. The RC loop (i.e., loop 1) at LF is related to the deposition on β-$Mg_{17}Al_{12}$ phase. The appearance of LF inductive loop is attributed to the relaxation of intermediate species like Mg^+ and $Mg(OH)^+$ adsorbed at the specimen surfaces. The capacitive and inductive loops observed at LF originated because of the localized corrosion attack on the surface of the specimens. The RC loops present at LF and MF in the NPs were also observed in the BPPs shown in Fig. 7.4 and became prominent as the immersion time increased.

Table 7.1: Summary of various parameters calculated from the proposed equivalent circuit.

Alloy Designation	**C_{DL} ($F.cm^{-2}$)**	**R_S ($\Omega.cm^2$)**	**R_{CT} ($\Omega.cm^2$)**	**R_F ($\Omega.cm^2$)**	**R_1 ($\Omega.cm^2$)**	**R_2 ($\Omega.cm^2$)**	**CPE_F**		**CPE_1**		**L(H/cm^2)**
							P_1	**n_1**	**P_2**	**n_2**	
AZ91	5.92E-02	30	72	200	130	85	9.91E-05	0.91	1.19E-05	0.95	75
AZY911	1.00E-02	30	130	510	420	267	9.86E-06	0.91	1.02E-06	0.72	50
AZX911	1.02E-02	30	110	480	139	155	1.90E-05	0.97	9.90E-06	0.99	80
AZXY9110	3.54E-02	30	82	495	205	188	1.90E-06	0.99	1.41E-05	0.88	80
AZXY9111	3.53E-02	30	85	300	200	200	3.09E-05	0.87	8.83E-05	0.33	40
AZXY9120	2.53E-03	30	90	230	150	110	5.97E-06	0.92	9.95E-05	0.55	80

BMPs of all the alloys shown in Fig. 7.3 revealed that the low frequency impedance decreased steadily and the break point frequencies for all the runs were almost same, which indicated a constant rate of hydrogen emission [193]. The horizontal parts of the BMPs were frequency independent and corresponded to a pure resistance. The linear slope of the BMPs in the negative direction is the characteristic of capacitive behaviour. The continuous decrease of impedance with a decrease in frequencies in the BMPs and the presence of trait of negative phase angles towards LF in the BPPs evidenced inductive behaviour (i.e., the current response lead applied potential). A similar behaviour was also reported by several other researchers as well [194–196]. The impedance spectra exhibited two RC loops that were almost merged initially, however, became prominent with an increase in immersion time.

The impedance spectra generated by regression fit using the equivalent circuit shown in Fig. 7.5. It is evident that the representative generated plot has excellent correlation with the obtained experimental data as shown in Fig. 7.6. The acquired experimental data of all the alloys can be fitted perfectly with the proposed equivalent circuit, and all the values of circuit elements for fitting purpose were enlisted in Table 7.1. No diffusion related phenomena was recognized in the obtained results, and therefore, diffusion processes were not considered in the model. A pictorial representation of the equivalent circuit corresponding to Fig. 7.5 is shown in Fig. 7.7.

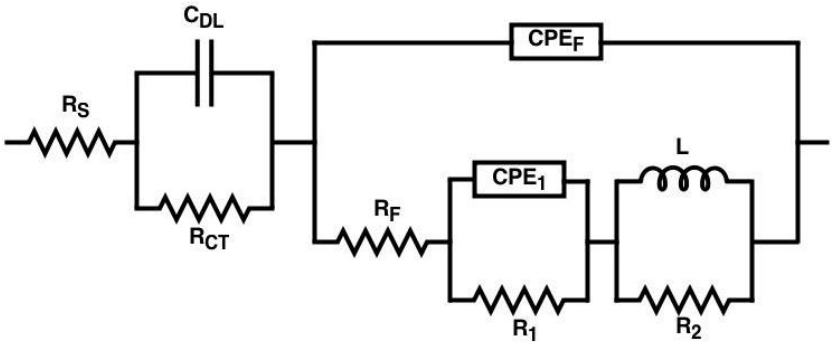

Fig. 7.5. Equivalent circuit corresponding to EIS response.

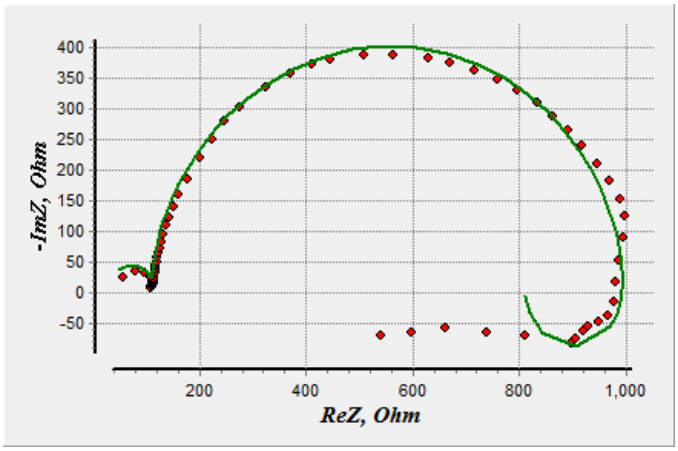

Fig. 7.6. Representative picture of model fitting with the obtained experimental data.

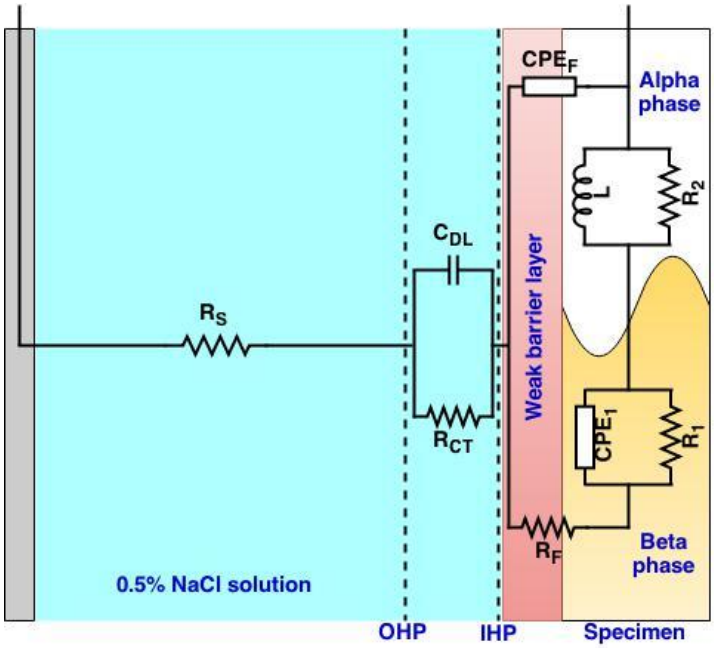

Fig. 7.7. Pictorial representation of corrosion behaviour of the Ca and Sb added AZ91 alloys.

EIS measurements confirmed the formation of a very weak protective film that degraded with increased immersion time due to localized corrosion attack. Active dissolution took place from the centre of α-Mg grain and the β-$Mg_{17}Al_{12}$, Al_2Ca phase, etc. acted as a partially protective phase.

7.2 Potentiodynamic polarization study

The results of potentiodynamic polarization scan carried out after the long term EIS measurements are shown in Fig. 7.8(a). The values of various parameters evaluated from the Tafel plots are included in Table 7.2. Fig. 7.8(b) shows the corrosion rates of all the alloys determined from Fig. 7.8(a). It is evident from Fig. 7.8(b) that the corrosion resistance increased considerably by the alloying additions. The base AZ91 alloy has the highest corrosion rate of 15.2 mm/y, and its polarization curve (Fig. 7.8(a)) suggests that there is less probability of quasi-passive film formation on the surface of the AZ91 alloy, which enhanced active dissolution of the alloy. The modified AZ91-based alloys revealed superior corrosion resistance than the base AZ91 alloy. The alloys comprising individual Ca and Sb additions exhibited better corrosion performance than that of the alloys having combined additions. However, the corrosion resistance of the AZX911 and AZY911 alloys was almost same, although, it was slightly better for the former alloy exhibiting a corrosion rate of 8.8 mm/y, which is about two times better than the base AZ91 alloy. Wu et al. [12] investigated corrosion behaviour of the AZ91 alloy with individual additions of Ca and REs. They also observed a reduced corrosion rate of the alloy with the individual additions of 1.0Ca (wt.%) and 1.0RE (wt.%) as compared to the base AZ91 alloy. Wang et al. [197] too observed the superior corrosion resistance of the heat-treated AZ91 alloy with 1.0Ca (wt.%) addition in their study. Among the alloys with mixed additions, the AZXY9120 and AZXY9111 alloys exhibited the highest and lowest corrosion resistance, respectively, with the AZXY9110 alloy exhibiting the corrosion resistance in-between. The addition of 0.3Sb (wt.%) to AZX911 alloy, i.e., the AZXY9110 alloy deteriorated the corrosion resistance by 30.7%. Further, as Sb content from 0.3 (wt.%) in the AZXY9110 alloy increased to 0.6 (wt.%) in the AZXY9111 alloy at constant Ca content (i.e., 1.0 wt.%), the corrosion resistance deteriorated by 5.8%. On the other hand, as the Ca content is increased from 1.0 (wt.%) in the AZXY9110 alloy to 2.0 (wt.%) in the AZXY9120 alloy at a constant Sb content (i.e., 0.3 wt.%), the corrosion resistance improved by 18.5%.

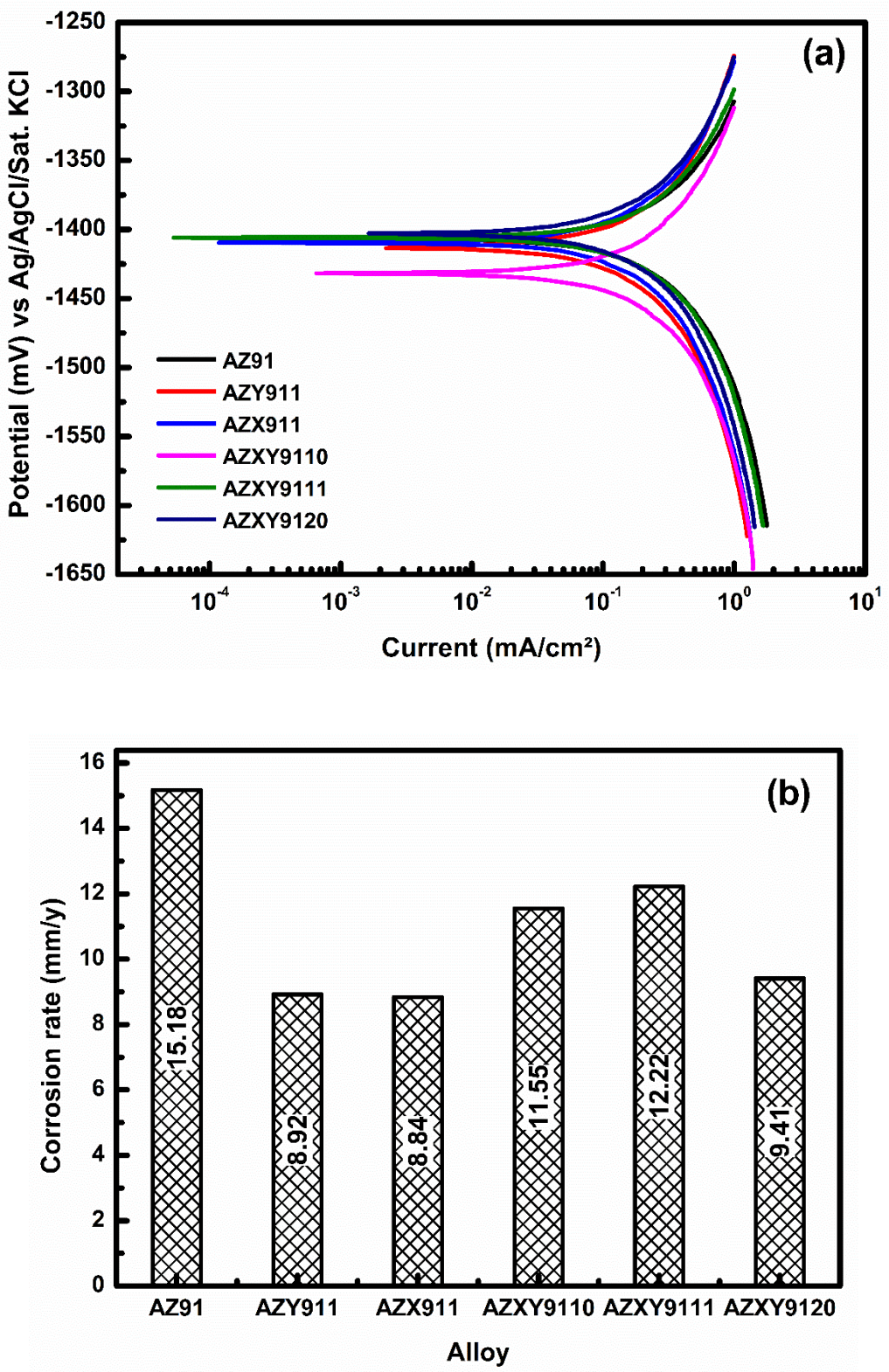

Fig. 7.8. (a) Potentiodynamic polarization curves for all the alloys and (b) corrosion rate of all the alloys.

Table 7.2: Summary of various parameters calculated from Tafel plots.

Alloy Designation	E_{corr} (mV) vs. Ag/AgCl/Sat. KCl	β_a (mV)	β_c (mV)	I_{corr} (mA/cm^2)	Corrosion Rate (mm/y)
AZ91	-1406.8	282.58	482.59	0.72	15.18
AZY911	-1413.6	303.91	394.23	0.49	8.92
AZX911	-1409.2	243.67	370.47	0.44	8.84
AZXY9110	-1432.2	295.89	445.2	0.58	11.55
AZXY9111	-1405.9	251.83	409.33	0.58	12.22
AZXY9120	-1402.7	277.37	370.08	0.50	9.41

Therefore, in the alloys comprising combined additions increased Ca content is beneficial, whereas, increased Sb content is detrimental for corrosion resistance.

7.3 Microstructural observation after corrosion test

Fig. 7.9(a-c) shows the corrosion film formed on the surfaces of the AZ91, AZX911 and AZXY9111 alloys following complete corrosion test. It is evident from Fig. 7.9(a) that the film on the surface of the base alloy was discontinuous and cracked. Thus, the poor corrosion resistance of the AZ91 alloy was attributed to the presence of irregular and cracked film. However, the extent of cracks observed on the surfaces of the AZX911 and AZXY9111 alloys were relatively less with the former alloy exhibited less cracks as compared to the later one. The whole surface of the AZX911 alloy was covered with a smooth and uniform corrosion film with a negligible presence of cracks on it. On the contrary, the surface of the AZXY9111 alloy shown as a representative picture for combined addition exhibited fine powdery appearance with a number of discontinuities, which allowed easy access of the electrolyte to its subsurface rendering the alloy more susceptible to corrosion.

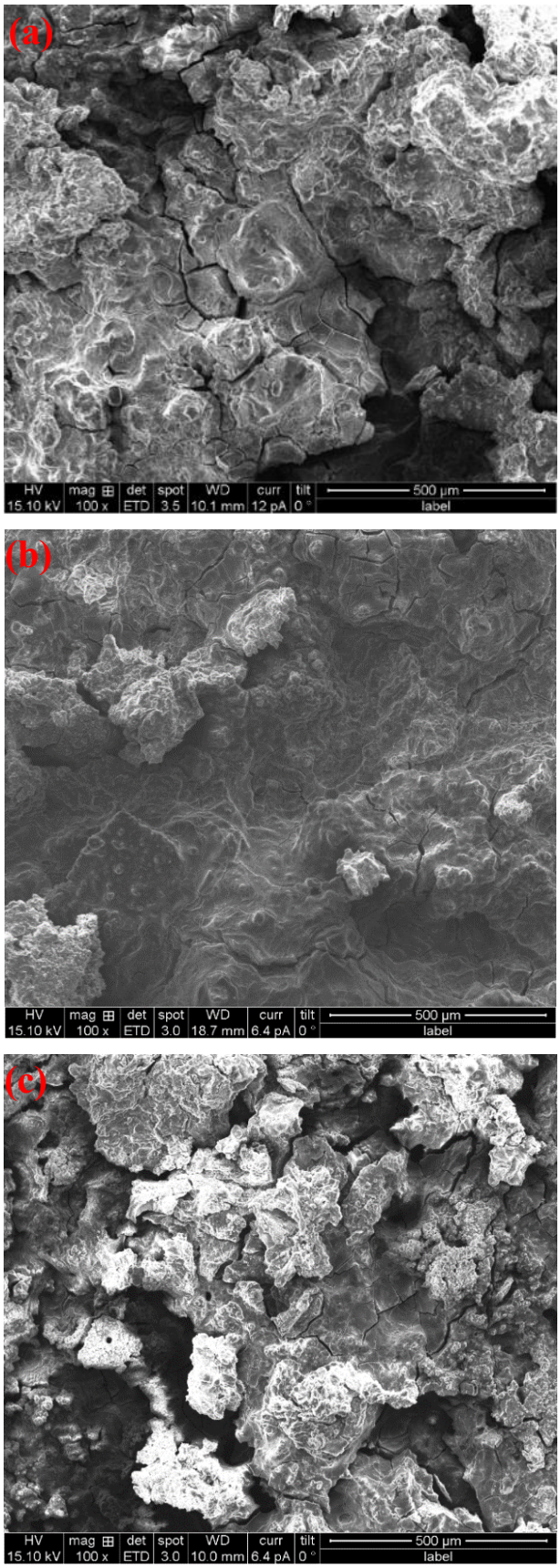

Fig. 7.9. SEM micrographs of corroded surfaces before removal of corrosion products for the (a) AZ91, (b) AZX911 and (c) AZXY9111 alloys.

Fig. 7.10 shows the XRD patterns obtained from the corrosion products developed on the surfaces of all the alloys. It is noticeable from the patterns that the corrosion product is mainly $Mg(OH)_2$. There was a considerable delay before conducting the XRD scan after completing the corrosion test. During this time gap, the $Mg(OH)_2$ might interact with the atmospheric CO_2 and converted it to carbonates. Further, CO_2 from environment dissolved in the electrolyte and resulted in the formation of carbonates as well as hydrated carbonates of Mg reacting with thermodynamically unstable $Mg(OH)_2$ as per the following reactions.

$$Mg(OH)_2 + CO_2 \rightarrow MgCO_3 + H_2O \quad 7.3$$

$$MgCO_3 + H_2O \rightarrow MgCO_3.3H_2O \quad 7.4$$

$$5MgCO_3.3H_2O \rightarrow 4MgCO_3.Mg(OH)_2.4H_2O + CO_2 + 10H_2O \quad 7.5$$

However, magnesium carbonate ($MgCO_3$) is often poorly crystalline and difficult to detect using XRD [198,199]. Therefore, FTIR absorption spectra were recorded at ambient temperature in open atmosphere in the mid-infrared region of 4000-400 cm^{-1} of the corrosion products formed at the specimen surfaces and shown in Fig. 7.11. It is evident that all the alloys exhibited a very distinct $(OH)^-$ peak at 3697 cm^{-1} confirming to brucite ($Mg(OH)_2$) as main corrosion product. Thus, the XRD results obtained from the corrosion products were confirmed by FTIR analysis as well. The peaks at 3643 and 3439 cm^{-1} were recognized as vibration bands corresponding to $(OH)^-$ and H_2O of the hydromagnesite ($Mg_5(CO_3)_4(OH)_2.4H_2O$). The sharp CO_3^{2-} asymmetric bending peak at 1641 cm^{-1} was attributed to the hydromagnesite as well. The stretch band of CO_3^{2-} observed at 1479-1392 cm^{-1} was probably due to the average of all the slightly different IR absorptions by small amount of magnesium carbonate, hydromagnesite, and nesquehonite ($MgCO_3.3H_2O$). The clear presence of nesquehonite ($MgCO_3.3H_2O$) was also identified by the asymmetric CO_3^{2-} peaks at 1529 and 846 cm^{-1} in the spectra of the AZXY9110 alloy. Thus, the hydromagnesite constituted a significant fraction of the corrosion products, and its formation took place upon prolong exposure of CO_2 containing environment and conversion of nesquehonite [198].

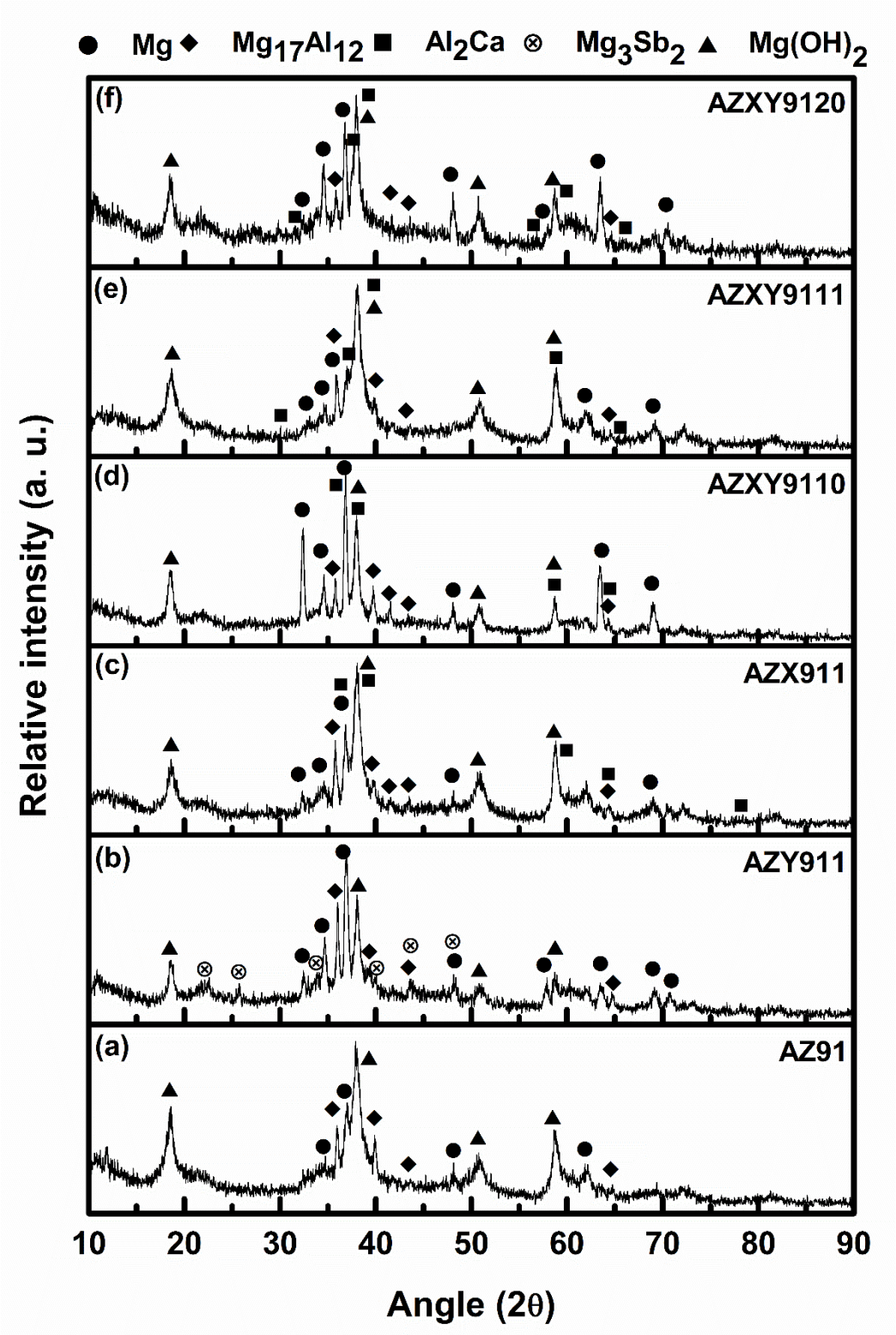

Fig. 7.10. XRD patterns obtained from the corroded surfaces of all the alloys.

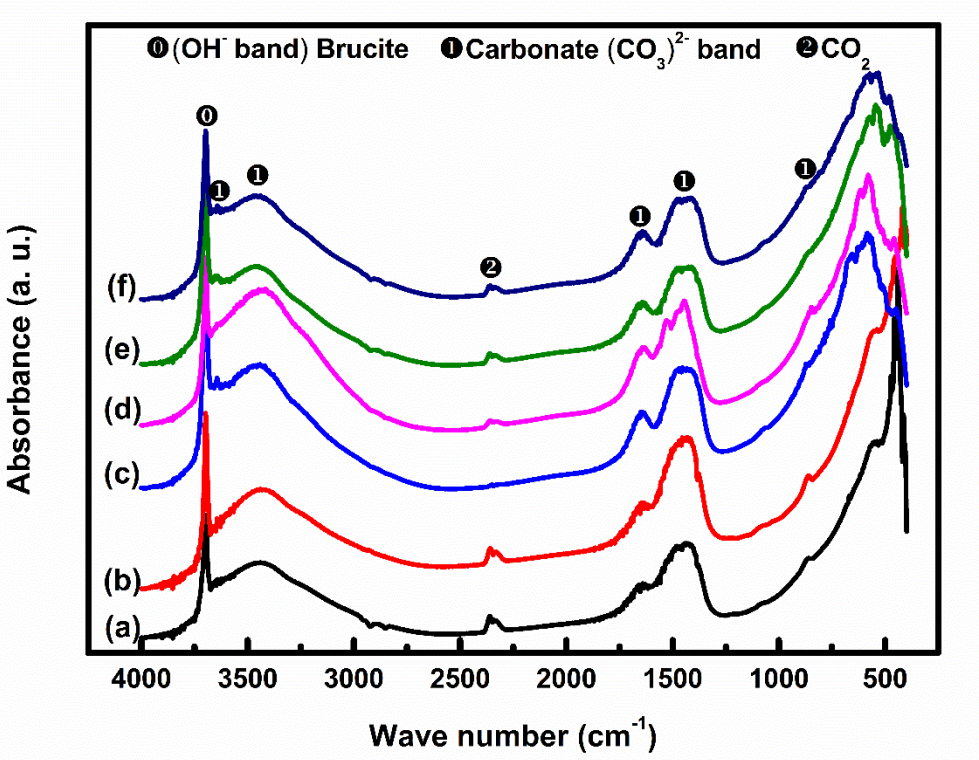

Fig. 7.11. FTIR patterns obtained from the corrosion products of all the alloys.

Fig. 7.12(a-c) illustrates the surfaces of the AZ91, AZX911 and AZXY9111 alloys after taking away of corrosion products. The intermetallic β-$Mg_{17}Al_{12}$ phase in the AZ91 alloy (Fig. 7.12(a)); both β-$Mg_{17}Al_{12}$ and Al_2Ca phases in the AZX911 and AZXY9111 alloys (Fig. 7.12(b and c)) were mainly visible along the GBs, which corroded less as compared to the α-Mg phase and remained as a kind of corrosion barrier. The Al_2Ca phase present with the β-$Mg_{17}Al_{12}$ phase on the corroded surfaces of the AZX911 and AZXY9111 alloys was not distinguishable (Fig. 7.12(b and c)) owing to their low Ca content i.e. 1.0 (wt.%). The SEM micrograph of the surface of the AZXY9120 alloy pertaining 2.0Ca (wt.%) after removal of corrosion products is shown in Fig. 7.12(d). It is obvious that the corroded surface of the AZXY9120 alloy revealed the distinct presence of the corrosion unaffected intermetallic Al_2Ca and β-$Mg_{17}Al_{12}$ phases. In order to further clarify the distribution of the alloying elements on the corroded surfaces, EPMA elemental mapping of the AZXY9120 alloy after removal of corrosion products was carried out and shown in Fig. 7.13 as a representative picture for all the alloys. The mapping clearly indicated that the region left after corrosion was enriched in Al and these regions were mostly intermetallic phases. The grain interiors with the lowest Al concentration were the most corrosion prone and removed completely by corrosion. Thus, the extent of corrosion attack decreased from the centre of the grains towards the GBs with an increase in Al concentration.

The as-cast microstructure of the AZ91 alloy mainly consists of α-Mg matrix phase and β-$Mg_{17}Al_{12}$ intermetallic phase. The β-$Mg_{17}Al_{12}$ phase is more corrosion resistant compared to α-Mg phase owing to its higher Al content. The β-$Mg_{17}Al_{12}$ phase plays a dual role in the AZ91 alloy. It acts as an effective barrier to corrosion, which is beneficial. In contrast, it also acts as an active cathode to the α-Mg matrix and thus, detrimental to corrosion resistance. However, the β-$Mg_{17}Al_{12}$ phase is beneficial for improving corrosion resistance when it acts as a barrier along the GBs. This is possible only when its volume fraction is reasonably high and forms a continuous network, which is generally observed in the die-cast alloys [200]. On the contrary, networking is not possible in the presence of coarse and discontinuous intermetallic phase, which was observed in the microstructure of the investigated squeeze-cast AZ91 alloy. Therefore, the beneficial effect of the presence of intermetallic phase was not observed in the AZ91 alloy. The intermetallic β-$Mg_{17}Al_{12}$ phase acted as an effective cathode and was undermined owing to the selective corrosion of the α-Mg matrix resulting in enhanced corrosion of the base AZ91 alloy.

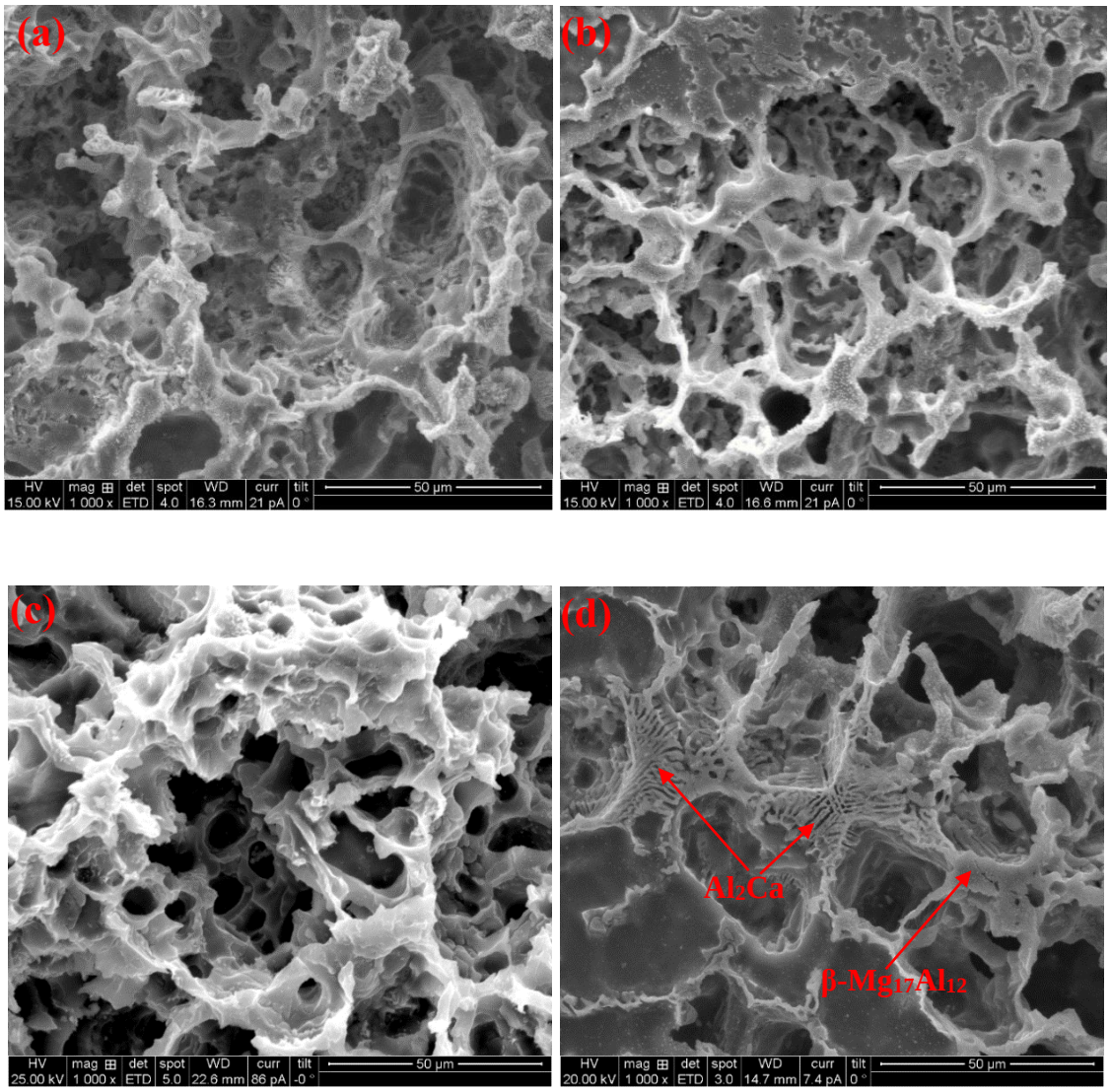

Fig. 7.12. SEM micrographs of corroded surfaces after removal of corrosion products for the (a) AZ91, (b) AZX911, (c) AZXY9111 and (d) AZXY9120 alloys.

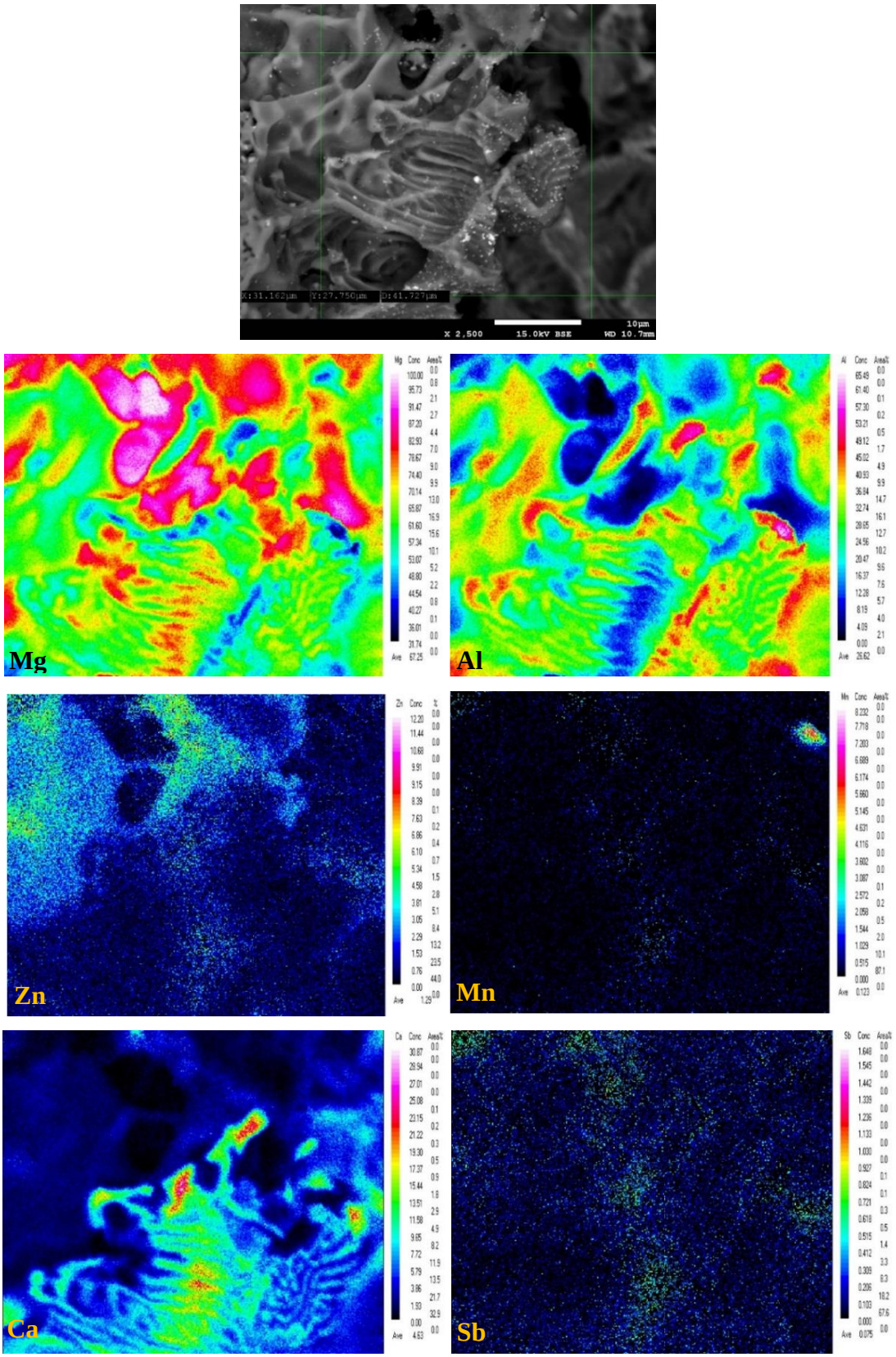

Fig. 7.13. EPMA elemental mapping taken from the AZXY9120 alloy after removal of corrosion product.

Both individual and combined additions of Ca and Sb to the AZ91 alloy reduced corrosion rate. All the alloying additions employed in the present investigation decreased as well as refined the β-$Mg_{17}Al_{12}$ phase and formed Al_2Ca or needle-shaped Mg_3Sb_2 phases distributed mainly along GBs. Further, the alloying additions refined grains of the base AZ91 alloy. All the alloying additions greatly improved the corrosion resistance of the AZ91 alloy by decreasing its corrosion current. The beneficial effect of grain refinement on corrosion behaviour of Mg alloy was reported elsewhere [136,172]. The Al_2Ca and Mg_3Sb_2 intermetallic phases are less detrimental compared to the β-$Mg_{17}Al_{12}$ phase [157,197] and therefore, replacing the latter by either of the former reduced potential difference between the matrix and intermetallic, which improves corrosion resistance. Wang et al. [197] also indicated the lower galvanic potential difference between Ca-containing precipitate and α-Mg matrix. The lowest corrosion rate of the AZX911 alloy was attributed to the reduced volume fraction of the β-$Mg_{17}Al_{12}$ phase, the maximum grain refinement observed as well as the presence of reticular Al_2Ca phase along GBs acting as a barrier against corrosion. In contrast, the random distribution of the Mg_3Sb_2 phase in the AZY911 alloy failed to develop effective corrosion resistant barrier resulting its slightly lower corrosion resistance as compared to that of the AZX911 alloy. The corrosion resistance of the AZ91 alloys containing combined additions of Ca and Sb was superior as compared to that of the base AZ91 alloy, and it was inferior to that of the alloys containing individual additions. The amount of Ca_2Sb phase was the maximum in the AZXY9111 alloy and relatively less in the AZXY9110 and AZXY9120 alloys due to lower Sb content in them. The Ca_2Sb phase might act as an active cathode, although, the exact electrode potential of it is not known. Besides, the Ca_2Sb phase similar to the Mg_3Sb_2 phase was distributed randomly in the matrix and thus, not beneficial for corrosion resistance. Therefore, it is speculated that the lower corrosion resistance of the AZXY9111 alloy as compared to that of the AZXY9110 alloy was attributed to the presence of higher amount of Ca_2Sb phase. On the other hand, the AZXY9120 alloy exhibited improved corrosion resistance as compared to that of the AZXY9110 alloy owing to the presence of relatively higher and lower amount of Al_2Ca and Ca_2Sb phases, respectively.

7.4 Summary of chapter 7

The effect of individual and combined additions of Ca and Sb on corrosion behaviour of the squeeze-cast AZ91 alloy is investigated. The following conclusions are drawn:

i. The alloying additions shifted the OCP towards more noble values except for the AZXY9110 alloy. There was not much variation of corrosion potentials among the alloys employed, and no specific trend was observed in the OCP values with respect to Ca and Sb contents.

ii. EIS measurements confirmed the formation of a very weak protective film that degraded with increased immersion time due to localized corrosion attack. Active dissolution took place from the centre of α-Mg grain, and the β-$Mg_{17}Al_{12}$ phase acted as a partially protective phase.

iii. Corrosion resistance of the AZ91 alloy was the lowest, and it was better for all the modified alloys owing to the refined and reduced amount of β-$Mg_{17}Al_{12}$ phase as well as grain refinement. Individual additions were better than combined additions.

iv. Corrosion resistance was the best in the AZX911 alloy with a continuous network of Al_2Ca phase, and it was slightly lower in the AZY911 alloy with a random distribution of the Mg_3Sb_2 phase.

v. Among the alloys comprising combined additions, the best corrosion resistance was exhibited by the AZXY9120 alloy due to higher and lower volume fraction of the Al_2Ca and Ca_2Sb phases, respectively.

Chapter 8

Conclusions

The effects of combined additions of Ca and Sb on the microstructure, tensile, creep and corrosion behaviour of the AZ91 alloy fabricated by squeeze-casting were investigated. For comparison, the same were also studied on the squeeze-cast AZ91 alloy with and without individual additions of Ca and Sb. Overall conclusions from the current investigation are as follows.

i. Both individual and combined additions of Ca and Sb refined the grain size and β-$Mg_{17}Al_{12}$ phase, which was more pronounced with combined additions.

ii. Besides, α-Mg and β-$Mg_{17}Al_{12}$ phases, individual additions of Ca and Sb in the AZ91 alloy resulted in the formation of a new reticular Al_2Ca and rod-shaped Mg_3Sb_2 phases. Furthermore, combined additions formed an additional Ca_2Sb phase suppressing Mg_3Sb_2 phase.

iii. Additions of both Ca and Sb increased YS at both ambient and elevated temperatures up to 473 K. However, both ductility and UTS decreased first up to 423 K and then increased at 473 K. The increase in YS was attributed to the grain refinement, whereas, the presence of brittle Al_2Ca, Mg_3Sb_2, and Ca_2Sb phases resulted in the reduction of ductility and UTS in the alloys.

iv. The best tensile properties were obtained in the AZXY9110 alloy owing to the presence of a negligible amount of brittle Al_2Ca, and Ca_2Sb phases resulted from the optimum content of 1.0Ca and 0.3Sb (wt.%).

v. The fracture surface of the tensile specimen tested at ambient temperature confirmed cleavage failure that changed to quasi-cleavage at 473 K.

vi. The squeeze-cast alloys even with high Ca and/or Sb content exhibited better tensile properties overcoming the detrimental effects of Ca and/or Sb additions to AZ91 alloy compared to that of the gravity-cast alloys reported in the literature.

vii. Impression creep behaviour of the AZ91 alloy enhanced significantly by the additions of Ca and/or Sb. The improvement was more pronounced by combined additions (except AZXY9111) than the individual additions. The individual addition of Ca was superior to the Sb addition.

viii. The improvement was attributed to the presence of thermally stable Al_2Ca in the AZX911 alloy, Mg_3Sb_2 in the AZY911 alloy and both Al_2Ca as well as Ca_2Sb in the AZXY9110, AZXY9111, and AZXY9120 alloys in addition to the reduced β-$Mg_{17}Al_{12}$ phase. The Al_2Ca phase was more effective in improving creep resistance than the Mg_3Sb_2 phase.

ix. Among the modified alloys, the AZXY9120 alloy exhibited the best creep resistance at the temperature and stress levels employed owing to the presence of highest amount of dense network of lamellar Al_2Ca phase and least content of β-$Mg_{17}Al_{12}$ phase at grain boundaries.

x. The values of stress exponents and activation energies were in the range of 4.3 to 6.4 and 111.9±1.1 to 114.9±3.0 kJ/mol, which suggested dislocation climb aided by pipe diffusion was the governing creep mechanism for all the alloys at the temperature and stress range employed.

xi. Microstructural observation of the creep-tested specimens revealed that the β-$Mg_{17}Al_{12}$ phase in the AZ91 alloy was severely fragmented and aligned in the direction of material flow, which deteriorated its creep resistance. In contrast, the dense lamellar network of the Al_2Ca phase in the AZXY9120 alloy sustained high stresses at elevated temperature without compromising its structural integrity, which resulted in its superior creep resistance.

xii. In electrochemical corrosion test, the alloying additions shifted the OCP towards more noble values except for the AZXY9110 alloy. Variation of corrosion potentials among the alloys employed was not significant, and no particular trend was noted in the OCP values with respect to Ca and Sb contents.

xiii. EIS measurements confirmed the formation of a very weak protective film that degraded with increased immersion time due to localized corrosion attack. Active dissolution took place from the centre of α-Mg grain, and the β-$Mg_{17}Al_{12}$ phase acted as a partially protective phase.

xiv. Corrosion resistance of the AZ91 alloy was the lowest, and it was better for all the modified alloys owing to the refined and reduced amount of β-$Mg_{17}Al_{12}$ phase as well as grain refinement. Individual additions were better than combined additions in improving corrosion resistance.

xv. Corrosion resistance was the best in the AZX911 alloy with a continuous network of Al_2Ca phase, and it was slightly lower in the AZY911 alloy with a random distribution of the Mg_3Sb_2 phase.

xvi. Among the alloys comprising combined additions, the best corrosion resistance was exhibited by the AZXY9120 alloy due to higher and lower volume fraction of the Al_2Ca and Ca_2Sb phases, respectively.

To conclude, the individual and combined additions of Ca and Sb to the AZ91 alloy resulted in improved ambient and elevated temperature tensile properties as well as impression and compression creep behaviour without deteriorating corrosion resistance. Among the modified alloys, the AZXY9120 alloy exhibited the best properties considering its targeted powertrain application at elevated temperature. In addition, the tensile and creep properties of the squeeze-cast alloys in the present investigation were superior as compared to that of the alloys developed by gravity-cast.

8.1 Scope for further research

The following works are suggested as a scope for future research based on the outcomes of the present investigation.

i. The targeted applications of the alloys developed in the present investigation are powertrain components that are subjected to abrasion and vibrations as well. Therefore, a detailed investigation of wear and damping behaviour of all the developed alloys is proposed.

ii. The possibility of production of wrought alloys from the newly developed Ca and/or Sb added AZ91 alloys could be an interesting area of research. Therefore, it is proposed to carry out microstructural and mechanical characterizations of the alloys following secondary processing (like equal-channel angular pressing (ECAP), multi-axial forging (MAF), extrusion, rolling and so on). The influence of texture developed owing to the additions of Ca and/or Sb should be correlated with the mechanical properties.

iii. The effect of heat treatment on mechanical properties of the developed alloys would be an area of research. It would be interesting to compare the properties of the alloys in both as-cast as well as heat treated conditions.

iv. The additions of both Ca and/or Sb to the AZ91 alloy was beneficial, and therefore, the same is proposed to carry out for other Mg-Al based alloys as well to explore the possibility of developing creep resistant Mg alloys for automobile applications.

Appendix I

Appendix I. Chronological development of alloying additions to AZ91 alloy

Sl. No.	Alloying addition	Casting route	Matter investigated	Ref.	Year
1.	AZ91 AZ91+1.0Y AZ91+0.5Sr AZ91+0.5Nd	Squeeze-cast	Microstructure, Hardness, Microfracture mechanism	[43]	1998
2.	AZ91 AZ91+0.15Sb AZ91+0.35Sb AZ91+0.7Sb	Gravity-cast	Microstructure, Tensile behaviour, Creep behaviour	[105]	2000
3.	AZ91+1RE AZ91+2RE AZ91+3RE	Gravity-cast	Microstructure, Hardness, Tensile behaviour, Fracture behaviour	[201]	2000
4.	AZ91+(0.5 ,1.0, 2.0, 3.0)Bi AZ91+(0.1, 0.4, 0.7, 1.0)Sb AZ91+0.5Bi+0.4Sb AZ91+1.0Bi+0.4Sb	Gravity-cast	Microstructure, Tensile behaviour, Creep behaviour	[7]	2001
5.	AZ91+0.5Ca AZ91+1.0Ca AZ91+2.0Ca	Gravity-cast	Microstructure, Tensile behaviour	[13]	2001
6.	Mg-9Al Mg-9Al-1.6RE Mg-9Al-1.2Zn Mg-9Al-1.2Zn-1.6RE	Gravity-cast	Microstructure, Solidification behaviour	[202]	2003
7.	AZ91+0.1Au	Gravity-cast	Microstructure, Ageing behaviour, Creep properties	[203]	2003
8.	AZ91+0.3Ca AZ91+0.3Ca+0.3RE AZ91+0.3Ca+1.0RE AZ91+0.3Ca+3.0RE	Gravity-cast	Microstructure, Tensile behaviour, Creep behaviour	[104]	2003

9.	AZ91+(0.3, 0.5, 1.0, 2.0, 3.0, 4.0)Ca AZ91+(0.5, 1.0, 1.2, 1.5)RE AZ91+1.0Ca+1.0RE AZ91+2.0Ca+1.0RE AZ91+3.0Ca+1.0RE AZ91+4.0Ca+1.0RE	Gravity-cast	Microstructure, Tensile behaviour, Corrosion behaviour	[12]	2005
10.	AZ91+0.4Ca AZ91+1.0Ca	Gravity-cast	Microstructure, Hot-cracking mechanism	[204]	2005
11.	AZ91 AZ91+1.0Ca+0.5Sr	Gravity-cast	Microstructure, Tensile behaviour, Creep behaviour	[205]	2005
12.	AZ91+0.1Ca AZ91+1.0Ca	Gravity-cast	Microstructure, Tensile behaviour	[14]	2005
13.	AZ91+1.0RE AZ91+2.0RE AZ91+3.0RE	Gravity-cast	Microstructure, Hardness, Tensile behaviour	[71]	2005
14.	AZ91 AZ91+0.3Ca AZ91+0.7Ca AZ91+1.0Ca AZ91+2.0Ca AZ91+5.0Ca	Gravity-cast	Microstructure, Tensile behaviour	[206]	2005
15.	AZ91 AZ91+0.5RE AZ91+1.0RE AZ91+1.2RE AZ91+1.5RE AZ91+1.0RE+1.0Ca AZ91+1.0RE+2.0Ca AZ91+1.0RE+3.0Ca AZ91+1.0RE+4.0Ca	Gravity-cast	Corrosion behaviour	[207]	2005
16.	AZ91+0.5Ce AZ91+1.0Ce AZ91+1.0Ce+0.5Ca AZ91+1.0Nd AZ91+1.0Y	Squeeze-cast	Creep behaviour	[208]	2005

17.	AZ91+0.3Ca AZ91+0.3Ca+ 0.2Si AZ91+0.3Ca+ 0.4Si AZ91+0.3Ca+ 0.6Si	Gravity-cast	Microstructure, Tensile behaviour, Creep behaviour	[66]	2006
18.	AZ91+0.5Ce AZ91+1.0Ce AZ91+1.5Ce AZ91+2.0Ce	Gravity-cast	Microstructure, Tensile behaviour, Corrosion behaviour	[154]	2006
19.	AZ91+0.24Ho AZ91+0.44Ho	Gravity-cast	Microstructure, Corrosion behaviour	[155]	2006
20.	AZ91+0.1Ca AZ91+0.3Ca AZ91+0.5Ca	Gravity-cast	Microstructure, Grain refinement properties	[67]	2006
21.	AZ91+0.4Ca AZ91+0.6Ca AZ91+1.0Ca	Gravity-cast	Microstructure, Grain refinement properties	[209]	2007
22.	AZ91D AZ91+0.3Sr AZ91+0.5Sr AZ91+1.0Sr AZ91+1.5Sr AZ91+2.0Sr	Gravity-cast	Microstructure, Tensile behaviour, Corrosion behaviour	[210]	2007
23.	AZ91D AZ91+0.2Sc AZ91+0.4Sc AZ91+0.6Sc	Gravity-cast	Microstructure, Corrosion behaviour	[211]	2007
24.	AZ91+0.5Ca+0.5Sr AZ91+1.0Ca+0.5Sr AZ91+2.0Ca+0.5Sr	Gravity-cast	Microstructure, Creep behaviour	[212]	2007
25.	AZ91+0.8Ce AZ91+0.2Ca+0.8Ce AZ91+0.2Sr+0.8Ce	Gravity-cast	Microstructure, Grain refinement properties	[213]	2008
26.	AZ91+0.5Si+0.2Sb	Gravity-cast	Microstructure, Creep behaviour	[10]	2008

27.	AZ91 AZ91+1.0Ca+4.5Nd	Sand cast	Microstructure, Thermal analysis	[214]	2008
28.	AZ91+(0.5, 1.0, 1.5, 2.0)Ca AZ91+0.5Ca+0.5Y AZ91+1.0Ca+0.5Y AZ91+1.5Ca+0.5Y AZ91+2.0Ca+0.5Y	Gravity-cast	Microstructure, Oxidation behaviour	[215]	2008
29.	AZ91D AZ91+1.0RE AZ91+2.0RE AZ91+0.3Sr AZ91+0.6Sr AZ91+1.4Sr AZ91+1.0RE+0.5Sr AZ91+1.0RE+0.8Sr	Gravity-cast	Microstructure, Corrosion behaviour	[216]	2008
30.	AZ91 AZ91+0.1Sr AZ91+0.2Sr AZ91+0.3Sr	Gravity-cast	Microstructure, Refinement mechanism	[217]	2008
31.	AZ91+3.0Ca	Cooling Slope Method	Microstructure	[218]	2008
32.	AZ91+1.0RE AZ91+2.0RE AZ91+3.0RE	Gravity-cast	Microstructure, Thermal fatigue	[219]	2009
33.	AZ91+0.5Y AZ91+1.0Y AZ91+2.0Y	Gravity-cast	Microstructure, Tensile behaviour	[220]	2009
34.	AZ91+0.14Ca AZ91+0.4Sb AZ91+0.4Sb+1.0Bi	Gravity-cast	Microstructure, Electrochemical corrosion behaviour	[157]	2009
35.	AZ91+(0.5, 1.0, 1.5, 2.0)Ca AZ91+0.5Ca+0.5Y AZ91+1.0Ca+0.5Y AZ91+1.5Ca+0.5Y AZ91+2.0Ca+0.5Y	Gravity-cast	Oxidation behaviour	[215]	2009

36.	AZ91+1.0RE AZ91+2.0RE AZ91+0.25Si AZ91+0.5Si AZ91+1.0Si AZ91+2.05Si	Gravity-cast	Microstructure, Tensile behaviour, Creep behaviour	[221]	2009
37.	AZ91+1.0Ca AZ91+3.0Ca AZ91+5.0Ca	Gravity-cast	Microstructure, Creep behaviour	[102]	2009
38.	AZ91 AZ91+0.3Sc	Gravity-cast	Microstructure, Tensile behaviour	[222]	2009
39.	AZ91+0.4Pr AZ91+0.8Pr AZ91+1.2Pr	HPDC	Microstructure, Hardness, Tensile behaviour	[223]	2010
40.	AZ91+(0.2, 0.4, 0.6, 0.8, 1.0)Ce	Gravity-cast	Solid solution effect, Aging response	[224]	2010
41.	AZ91+1.0RE AZ91+2.0RE AZ91+3.0RE	Gravity-cast	Microstructure, Hardness, Tensile behaviour, Wear behaviour	[101]	2010
42.	AZ91 AZ91+1.0RE+1.2Ca	Gravity-cast	Microstructure, Creep behaviour	[114]	2010
43.	AZ91+0.5Nd AZ91+1.0Nd AZ91+1.5Nd	Gravity-cast	Microstructure, Tensile behaviour, Fatigue behaviour	[225]	2010
44.	AZ91+0.5Ce AZ91+1.0Ce AZ91+1.5Ce AZ91+1.0Nd AZ91+1.0Y	Die-cast	Microstructure, Tensile behaviour, Creep behaviour	[226]	2010
45.	AZ91+1.0Y	Gravity-cast	Microstructure, Tensile behaviour, Corrosion behaviour, Fracture morphology	[227]	2010

46.	AZ91+2.0Ca	Squeeze-cast	Micro hardness, Tensile behaviour	[228]	2010
47.	AZ91+1.0Y+0.5Ca AZ91+1.0Y+1.0Ca AZ91+1.0Y+1.5Ca	Die-cast	Microstructure, Tensile behaviour	[8]	2010
48.	AZ91 AZ91+0.1RE AZ91+0.1Sr AZ91+0.1RE+0.1Sr	Die-cast	Microstructure, Dendrite growth	[229]	2010
49.	AZ91+1.0RE+1.2Ca	Thixoform	Impression creep behaviour	[230]	2011
50.	AZ91 AZ91+1.0RE+1.2Ca	Gravity-cast	Microstructure, Impression creep behaviour	[231]	2011
51.	AZ91+1.0C	Gravity-cast	Microstructure, Hot rolling behaviour	[232]	2011
52.	AZ91 AZ91+0.5Er	Gravity-cast	Microstructure, Corrosion behaviour	[233]	2011
53.	AZ91 AZ91+0.2Ti AZ91+0.4Ti AZ91+0.8Ti	Gravity-cast	Corrosion behaviour	[234]	2011
54.	AZ91 AZ91+0.5Sb AZ91+0.5Si AZ91+0.5Si+0.2Sb	Gravity-cast	Creep behaviour, Corrosion behaviour	[11]	2011
55.	AZ91+0.2Ti AZ91+0.5Ti	Gravity-cast	Hardness, Tensile behaviour, Corrosion behaviour	[235]	2011

56.	AZ91+0.5RE	Squeeze-cast	Microstructure, Tensile behaviour	[40]	2012
57.	AZ91+(0.45-0.9)Zn	Gravity-cast	Microstructure, Corrosion behaviour	[236]	2012
58.	AZ91+0.3Ce	Gravity-cast	Microstructure, Fatigue behaviour	[237]	2012
59.	AZ91+1.0Ce AZ91+2.0Ce AZ91+3.0Ce	Gravity-cast	Corrosion behaviour, Damping behaviour	[238]	2012
60.	AZ91D AZ91D+0.4Ca+0.3Sr AZ91D+0.4Ca+0.3Sr+3.0Gd+3.0Y	Gravity-cast	Microstructure, Tensile behaviour, Fatigue behaviour	[239]	2012
61.	AZ91 AZ91+0.5Sn AZ91+1.0Sn AZ91+2.0Sn	Gravity-cast	Microstructure, Hardness, Tensile behaviour, Casting properties	[74]	2013
62.	AZ91 AZ91+0.5Sn AZ91+1.0Sn AZ91+2.0Sn	Gravity-cast	Microstructure, Impression creep behaviour	[111]	2013
63.	AZ91+0.5Sb AZ91+0.5Si AZ91+0.5Si+0.2Sb	Gravity-cast	Microstructure, Creep behaviour	[240]	2013
64.	AZ91+0.4Nd	Gravity-cast	Corrosion behaviour	[241]	2013
65.	AZ91 AZ91+0.4Nd	Gravity-cast	Corrosion behaviour	[242]	2013

66.	AZ91+1.0Ca+3.0Sn AZ91+2.0Ca+3.0Sn	Gravity-cast	Creep behaviour	[243]	2014
67.	AZ91+1.0Ca AZ91+2.0Ca AZ91+3.0Ca	Squeeze-cast	Microstructure, Tensile behaviour	[17]	2014
68.	AZ91+RE	Die-cast	Corrosion behaviour	[244]	2014
69.	AZ91+0.2Bi AZ91+0.5Bi AZ91+1.0Bi	Die-cast	Microstructure, Hardness, Tensile behaviour	[245]	2015
70.	AZ91+2.0Ca	Rheo-Squeeze-cast	Microstructure, Tensile behaviour	[246]	2015
71.	AZ91+0.5Ca AZ91+1.0Ca AZ91+1.5Ca	Gravity-cast	Microstructure, Corrosion behaviour	[247]	2015
72.	AZ91 AZ91+0.6Sb AZ91+0.9Ca AZ91+0.9Ca+0.3Sb AZ91+0.9Ca+0.6Sb AZ91+1.8Ca+0.3Sb	Squeeze-cast	Microstructure, Tensile behaviour, Creep behaviour, Corrosion behaviour	Present study	2016

References

[1] A.A. Luo, Recent magnesium alloy development for elevated temperature applications, Int. Mater. Rev. 49 (2004) 13–30.

[2] M.O. Pekguleryuz, A.A. Kaya, Creep resistant magnesium alloys for powertrain applications, Adv. Eng. Mater. 5 (2003) 866–878.

[3] B.L. Mordike, T. Ebert, Magnesium properties - applications - potential, Mater. Sci. Eng. A. 302 (2001) 37–45.

[4] A. Luo, M.O. Pekguleryuz, Cast magnesium alloys for elevated temperature applications, J. Mater. Sci. 29 (1994) 5259–5271.

[5] M.O. Pekguleryuz, Development of creep resistant magnesium diecasting alloys, Mater. Sci. Forum. 350–351 (2000) 131–140.

[6] B.C. Pai, U.T.S. Pillai, P. Manikandan, A. Srinivasan, Modification of AZ91 Mg alloys for high temperature applications, Trans. Indian Inst. Met. 65 (2012) 601–606.

[7] Y. Guangyin, S. Yangshan, D. Wenjiang, Effects of bismuth and antimony additions on the microstructure and mechanical properties of AZ91 magnesium alloy, Mater. Sci. Eng. A. 308 (2001) 38–44.

[8] F. Wang, Y. Wang, P.L. Mao, B.Y. Yu, Q.Y. Guo, Effects of combined addition of Y and Ca on microstructure and mechanical properties of die casting AZ91 alloy, Trans. Nonferrous Met. Soc. China. 20 (2010) s311–s317.

[9] A. Srinivasan, U.T.S. Pillai, B.C. Pai, Microstructure and mechanical properties of Si and Sb added AZ91 magnesium alloy, Metall. Mater. Trans. A. 36 (2005) 2235–2243.

[10] A. Srinivasan, J. Swaminathan, U.T.S. Pillai, K. Guguloth, B.C. Pai, Effect of combined addition of Si and Sb on the microstructure and creep properties of AZ91 magnesium alloy, Mater. Sci. Eng. A. 485 (2008) 86–91.

[11] U.T.S. Pillai, A. Srinivasan, K. Raghukandan, B.C. Pai, Development of magnesium based alloys for high temperature applications, Mater. Sci. Forum. 673 (2011) 179–184.

[12] G. Wu, Y. Fan, H. Gao, C. Zhai, Y.P. Zhu, The effect of Ca and rare earth elements on the microstructure, mechanical properties and corrosion behavior of AZ91D, Mater. Sci. Eng. A. 408 (2005) 255–263.

[13] W. Qudong, C. Wenzhou, Z. Xiaoqin, L.U. Yizhen, Effects of Ca addition on the microstructure and mechanical properties of AZ91 magnesium alloy, J. Mater. Sci. 36 (2001) 3035–3040.

[14] P. Li, B. Tang, E.G. Kandalova, Microstructure and properties of AZ91D alloy with Ca additions, Mater. Lett. 59 (2005) 671–675.

[15] H. Liu, N. Gong, L. Pang, X. Zhang, Microstructure and mechanical properties of as-cast AZ31 with the addition of Sb, Mater. Sci. Eng. A. 497 (2008) 254–259.

[16] N. Balasubramani, A. Srinivasan, U.T.S. Pillai, K. Raghukandan, B.C. Pai, Effect of antimony addition on the microstructure and mechanical properties of ZA84

magnesium alloy, J. Alloys Compd. 455 (2008) 168–173.

[17] Y. Zhang, G. Wu, W. Liu, L. Zhang, S. Pang, Y. Wang, et al., Effects of processing parameters and Ca content on microstructure and mechanical properties of squeeze casting AZ91-Ca alloys, Mater. Sci. Eng. A. 595 (2014) 109–117.

[18] G.E. Dieter, D. Bacon, G.L. Wilkes, Mechanical metallurgy, SI Metric, McGraw-Hill, 1988.

[19] Manoj Gupta, Nai Mui Ling Sharon, Magnesium, magnesium alloys, and magnesium composites, John Wiley & Sons, 2011.

[20] M.M. Avedesian, H. Baker, ASM specialty handbook: magnesium and magnesium alloys, ASM International, 1999.

[21] Z.P. Luo, D.Y. Song, S.Q. Zhang, Strengthening effects of rare earths on wrought Mg-Zn-Zr-RE alloys, J. Alloys Compd. 230 (1995) 109–114.

[22] K. Maruyama, M. Suzuki, H. Sato, Creep strength of magnesium-based alloys, Metall. Mater. Trans. A. 33 (2002) 875–882.

[23] P. Abachi, A. Masoudi, K. Purazrang, Dry sliding wear behavior of SiCP/QE22 magnesium alloy matrix composites, Mater. Sci. Eng. A. 435 (2006) 653–657.

[24] J.L. Murray, Phase diagrams of binary magnesium alloys, ASM International, Ohio, 1988.

[25] S. Celotto, TEM Study of continuous precipitation in Mg-9wt%Al-1wt%Zn alloy, Acta Mater. 48 (2000) 1775–1787.

[26] A.K. Dahle, Y.C. Lee, M.D. Nave, P.L. Scha, D.H. Stjohn, Development of the as-cast microstructure in magnesium-aluminium alloys, J. Light Met. 1 (2001) 61–72.

[27] M.D. Nave, A.K. Dahle, D.H. StJohn, Eutectic growth morphologies in magnesium-aluminium alloys, in: H.I. Kaplan, J. Hryn, B. Clow (Eds.), Magnes. Technol. 2000, 2000: pp. 233–242.

[28] Z. Yang, J.P. Li, J.X. Zhang, G.W. Lorimer, J. Robson, Review on research and development of magnesium alloys, Acta Metall. Sin. 21 (2008) 313–328.

[29] O. Lunder, T.K. Aune, K. Nisancioglu, Effect of Mn additions on the corrosion behavior of mould-cast magnesium ASTM AZ91, Corrosion. 43 (1987) 291–295.

[30] A. Luo, Understanding the solidification of magnesium alloys, in: Proc. 3rd Int. Magnes. Conf., Manchester, UK, 1996: pp. 449–464.

[31] W. Kurz, K. Fisher, Fundamentals of solidification., Trans Tech Publications, 1986.

[32] G.V. Raynor, The physical metallurgy of magnesium and its alloys, Pergamon Press Ltd, London, 1959.

[33] A. Maleki, B. Niroumand, A. Shafyei, Effects of squeeze casting parameters on density, macrostructure and hardness of LM13 alloy, Mater. Sci. Eng. A. 428 (2006) 135–140.

[34] A.J. Clegg, Precision casting processes, Pergamon Press, Oxford, 1991.

[35] D.J. Britnell, K. Neailey, Macrosegregation in thin walled castings produced via the direct squeeze casting process, J. Mater. Process. Technol. 138 (2003) 306–310.

[36] A.A. Luo, Magnesium casting technology for structural applications, J. Magnes. Alloy. 1 (2013) 2–22.

[37] S. Kleiner, O. Beffort, A. Wahlen, P.J. Uggowitzer, Microstructure and mechanical properties of squeeze cast and semi-solid cast Mg-Al alloys, J. Light Met. 2 (2002) 277–280.

[38] H. Shastri, Correlation of microstructure with tensile , creep and corrosion behaviour of AZ91 Mg alloy fabricated by three different casting techniques, National Institute of Technology Rourkela, 2015.

[39] S.M. Zhu, B.L. Mordike, J.F. Nie, Creep properties of a Mg-Al-Ca alloy produced by different casting technologies, Mater. Sci. Eng. A. 483–484 (2008) 583–586.

[40] Q. Chen, B. Yuan, G. Zhao, D. Shu, C. Hu, Z. Zhao, et al., Microstructural evolution during reheating and tensile mechanical properties of thixoforged AZ91D-RE magnesium alloy prepared by squeeze casting–solid extrusion, Mater. Sci. Eng. A. 537 (2012) 25–38.

[41] C.S. Goh, K.S. Soh, P.H. Oon, B.W. Chua, Effect of squeeze casting parameters on the mechanical properties of AZ91-Ca Mg alloys, Mater. Des. 31 (2010) S50–S53.

[42] Z. Han, H. Pan, Y. Li, A.A. Luo, A.K. Sachdev, Study on pressurized solidification behavior and microstructure characteristics of squeeze casting magnesium alloy AZ91D, Metall. Mater. Trans. B. 46B (2015) 328–336.

[43] S. Lee, S.H. Lee, D.H. Kim, Effect of Y, Sr, and Nd additions on the microstructure and microfracture mechanism of squeeze-cast AZ91-X magnesium alloys, Metall. Mater. Trans. A. 29 (1998) 1221–1235.

[44] Y.L. Yang, L.M. Peng, P.H. Fu, B. Hu, W.J. Ding, Study on microstructure of squeeze casting AZ91D alloy, Mater. Sci. Technol. 27 (2011) 189–193.

[45] G.M. Han, Z.Q. Han, a. a. Luo, B.C. Liu, Microstructure characteristics and effect of aging process on the mechanical properties of squeeze-cast AZ91 alloy, J. Alloys Compd. 641 (2015) 56–63.

[46] S.C. Kurnaz, H. Sevik, S. Aikgöz, A. Özel, Influence of titanium and chromium addition on the microstructure and mechanical properties of squeeze cast Mg-6Al alloy, J. Alloys Compd. 509 (2011) 3190–3196.

[47] Y.Z. Lü, Q.D. Wang, W.J. Ding, X.Q. Zeng, Y.P. Zhu, Fracture behavior of AZ91 magnesium alloy, Mater. Lett. 44 (2000) 265–268.

[48] I. J. Polmear, Recent developments in light alloys, Mater. Trans. JIM. 37 (1996) 12–31.

[49] D.G. Leo Prakash, D. Regener, W.J.J. Vorster, Effect of position on the tensile properties in high-pressure die cast Mg alloy, J. Alloys Compd. 470 (2009) 111–116.

[50] M. Mabuchi, M. Kobata, Y. Chino, H. Iwasaki, Tensile properties of directionally solidified AZ91 Mg alloy, Mater. Trans. 44 (2003) 436–439.

[51] Z. Zhang, H. Yu, G. Chen, H. Yu, C. Xu, Correlation between microstructure and tensile properties in powder metallurgy AZ91 alloys, Mater. Lett. 65 (2011) 2686–2689.

[52] Y. Li, Y. Chen, H. Cui, B. Xiong, J. Zhang, Microstructure and mechanical properties of spray-formed AZ91 magnesium alloy, Mater. Charact. 60 (2009) 240–245.

[53] S.S. Park, Y.S. Park, N.J. Kim, Microstructure and properties of strip cast AZ91 Mg alloy, Met. Mater. Int. 8 (2002) 551–554.

[54] D. Gao, Z. Li, Q. Han, Q. Zhai, Effect of ultrasonic power on microstructure and mechanical properties of AZ91 alloy, Mater. Sci. Eng. A. 502 (2009) 2–5.

[55] M. Khosro Aghayani, B. Niroumand, Effects of ultrasonic treatment on microstructure and tensile strength of AZ91 magnesium alloy, J. Alloys Compd. 509 (2011) 114–122.

[56] Y. Yang, J. Wang, T. Wang, C. Liu, Z. Zhang, Effects of ultrasonic treatment on microstructures of AZ91 alloy, Trans. Nonferrous Met. Soc. China. 24 (2014) 76–81.

[57] M. Mabuchi, K. Ameyama, H. Iwasaki, K. Higashi, Low temperature superplasticity of AZ91 magnesium alloy with non-equilibrium grain boundaries, Acta Mater. 47 (1999) 2047–2057.

[58] K. Máthis, J. Gubicza, N.H. Nam, Microstructure and mechanical behavior of AZ91 Mg alloy processed by equal channel angular pressing, J. Alloys Compd. 394 (2005) 194–199.

[59] B. Chen, D.-L. Lin, L. Jin, X.-Q. Zeng, C. Lu, Equal-channel angular pressing of magnesium alloy AZ91 and its effects on microstructure and mechanical properties, Mater. Sci. Eng. A. 483–484 (2008) 113–116.

[60] H. Ding, L. Liu, S. Kamado, W. Ding, Y. Kojima, Study of the microstructure, texture and tensile properties of as-extruded AZ91 magnesium alloy, J. Alloys Compd. 456 (2008) 400–406.

[61] P. Cavaliere, P.P. De Marco, Superplastic behaviour of friction stir processed AZ91 magnesium alloy produced by high pressure die cast, J. Mater. Process. Technol. 184 (2007) 77–83.

[62] D. Zhang, S. Wang, C. Qiu, W. Zhang, Superplastic tensile behavior of a fine-grained AZ91 magnesium alloy prepared by friction stir processing, Mater. Sci. Eng. A. 556 (2012) 100–106.

[63] Y. Jiang, G. Tang, C. Shek, Y. Zhu, Effect of electropulsing treatment on microstructure and tensile fracture behavior of aged Mg–9Al–1Zn alloy strip, Appl. Phys. A. 97 (2009) 607–615.

[64] C.D. Lee, K.S. Shin, Effect of microporosity on the tensile properties of AZ91 magnesium alloy, Acta Mater. 55 (2007) 4293–4303.

[65] C.D. Lee, Tensile properties of high-pressure die-cast AM60 and AZ91 magnesium alloys on microporosity variation, J. Mater. Sci. 42 (2007) 10032–10039.

[66] X. Feng, M. Xuegang, S. Yangshan, Microstructures and mechanical properties of AZ91 alloy with combined additions of Ca and Si, J. Mater. Sci. 41 (2006) 4725–4731.

[67] S. Liu, L. Kang, H. Han, Z. Wang, The role of calcium in microstructural refinement of AZ91 magnesium alloy, J. Wuhan Univ. Technol. Mater. Sci. Ed. 21 (2006) 45–47.

[68] D.B. Lee, High temperature oxidation of AZ31+0.3wt.%Ca and AZ31+0.3wt.%CaO magnesium alloys, Corros. Sci. 70 (2013) 243–251.

[69] B.-H. Choi, B.-S. You, W.-W. Park, Y.-B. Huang, I.-M. Park, Effect of Ca addition on the oxidation resistance of AZ91 magnesium alloys at elevated temperatures, Met. Mater. Int. 9 (2003) 395–398.

[70] B. Nami, S. Rashno, S.M. Miresmaeili, Effect of tin on the microstructure and impression creep behavior of MRI153 magnesium alloy, J. Alloys Compd. 639 (2015) 308–314.

[71] F. Khomamizadeh, B. Nami, S. Khoshkhooei, Effect of rare-earth element additions on high-temperature mechanical properties of AZ91 magnesium alloy, Metall. Mater. Trans. A. 36 (2005) 3489–3494.

[72] R. Mahmudi, F. Kabirian, Z. Nematollahi, Microstructural stability and high-temperature mechanical properties of AZ91 and AZ91+2RE magnesium alloys, Mater. Des. 32 (2011) 2583–2589.

[73] Q. Wang, W. Chen, W. Ding, Y. Zhu, M. Mabuchi, Effect of Sb on the microstructure and mechanical properties of AZ91 magnesium alloy, Metall. Mater. Trans. A. 32 (2001) 787–794.

[74] Y. Turen, Effect of Sn addition on microstructure, mechanical and casting properties of AZ91 alloy, Mater. Des. 49 (2013) 1009–1015.

[75] H.L. Zhao, S.K. Guan, F.Y. Zheng, Effects of Sr and B addition on microstructure and mechanical properties of AZ91 magnesium alloy, J. Mater. Res. 22 (2007) 2423–2428.

[76] Y. Chen, H. Liu, R. Ye, G. Liu, Effects of the addition of Ca and Sb on the microstructure and mechanical properties of AZ91 magnesium, Mater. Sci. Eng. A. 587 (2013) 262–267.

[77] W.D. Callister, Materials science and engineering: an introduction, 5th ed., John Wiley & Sons, New York, 2000.

[78] M.A. Meyers, K.K. Chawla, Mechanical behavior of materials, Cambridge University Press, 2009.

[79] J.-P. Poirier, Creep of crystals : high-temperature deformation processes in metals, ceramics, and minerals, Cambridge University Press, 1985.

[80] C. Herring, Diffusional viscosity of a polycrystalline solid, J. Appl. Phys. 21 (1950) 437–445.

[81] T.G. Langdon, Identifiying creep mechanisms at low stresses, Mater. Sci. Eng. A. 283 (2000) 266–273.

[82] T.G. Langdon, Grain boundary sliding revisited: Developments in sliding over four decades, J. Mater. Sci. 41 (2006) 597–609.

[83] R.L. Coble, A model for boundary diffusion controlled creep in polycrystalline materials, J. Appl. Phys. 34 (1963) 1679–1682.

[84] I.M. Lifshitz, On the theory of diffusion-viscous flow of polycrystalline bodies, Sov. Phys. JETP. 17 (1963) 1349–1367.

[85] K. Milička, J. Cadek, P. Rys, High temperature creep mechanisms in magnesium, Acta Metall. 18 (1970) 1071–1082.

[86] K. Milička, P. Pérez, F. Dobeš, G. Garcés, P. Adeva, Creep of high-strength Mg-Ni-Y-RE alloys, Mater. Sci. Eng. A. 510–511 (2009) 377–381.

[87] A. Saxena, Nonlinear fracture mechanics for engineers, illustrate, CRC Press, 1998.

[88] O.D. Sherby, A.K. Miller, Combining phenomenology and physics in describing the

high temperature mechanical behavior of crystalline solids, J. Eng. Mater. Technol. 101 (1979) 387–395.

[89] A.K. Mukherjee, J.E. Bird, J.E. Dorn, Experimental corelations for high temperature creep, Trans ASM. 62 (1969) 155–179.

[90] Z. Xiao Guo, The deformation and processing of structural materials, Taylor & Francis, 2005.

[91] H. Gjestland, G. Nussbaum, G. Regazzoni, O. Lohne, Ø. Bauger, Stress-relaxation and creep behaviour of some rapidly solidified magnesium alloys, Mater. Sci. Eng. A. 134 (1991) 1197–1200.

[92] K. Lovold, Transient creep in pressure-die-cast Mg alloys, Zeitschrift Fur Met. 67 (1976) 514–517.

[93] M.O. Pekguleryuz, M.M. Avedesian, Magnesium alloying, some potentials for alloy development, J. Jpn. Inst. Light Met. 42 (1992) 679–686.

[94] M.S. Dargusch, K. Pettersen, K. Nogita, M.D. Nave, G.L. Dunlop, The effect of aluminium content on the mechanical properties and microstructure of die cast binary magnesium-aluminium alloys, Mater. Trans. 47 (2006) 977–982.

[95] M. Regev, E. Aghion, A. Rosen, Creep studies of AZ91D pressure die casting, Mater. Sci. Eng. A. 234–236 (1997) 123–126.

[96] W. Blum, P. Zhang, B. Watzinger, B.V. Grossmann, H.G. Haldenwanger, Comparative study of creep of the die-cast Mg-alloys AZ91, AS21, AS41, AM60 and AE42, Mater. Sci. Eng. A. 319 (2001) 735–740.

[97] W.K. Miller, Creep of die cast AZ91 magnesium at room temperature and low stress, Metall. Trans. A. 22 (1991) 873–877.

[98] M.S. Dargusch, G.L. Dunlop, Elevated temperature creep and microstructure of die cast Mg alloys, in: Michael Ferry (Ed.), Mater. 98, Institute of Materials Engineering, Australasia Ltd., Wollongong, Australia, 1998: pp. 579–584.

[99] M. Regev, M. Bamberger, A. Rosen, E. Aghion, Creep studies of AZ91D castings, in: B.L. Mordike, K.U. Kainer (Eds.), Magnes. Alloy. Their Appl., Werkstoff-informationsgesellschaft mbH, Frankfurt, Germany, 1998: pp. 283–288.

[100] J. Zhang, X. Niu, X. Qiu, K. Liu, C. Nan, D. Tang, et al., Effect of yttrium-rich misch metal on the microstructures, mechanical properties and corrosion behavior of die cast AZ91 alloy, J. Alloys Compd. 471 (2009) 322–330.

[101] K. Meshinchi Asl, A. Masoudi, F. Khomamizadeh, The effect of different rare earth elements content on microstructure, mechanical and wear behavior of Mg–Al–Zn alloy, Mater. Sci. Eng. A. 527 (2010) 2027–2035.

[102] D. Amberger, P. Eisenlohr, M. Göken, Microstructural evolution during creep of Ca-containing AZ91, Mater. Sci. Eng. A. 510–511 (2009) 398–402.

[103] L. Shepeleva, M. Bamberger, Microstructure of high pressure die cast AZ91D modified with Ca and Ce, Mater. Sci. Eng. A. 425 (2006) 312–317.

[104] D. Wenwen, S. Yangshan, M. Xuegang, X. Feng, Z. Min, W. Dengyun, Microstructure and mechanical properties of Mg-Al based alloy with calcium and rare earth additions, Mater. Sci. Eng. A. 356 (2003) 1–7.

[105] Y. Guangyin, S. Yangshan, D. Wenjiang, Effects of Sb addition on the microstructure

and mechanical properties of AZ91 magnesium alloy, Scr. Mater. 43 (2000) 1009–1013.

[106] Y. Guangyin, W. Qudong, D. Wenjiang, High temperature deformation behavior of permanent casting AZ91 alloy with and without Sb addition, J. Mater. Sci. 37 (2002) 127–132.

[107] D.H. Sastry, Impression creep technique - An overview, Mater. Sci. Eng. A. 409 (2005) 67–75.

[108] J.C.M. Li, Impression creep and other localized tests, Mater. Sci. Eng. A. 322 (2002) 23–42.

[109] F. Yang, J.C.M. Li, Impression test - A review, Mater. Sci. Eng. R Reports. 74 (2013) 233–253.

[110] S. Rashno, B. Nami, S.M. Miresmaeili, Impression creep behavior of a cast MRI153 magnesium alloy, Mater. Des. 60 (2014) 289–294.

[111] R. Mahmudi, S. Moeendarbari, Effects of Sn additions on the microstructure and impression creep behavior of AZ91 magnesium alloy, Mater. Sci. Eng. A. 566 (2013) 30–39.

[112] F. Kabirian, R. Mahmudi, Impression creep behavior of a cast AZ91 magnesium alloy, Metall. Mater. Trans. A. 40 (2009) 116–127.

[113] F. Kabirian, R. Mahmudi, Effects of rare earth element additions on the impression creep behavior of AZ91 magnesium alloy, Metall. Mater. Trans. A. 40 (2009) 2190–2201.

[114] B. Nami, H. Razavi, S. Mirdamadi, S.G. Shabestari, S.M. Miresmaeili, Effect of Ca and rare earth elements on impression creep properties of AZ91 magnesium alloy, Metall. Mater. Trans. A. 41 (2010) 1973–1982.

[115] F. Kabirian, R. Mahmudi, Effects of Zr additions on the microstructure and impression creep behavior of AZ91 magnesium alloy, Metall. Mater. Trans. A. 41 (2010) 3488–3498.

[116] E. Mohammadi Mazraeshahi, B. Nami, S.M. Miresmaeili, S.M. Tabatabaei, Effect of Si on the creep properties of AZ61 cast magnesium alloy, Mater. Des. 76 (2015) 64–70.

[117] B. Amir Esgandari, H. Mehrjoo, B. Nami, S.M. Miresmaeili, The effect of Ca and RE elements on the precipitation kinetics of $Mg_{17}Al_{12}$ phase during artificial aging of magnesium alloy AZ91, Mater. Sci. Eng. A. 528 (2011) 5018–5024.

[118] E. Mohammadi Mazraeshahi, B. Nami, S.M. Miresmaeili, Investigation on the impression creep properties of a cast Mg-6Al-1Zn magnesium alloy, Mater. Des. 51 (2013) 427–431.

[119] A.R. Geranmayeh, R. Mahmudi, Compressive and impression creep behavior of a cast Mg-Al-Zn-Si alloy, Mater. Chem. Phys. 139 (2013) 79–86.

[120] S. Ansary, R. Mahmudi, M.J. Esfandyarpour, Creep of AZ31 Mg alloy: A comparison of impression and tensile behavior, Mater. Sci. Eng. A. 556 (2012) 9–14.

[121] G. Nayyeri, R. Mahmudi, F. Salehi, The microstructure, creep resistance, and high-temperature mechanical properties of Mg-5Sn alloy with Ca and Sb additions, and aging treatment, Mater. Sci. Eng. A. 527 (2010) 5353–5359.

[122] L. Peng, F. Yang, J.F. Nie, J.C.M. Li, Impression creep of a Mg-8Zn-4Al-0.5Ca alloy, Mater. Sci. Eng. A. 410–411 (2005) 42–47.

[123] M.G. Fontana, Corrosion Engineering, reprint, Tata McGraw-Hill Education, 2005.

[124] N. Perez, Electrochemistry and corrosion science, illustrate, Springer Science & Business Media, 2004.

[125] G.L. Song, A. Atrens, Corrosion mechanisms of magnesium alloys, Adv. Eng. Mater. 1 (1999) 11–33.

[126] M. Park, ASM handbook corrosion : Materials, 2005.

[127] J. Oldfield, Electrochemical theory of galvanic corrosion, in: Galvanic Corros., ASTM International, 100 Barr Harbor Drive, PO Box C700, West Conshohocken, PA 19428-2959, 1988: p. 18.

[128] G.S. Frankel, Pitting corrosion of metals, J. Electrochem. Soc. 145 (1998) 2186–2198.

[129] J.R. Davis, Corrosion: understanding the basics, ASM International, 2000.

[130] R.N. Parkins, Stress Corrosion Cracking, in: R.W. Revie (Ed.), Uhlig's Corros. Handb., John Wiley & Sons, 2011: pp. 171–182.

[131] N.D. Tomashov, Theory and protection of metals: the science of corrosion, The Macmillan Company, New York, 1966.

[132] G. Makar, J. Kruger, Corrosion of magnesium, Int. Mater. Rev. 38 (1993) 138–153.

[133] E. Ghali, Corrosion resistance of aluminum and magnesium alloys, John Wiley & Sons, Inc., 2010.

[134] P. Kurze, Corrosion and surface protections, in: Magnes. Technol. Metall. Des. Data, Appl., Springer Berlin Heidelberg, 2006: pp. 431–497.

[135] K.W. Guo, A review of magnesium/magnesium alloys corrosion and its protection, Recent Patents Corros. Sci. 2 (2010) 13–21.

[136] G. Song, A. Atrens, M. Dargusch, Influence of microstructure on the corrosion of diecast AZ91D, Corros. Sci. 41 (1999) 249–273.

[137] G.L. Song, Corrosion of magnesium alloys, Woodhead Publishing Limited, 2011.

[138] O. Khaselev, J. Yahalom, The anodic behavior of binary Mg-Al alloys in KOH-aluminate solutions, Corros. Sci. 40 (1998) 1149–1160.

[139] O. Lunder, J.H. Nordien, K. Nisancioglu, Corrosion resistance of cast Mg-Al alloys, Corros. Rev. 15 (1997) 439–470.

[140] S. Mathieu, C. Rapin, J. Steinmetz, P. Steinmetz, A corrosion study of the main constituent phases of AZ91 magnesium alloys, Corros. Sci. 45 (2003) 2741–2755.

[141] T.J. Warner, N.A. Thorne, G. Nussbaum, W.M. Stobbs, A cross-sectional TEM study of corrosion initiation in rapidly solidified Mg-based ribbons, Surf. Interface Anal. 19 (1992) 386–392.

[142] F. Hermann, F. Sommer, H. Jones, R.G.J. Edyvean, Corrosion inhibition in magnesium-aluminium-based alloys induced by rapid solidification processing, J. Mater. Sci. 24 (1989) 2369–2379.

[143] G. Song, A. Atrens, Understanding magnesium corrosion—A framework for

improved alloy performance, Adv. Eng. Mater. 5 (2003) 837–858.

[144] D.A. Vermilyea, C.F. Kirk, Studies of inhibition of magnesium corrosion, J. Electrochem. Soc. 116 (1969) 1487–1492.

[145] G. Song, A. Atrens, X. Wu, B. Zhang, Corrosion behaviour of AZ21, AZ501 and AZ91 in Sodium Chloride, Corros. Sci. 40 (1998) 1769–1791.

[146] N. Pebere, C. Riera, F. Dabosi, Investigation of magnesium corrosion in aerated sodium sulfate solution by electrochemical impedance spectroscopy, Electrochim. Acta. 35 (1990) 555–561.

[147] R. Ambat, N.N. Aung, W. Zhou, Evaluation of microstructural effects on corrosion behaviour of AZ91D magnesium alloy, Corros. Sci. 42 (2000) 1433–1455.

[148] M.C. Zhao, M. Liu, G. Song, A. Atrens, Influence of the β-phase morphology on the corrosion of the Mg alloy AZ91, Corros. Sci. 50 (2008) 1939–1953.

[149] R. Ambat, N.N. Aung, W. Zhou, Studies on the influence of chloride ion and pH on the corrosion and electrochemical behaviour of AZ91D magnesium alloy, J. Appl. Electrochem. 30 (2000) 865–874.

[150] S. Mathieu, C. Rapin, J. Hazan, P. Steinmetz, Corrosion behaviour of high pressure die-cast and semi-solid cast AZ91D alloys, Corros. Sci. 44 (2002) 2737–2756.

[151] G. Song, A.L. Bowles, D.H. StJohn, Corrosion resistance of aged die cast magnesium alloy AZ91D, Mater. Sci. Eng. A. 366 (2004) 74–86.

[152] O. Lunder, J.E. Lein, T.K. Aune, K. Nisancioglu, The role of $Mg_{17}Al_{12}$ phase in the corrosion of Mg alloy AZ91, Corrosion. 45 (1989) 741–748.

[153] M.-C. Zhao, M. Liu, G.L. Song, A. Atrens, Influence of homogenization annealing of AZ91 on mechanical properties and corrosion behavior, Adv. Eng. Mater. 10 (2008) 93–103.

[154] Y. Fan, G. Wu, C. Zhai, Influence of cerium on the microstructure, mechanical properties and corrosion resistance of magnesium alloy, Mater. Sci. Eng. A. 433 (2006) 208–215.

[155] X. Zhou, Y. Huang, Z. Wei, Q. Chen, F. Gan, Improvement of corrosion resistance of AZ91D magnesium alloy by holmium addition, Corros. Sci. 48 (2006) 4223–4233.

[156] A. Srinivasan, S. Ningshen, U. Kamachi Mudali, U.T.S. Pillai, B.C. Pai, Influence of Si and Sb additions on the corrosion behavior of AZ91 magnesium alloy, Intermetallics. 15 (2007) 1511–1517.

[157] W. Zhou, N.N. Aung, Y. Sun, Effect of antimony, bismuth and calcium addition on corrosion and electrochemical behaviour of AZ91 magnesium alloy, Corros. Sci. 51 (2009) 403–408.

[158] S. Candan, M. Unal, M. Turkmen, E. Koc, Y. Turen, E. Candan, Improvement of mechanical and corrosion properties of magnesium alloy by lead addition, Mater. Sci. Eng. A. 501 (2009) 115–118.

[159] A.D. Südholz, N. Birbilis, C.J. Bettles, M.A. Gibson, Corrosion behaviour of Mg-alloy AZ91E with atypical alloying additions, J. Alloys Compd. 471 (2009) 109–115.

[160] R. Arrabal, A. Pardo, M.C. Merino, M. Mohedano, P. Casajús, K. Paucar, et al., Effect of Nd on the corrosion behaviour of AM50 and AZ91D magnesium alloys in 3.5wt.% NaCl solution, Corros. Sci. 55 (2012) 301–312.

[161] R. Arrabal, B. Mingo, A. Pardo, E. Matykina, M. Mohedano, M.C. Merino, et al., Role of alloyed Nd in the microstructure and atmospheric corrosion of as-cast magnesium alloy AZ91, Corros. Sci. 97 (2015) 38–48.

[162] R. Arrabal, E. Matykina, A. Pardo, M.C. Merino, K. Paucar, M. Mohedano, et al., Corrosion behaviour of AZ91D and AM50 magnesium alloys with Nd and Gd additions in humid environments, Corros. Sci. 55 (2012) 351–362.

[163] T.J. Luo, Y.S. Yang, Y.J. Li, X.G. Dong, Influence of rare earth Y on the corrosion behavior of as-cast AZ91 alloy, Electrochim. Acta. 54 (2009) 6433–6437.

[164] F. Mert, C. Blawert, K.U. Kainer, N. Hort, Influence of cerium additions on the corrosion behaviour of high pressure die cast AM50 alloy, Corros. Sci. 65 (2012) 145–151.

[165] R. Walter, M.B. Kannan, Influence of surface roughness on the corrosion behaviour of magnesium alloy, Mater. Des. 32 (2011) 2350–2354.

[166] G. Wu, Y. Fan, A. Atrens, C. Zhai, W. Ding, Electrochemical behavior of magnesium alloys AZ91D, AZCe2, and AZLa1 in chloride and sulfate solutions, J. Appl. Electrochem. 38 (2008) 251–257.

[167] A. Suzuki, N.D. Saddock, J.W. Jones, T.M. Pollock, Phase equilibria in the Mg-Al-Ca ternary system at 773 and 673 K, Metall. Mater. Trans. A. 37 (2006) 975–983.

[168] B. Kondori, R. Mahmudi, Effect of Ca additions on the microstructure, thermal stability and mechanical properties of a cast AM60 magnesium alloy, Mater. Sci. Eng. A. 527 (2010) 2014–2021.

[169] W. Chen, J. Kong, W.J. Chen, Effect of rare earth Ce on the microstructure, physical properties and thermal stability of a new lead-free solder, J. Min. Metall. B Metall. 47 (2011) 11–21.

[170] A. Suzuki, N.D. Saddock, J.W. Jones, T.M. Pollock, Solidification paths and eutectic intermetallic phases in Mg-Al-Ca ternary alloys, Acta Mater. 53 (2005) 2823–2834.

[171] R. Ninomiya, T. Ojiro, K. Kubota, Improved heat resistance of Mg-Al alloys by the Ca addition, Acta Metall. Mater. 43 (1995) 669–674.

[172] A.K. Mondal, S. Kumar, C. Blawert, N.B. Dahotre, Effect of laser surface treatment on corrosion and wear resistance of ACM720 Mg alloy, Surf. Coatings Technol. 202 (2008) 3187–3198.

[173] M.P. Liu, Q.D. Wang, X.Q. Zeng, Y.H. Wei, Y.P. Zhu, C. Lu, Development of microstructure in solution-heat-treated Mg-5Al-xCa alloys, Zeitschrift Für Met. 94 (2003) 886–891.

[174] M. Liu, Q. Wang, Z. Liu, G. Yuan, G. Wu, Y. Zhu, et al., Behavior of Mg–Al–Ca alloy during solution heat treatment at 415 °C, J. Mater. Sci. Lett. 21 (2002) 1281–1283.

[175] H. Okamoto, Ca-Sb (Calcium-Antimony), J. Phase Equilibria. 18 (1997) 313–313.

[176] A.H. Feng, Z.Y. Ma, Enhanced mechanical properties of Mg-Al-Zn cast alloy via friction stir processing, Scr. Mater. 56 (2007) 397–400.

[177] G. Nussbaum, P. Bridot, T.J. Warner, J. Charbonnier, G. Regazzon, New Mg-Al based alloys with improved casting and corrosion properties, in: B.L. Mordike, F. Hehmann (Eds.), Magnes. Alloy. Their Appl., DGM, Germany, 1992: pp. 351–358.

[178] H.A. Patel, D.L. Chen, S.D. Bhole, K. Sadayappan, Microstructure and tensile properties of thixomolded magnesium alloys, J. Alloys Compd. 496 (2010) 140–148.

[179] M. Regev, E. Aghion, A. Rosen, M. Bamberger, Creep studies of coarse-grained AZ91D magnesium castings, Mater. Sci. Eng. A. 252 (1998) 6–16.

[180] A. Boby, K.K. Ravikumar, U.T.S. Pillai, B.C. Pai, Effect of antimony and yttrium addition on the high temperature properties of AZ91 magnesium alloy, Procedia Eng. 55 (2013) 98–102.

[181] L. Liu, H. Ding, Study of the plastic flow behaviors of AZ91 magnesium alloy during thermomechanical processes, J. Alloys Compd. 484 (2009) 949–956.

[182] J. Guo, L. Chen, Y. Xu, F. Lian, Investigation of the compressive creep behavior of AZ91D magnesium alloy, Mater. Sci. Eng. A. 443 (2007) 66–70.

[183] K. Ishikawa, H. Watanabe, T. Mukai, High strain rate deformation behavior of an AZ91 magnesium alloy at elevated temperatures, Mater. Lett. 59 (2005) 1511–1515.

[184] S.N.G. Chu, J.C.M. Li, Impression creep; a new creep test, J. Mater. Sci. 12 (1977) 2200–2208.

[185] H. Somekawa, K. Hirai, H. Watanabe, Y. Takigawa, K. Higashi, Dislocation creep behavior in Mg–Al–Zn alloys, Mater. Sci. Eng. A. 407 (2005) 53–61.

[186] A.C. Fischer-Cripps, Introduction to contact mechanics, Second Edi, Springer, New York, 2000.

[187] H.Y. Ha, J.Y. Kang, J. Yang, C.D. Yim, B.S. You, Limitations in the use of the potentiodynamic polarisation curves to investigate the effect of Zn on the corrosion behaviour of as-extruded Mg-Zn binary alloy, Corros. Sci. 75 (2013) 426–433.

[188] M.C. Zhao, M. Liu, G.L. Song, A. Atrens, Influence of pH and chloride ion concentration on the corrosion of Mg alloy ZE41, Corros. Sci. 50 (2008) 3168–3178.

[189] J.R. Macdonald, Impedance spectroscopy: emphasizing solid materials and analysis, John Wiley & Sons, New York, 1987.

[190] J.-B. Jorcin, M.E. Orazem, N. Pébère, B. Tribollet, CPE analysis by local electrochemical impedance spectroscopy, Electrochim. Acta. 51 (2006) 1473–1479.

[191] D.D. MacDonald, Reflections on the history of electrochemical impedance spectroscopy, Electrochim. Acta. 51 (2006) 1376–1388.

[192] A.D. King, N. Birbilis, J.R. Scully, Accurate electrochemical measurement of magnesium corrosion rates; A combined impedance, mass-loss and hydrogen collection study, Electrochim. Acta. 121 (2014) 394–406.

[193] G.W. Walter, A review of impedance plot methods used for corrosion performance analysis of painted metals, Corros. Sci. 26 (1986) 681–703.

[194] G. Song, A. Atrens, D.S. John, X. Wu, J. Nairn, The anodic dissolution of magnesium in chloride and sulphate solutions, Corros. Sci. 39 (1997) 1981–2004.

[195] G. Baril, N. Pébère, Corrosion of pure magnesium in aerated and deaerated sodium sulphate solutions, Corros. Sci. 43 (2001) 471–484.

[196] Z. Qiao, Z. Shi, N. Hort, N.I. Zainal Abidin, A. Atrens, Corrosion behaviour of a nominally high purity Mg ingot produced by permanent mould direct chill casting, Corros. Sci. 61 (2012) 185–207.

[197] Y.Q. Wang, M.Z. Li, C. Li, X.Y. Li, L.Q. Fan, T. Jia, The effect of Ca on corrosion behavior of heat-treated Mg-Al-Zn alloy, Mater. Corros. 63 (2012) 497–504.

[198] M. Jönsson, D. Persson, D. Thierry, Corrosion product formation during NaCl induced atmospheric corrosion of magnesium alloy AZ91D, Corros. Sci. 49 (2007) 1540–1558.

[199] W. Liu, F. Cao, B. Jia, L. Zheng, J. Zhang, C. Cao, et al., Corrosion behaviour of AM60 magnesium alloys containing Ce or La under thin electrolyte layers. Part 2: Corrosion product and characterization, Corros. Sci. 52 (2010) 639–650.

[200] A. Pardo, M.C. Merino, A.E. Coy, F. Viejo, R. Arrabal, S. Feliú, Influence of microstructure and composition on the corrosion behaviour of Mg/Al alloys in chloride media, Electrochim. Acta. 53 (2008) 7890–7902.

[201] Y. Lü, Q. Wang, X. Zeng, W. Ding, C. Zhai, Y. Zhu, Effects of rare earths on the microstructure, properties and fracture behavior of Mg–Al alloys, Mater. Sci. Eng. A. 278 (2000) 66–76.

[202] Y. Wang, Q. Wang, C. Ma, W. Ding, Y. Zhu, Effects of Zn and RE additions on the solidification behavior of Mg-9Al magnesium alloy, Mater. Sci. Eng. A. 342 (2003) 178–182.

[203] C.J. Bettles, The effect of gold additions on the ageing behaviour and creep properties of the magnesium alloy AZ91E, Mater. Sci. Eng. A. 348 (2003) 280–288.

[204] B.I.N. Tang, S.-S. Li, X. Wang, D.Z.R. Wu, An investigation on hot-crack mechanism of Ca addition into AZ91D alloy, J. Mater. Sci. 40 (2005) 2931–2936.

[205] K. Hirai, H. Somekawa, Y. Takigawa, K. Higashi, Effects of Ca and Sr addition on mechanical properties of a cast AZ91 magnesium alloy at room and elevated temperature, Mater. Sci. Eng. A. 403 (2005) 276–280.

[206] B.H. Choi, B.S. You, D.Y. Chang, W.W. Park, I.M. Park, Microstructure and mechanical properties of Ca containing AZ91 magnesium alloys, Mater. Sci. Forum. 475–479 (2005) 2477–2480.

[207] Y. Fan, G.H. Wu, H.T. Gao, C.Q. Zhai, The effect of RE and Ca on corrosion resistance of AZ91, Mater. Sci. Forum. 488–489 (2005) 869–872.

[208] L. Haifeng, T. Guodong, H. Jun, Development of high temperature creep resistant magnesium alloys for die casting, Mater. Sci. Forum. 488–489 (2005) 279–282.

[209] S.S. Li, B. Tang, D.B. Zeng, Effects and mechanism of Ca on refinement of AZ91D alloy, J. Alloys Compd. 437 (2007) 317–321.

[210] Y. Fan, G.H. Wu, C.Q. Zhai, Effect of strontium on mechanical properties and corrosion resistance of AZ91D, Mater. Sci. Forum. 546–549 (2007) 567–570.

[211] S.J. Yao, D.Q. Yi, S. Yang, X.H. Cang, W.X. Li, Effect of Sc on microstructures and corrosion properties of AZ91, Mater. Sci. Forum. 546–549 (2007) 139–142.

[212] I. Takeuchi, K. Hirai, Y. Takigawa, T. Uesugi, K. Higashi, Effect of Ca and Sr content on elevated temperatures mechanical properties of a cast AZ91 magnesium alloy, Adv. Mater. Res. 26–28 (2007) 141–144.

[213] S.F.F. Liu, B. Li, X.H.H. Wang, W. Su, H. Han, Refinement effect of cerium, calcium and strontium in AZ91 magnesium alloy, J. Mater. Process. Technol. 209 (2009) 3999–4004.

[214] M. Sumida, Microstructure development of sand-cast AZ-type magnesium alloys modified by simultaneous addition of calcium and neodymium, J. Alloys Compd. 460 (2008) 619–626.

[215] S.L. Cheng, G.C. Yang, J.F. Fan, Y.J. Li, Y.H. Zhou, Effect of Ca and Y additions on oxidation behavior of AZ91 alloy at elevated temperatures, Trans. Nonferrous Met. Soc. China. 19 (2009) 299–304.

[216] J.X. Niu, Q.R. Chen, N.X. Xu, Z.L. Wei, Effect of combinative addition of strontium and rare earth elements on corrosion resistance of AZ91D magnesium alloy, Trans. Nonferrous Met. Soc. China. 18 (2008) 1058–1064.

[217] S.F. Liu, L.Y. Liu, L.G. Kang, Refinement role of electromagnetic stirring and strontium in AZ91 magnesium alloy, J. Alloys Compd. 450 (2008) 546–550.

[218] A. Khosravani, H. Aashuri, P. Davami, A. Narimannezhad, A. Foroughi, M. Kiani, Microstructural evolution of AZ91 alloy containing 3%Ca prepared by cooling slope, Solid State Phenom. 141–143 (2008) 427–432.

[219] H. Bayani, E. Saebnoori, Effect of rare earth elements addition on thermal fatigue behaviors of AZ91 magnesium alloy, J. Rare Earths. 27 (2009) 255–258.

[220] Z. Zhao, Q. Chen, Y. Wang, D. Shu, Microstructures and mechanical properties of AZ91D alloys with Y addition, Mater. Sci. Eng. A. 515 (2009) 152–161.

[221] K. Meshinchi Asl, A. Tari, F. Khomamizadeh, The effect of different content of Al, RE and Si element on the microstructure, mechanical and creep properties of Mg-Al alloys, Mater. Sci. Eng. A. 523 (2009) 1–6.

[222] D.H. Xiao, M. Song, F.Q. Zhang, Y.H. He, Characterization and preparation of Mg–Al–Zn alloys with minor Sc, J. Alloys Compd. 484 (2009) 416–421.

[223] X.P. Cui, H.F. Liu, J. Meng, D.P. Zhang, Microstructure and mechanical properties of die-cast AZ91D magnesium alloy by Pr additions, Trans. Nonferrous Met. Soc. China. 20 (2010) s435–s438.

[224] F. Guo, P. Li, X. Gao, J. Xu, Study on solid solution and aging process of AZ91D magnesium alloy with cerium, J. Rare Earths. 28 (2010) 948–951.

[225] Y. Yang, X. Li, Influence of neodymium on high cycle fatigue behavior of die cast AZ91D magnesium alloy, J. Rare Earths. 28 (2010) 456–460.

[226] G.D. Tong, H.F. Liu, Y.H. Liu, Effect of rare earth additions on microstructure and mechanical properties of AZ91 magnesium alloys, Trans. Nonferrous Met. Soc. China (English Ed. 20 (2010) s336–s340.

[227] Q. Wang, Y. Liu, S. Fang, Y. Song, D. Zhang, L. Zhang, et al., Evaluating the improvement of corrosion residual strength by adding 1.0 wt.% yttrium into an AZ91D magnesium alloy, Mater. Charact. 61 (2010) 674–682.

[228] C.S. Goh, K.S. Soh, P.H. Oon, B.W. Chua, Effect of squeeze casting parameters on the mechanical properties of AZ91 – Ca Mg alloys, Mater. Des. 31 (2010) S50–S53.

[229] J.X. Zhou, J. Wang, J. Wang, Y.S. Yang, Effects of RE and Sr additions on dendrite growth and phase precipitation in AZ91D magnesium alloy, Trans. Nonferrous Met. Soc. China. 20 (2010) s331–s335.

[230] B. Nami, H. Razavi, S.M. Miresmaeili, S. Mirdamadi, S.G. Shabestari, Impression creep properties of a semi-solid processed magnesium-aluminum alloy containing

calcium and rare earth elements, Scr. Mater. 65 (2011) 221–224.

[231] B. Nami, S.G. Shabestari, H. Razavi, S. Mirdamadi, S.M. Miresmaeili, Effect of Ca, RE elements and semi-solid processing on the microstructure and creep properties of AZ91 alloy, Mater. Sci. Eng. A. 528 (2011) 1261–1267.

[232] L. Wang, Y.M. Kim, J. Lee, B.S. You, Improvement in rollability of AZ91 magnesium alloy by carbon addition, Mater. Sci. Eng. A. 528 (2011) 943–949.

[233] Z.J. Wang, Y. Xu, J. Zhu, Effects of erbium addition on the corrosion resistance and microstructure of AZ91 magnesium alloy, Adv. Mater. Res. 194–196 (2011) 1221–1224.

[234] X. Ai, G. Quan, J. Yang, Effect of Ti on the mechanical properties and corrosion of cast AZ91 magnesium alloy, Adv. Mater. Res. 311–313 (2011) 1457–1461.

[235] S. Candan, M. Unal, E. Koc, Y. Turen, E. Candan, Effects of titanium addition on mechanical and corrosion behaviours of AZ91 magnesium alloy, J. Alloys Compd. 509 (2011) 1958–1963.

[236] L. Hu, Q. Meng, S. Chen, H. Wang, Effect of Zn content on the chemical conversion treatments of AZ91D magnesium alloy, Appl. Surf. Sci. 259 (2012) 816–823.

[237] Q. Fu, Y. Li, G. Liu, H. Li, Low cycle fatigue behavior of AZ91D magnesium alloy containing rare-earth Ce element, Procedia Eng. 27 (2012) 1794–1800.

[238] D.Q. Wan, Enhanced corrosion resistance and damping capacity of as-cast AZ91 magnesium alloys with Ce addition, Adv. Mater. Res. 418–420 (2011) 246–249.

[239] Q. Sun, H. Wang, Y. Zhu, Effect of alloying elements on the microstructure and properties of AZ91D-xCa-ySr, Adv. Mater. Res. 591–593 (2012) 993–996.

[240] A. Srinivasan, K.K. Ajithkumar, J. Swaminathan, U.T.S. Pillai, B.C. Pai, Creep behavior of AZ91 magnesium alloy, Procedia Eng. 55 (2013) 109–113.

[241] J. Zhang, Z. Wang, W. Sun, M. Zhu, Microstructure and corrosion behavior of AZ91-0.4%Nd magnesium alloy, Appl. Mech. Mater. 291–294 (2013) 2577–2580.

[242] J.M. Zhang, Z.H. Wang, H. Cai, M. Zhu, L. Bin Niu, Corrosion behavior of AZ91/AZ91-0.4%Nd alloys in 3.5wt.% NaCl, Appl. Mech. Mater. 291–294 (2013) 699–702.

[243] Y. Huang, H. Dieringa, K.U. Kainer, N. Hort, Understanding effects of microstructural inhomogeneity on creep response – New approaches to improve the creep resistance in magnesium alloys, J. Magnes. Alloy. 2 (2014) 124–132.

[244] J. Yang, Y. Li, P. Xue, Corrosion resistance of RE-AZ91 magnesium alloys, Adv. Mater. Res. 933 (2014) 66–70.

[245] E. Levent, Z. Huseyin, T. Yunus, T.M. Emre, S. Yavuz, A. Hayrettin, Effects of bismuth (Bi) additions on microstructure and mechanical properties of AZ91 alloy, in: Met. 2015, Brno, Czech Republic, EU, 2015.

[246] Y. Zhang, G. Wu, W. Liu, L. Zhang, S. Pang, W. Ding, Microstructure and mechanical properties of rheo-squeeze casting AZ91-Ca magnesium alloy prepared by gas bubbling process, Mater. Des. 67 (2015) 1–8.

[247] F. Chong, L. Mingzhao, H. Yang, W. Haiyan, L. Xiaoyan, F. Liuqun, Effect of Ca on corrosion resistance behavior of as-cast AZ91 magnesium alloys, Rare Met. Mater. Eng. 44 (2015) 41–47.

Dissemination

Publications from the present thesis in peer reviewed international journals

1. **A.K.S. Bankoti**, A.K. Mondal, S. Kumar, B.C. Ray, Individual and combined additions of calcium and antimony on microstructure and mechanical properties of squeeze-cast AZ91D magnesium alloy, Mater. Sci. Eng. A. 626 (2015) 186–194.
2. **A.K.S. Bankoti**, A.K. Mondal, Hajo Dieringa, B.C. Ray, S. Kumar, Impression creep behaviour of squeeze-cast Ca and Sb added AZ91 magnesium alloy, Mater. Sci. Eng. A. 673 (2016) 332-345.
3. **A.K.S. Bankoti**, A.K. Mondal, Chandra S. Perugu, B.C. Ray, S. Kumar, Correlation of microstructure and electrochemical corrosion behaviour of squeeze-cast Ca and/or Sb added AZ91 Mg alloys, Metall. Mater. Trans. A, Revision submitted.
4. **A.K.S. Bankoti**, Chandra S. Perugu, B.C. Ray, A.K. Mondal, Compressive creep behaviour of squeeze-cast Ca and Sb added AZ91 Mg alloy, Manuscript under preparation.

Conferences attended

1. **A.K.S. Bankoti**, A.K. Mondal, S. Kumar, B.C. Ray, Damping behaviour of Ca and Sb added squeeze-cast AZ91D Mg alloys, 4-6 February 2016, iMagCon 2016, VIT Chennai, India.
2. **A.K.S. Bankoti**, A.K. Mondal, S. Kumar, B.C. Ray, Microstructure and properties of Ca and Sb added squeeze cast AZ91 Mg alloys, 11-13 December 2014, ISRS 2014, IIT Madras, India.